Magnetoelectric Particle Imaging of Neural Electrical Fields using Optimized Nanofabricated Structures

by

Ilhan Bok

A Dissertation Submitted in Partial Fulfillment of

the Requirements for the Degree of

Doctor of Philosophy

(Electrical and Computer Engineering)

at the

University of Wisconsin–Madison

2024

Date of Final Oral Examination: 6/5/2024
This Dissertation is Approved by the Members of the Final Oral Examination Committee:
Aviad Hai, Ph.D., Assistant Professor, Biomedical Engineering
Irena Knezevic, Ph.D., Professor, Electrical and Computer Engineering
Raunak Sinha, Ph.D., Assistant Professor, Neuroscience
Ronald T. Wakai, Ph.D., Professor, Medical Physics

Dedication

To my family for supporting my educational endeavors,

to my fellow researchers for showing me a part of life I had never seen,

and to my advisor Dr. Aviad Hai for showing me a part of myself I had never envisioned.

In Memoriam

Frankie Ziyu Wang

2001-2023

Acknowledgments

This extraordinary Ph.D. was realized through extraordinary mentoring. Dr. Aviad Hai served as a mentor who was fully committed to all facets of my academic and personal growth. Upon entering the lab, I found myself immersed in an environment where I was able to reach beyond my full potential. Every seminar, discussion, presentation, simulation, experiment, and project I undertook provided incredible insights into the most amazing aspects of neuroengineering. I also acknowledge my committee members Dr. Irena Knezevic, Dr. Raunak Sinha, and Dr. Ronald T. Wakai who provided me with the support and advice necessary for this laborious process.

Although this thesis represents years of dedication, the support and encouragement from colleagues lent to its passage in a blur. I commend Dr. Jax Phillips for not only setting an incredible academic precedent but also for their nonjudgmental, unwavering support for everyone in the lab. I thank Suyash Bhatt for organizing numerous lab outings by which I was able to connect with fellow lab members, including Adam Vareberg, Emily Blick, TShawn (Tianxiang) Zhu, Alireza Ashtiani, Yash Gokhale, Anna Vena, Emily Masterson, Maya Lines, Thor Larson, Jamie Sergay, and Judy George. In the lab, I was fortunate enough to collaborate with fellow students Virgil (Xiangfei) Wang, Ido Haber, Tyler Kearse, Maya Nornberg, Jennifer (Xiaofei) Qu, Xiaoxuan Ren, Frankie Ziyu Wang, and many more researchers throughout the University of Wisconsin - Madison.

Finally, I owe this degree to my family and apologize for my obsession with science which wreaked havoc on our household.

Abstract

While mainstream clinical techniques for functional imaging of the brain such as BOLD (blood oxygenation level dependent) fMRI (functional magnetic resonance imaging), molecular fMRI, PET (positron emission tomography), CT (computed tomography), fNIRS (functional near-infrared spectroscopy), EEG (electroencephalography), MEG (magnetoencephalography), and electrophysiology offer impressive advantages and comprehensive breadth, they nevertheless possess a wide range of well-known pitfalls precluding acquisition of richer readouts that would expedite numerous aspects of neuroscientific research and inquiry. In particular, there has yet to be a technology which benefits researchers and clinicians alike with a functional full-brain readout with exceptional spatial and temporal resolution. To address this need, this dissertation examines the capabilities of geometrically varied magnetoelectric nanoscale structures for their usage as readout vehicles for full-brain neuroelectrophysiology using magnetic particle imaging (MPI) with high spatiotemporal resolution and sensitivity (termed magnetoelectric particle imaging (MEPI)). With this goal in mind, I performed finite element modeling of nanoscale structures, developed novel multi-step nanofabrication techniques to produce structures, applied magnetic force microscopy to characterize the structures, and assessed biocompatibility *in vitro* before performing single-point magnetic particle imaging recordings and correlating frequency-domain features to conventional extracellular electrophysiology using microelectrode arrays. These structures, including superparamagnetic iron oxide nanoparticles (SPIONs) developed for magnetic resonance imaging, provide a pathway for injectable and large-scale implantable sensors to image neural electric fields with high spatiotemporal resolution and sensitivity.

Table of Contents

Table of Figures

Table of Tables

Introduction

A large variety of imaging techniques with various advantages and disadvantages currently exist for imaging the brain. Walking through these techniques individually, fMRI (functional magnetic resonance imaging) has achieved widespread prominence due to its supposed ability to determine the response of various regions of the brain, there has been equally pervasive criticism of its capacity to properly identify regions of neural engagement. PET (positron emission tomography) uses radiolabeled ligands to detect biochemical events within the brain, such as glucose metabolism. However, it uses specialized, unstable, radioactive tracers and has relatively low spatiotemporal resolution. EEG (electroencephalography) is a surface measurement system for electric fields and has high temporal and low spatial resolution. However, electric fields are harshly attenuated by the skull and skin and this technique additionally suffers from the inverse problem. MEG (magnetoencephalography) is similar to EEG except rather than electric fields it uses magnetic fields which experience less severe distortion from cranial features. Unfortunately, it also suffers from the inverse problem. fNIRS (functional near-infrared spectroscopy) has spatial resolution far worse than the previous tools but offers the ability to measure hemodynamic response without the need for immobility. fMRI (functional magnetic resonance imaging) works on similar principles but requires immobility for cleaner images and like fNIRS suffers from statistical concerns rendering interpretation of results more complicated. Electrophysiology has excellent spatiotemporal resolution but is localized and highly invasive due to bulky electrodes interfacing with surgically exposed brain tissue. Computed tomography (CT) is mostly a structural or anatomical modality with a small number of studies showing functional readouts[1, 2], but exposes the subject to ionizing radiation. Single-photon emission computerized tomography (SPECT) operates on a similar principle to PET and is likewise challenging for use due to tracer

instability and low spatiotemporal resolution. Ultrasound suffers from signal attenuation from air cavities and bone, and is prone to artifacts. However, these disadvantages are absent or mitigated within a novel, emerging volumetric imaging paradigm deemed magnetic particle imaging (MPI) which in a primordial manner can detect iron oxide nanoparticles in the brain [3]. The high spatiotemporal resolution and sensitivity of MPI renders it as an optimal choice for functional imaging of the brain.

Among all the modalities mentioned above, electrophysiology remains the most direct form of accessing the brain with superior abilities to record spiking activity and create high-fidelity brain-machine interfaces which have endowed a wide set of benefits to subjects with varying degrees of paralysis. However, despite their success and feature improvements throughout time, the sheer number of electrodes required for a comprehensive neural interface is on the order of 100 billion electrodes. Ever since the introduction of the Utah array in 2006 where a tetraplegic patient operated various prostheses by controlling his neural activity[4], designs today require large hardware modules and bear bulky electrodes and extracranial wiring [5]that would theoretically require hundreds of millions of intrusive shanks to record from the entirety of the brain [6].

New sensors and modulators that interact wirelessly with medical modalities unlock uncharted avenues for *in situ* brain recording and stimulation. Ongoing miniaturization, material refinement, and sensitization to specific neurophysiological and neurochemical processes are spurring new capabilities that begin to transcend the constraints of traditional bulky and invasive wired probes. Current state-of-the-art agents span diverse realms of operation and represent various possibilities depending on size, delivery, specificity and spatiotemporal resolution. These devices span implantable and injectable micro- and nano-scale electronic devices operating at or below the radio frequency (RF) regime with simple near field transmission, and continue with more sophisticated

devices, nanoparticles and biochemical molecular conjugates acting as dynamic contrast agents in magnetic resonance imaging (MRI), ultrasound (US) transduction and other functional tomographic modalities. Some of these technologies can deliver stimulation and neuromodulation with emerging probes and materials that provide minimally invasive magnetic, electrical, thermal and optogenetic stimulation. These methodologies are transforming the repertoire of readily available technologies paired with compatible imaging systems and hold promise toward broadening the expanse of neurological and neuroscientific diagnostics and therapeutics. (Fig. 1) that are attempting to change the invasiveness of neural readout methodologies while improving spatiotemporal resolution. Scanning through this parameter space shows there are standalone structures including micro- and nano-fabricated sensors with exotic shapes and methods of operation are allowing traditional modalities (MRI, ultrasound, and optogenetics) to be repurposed for new detection methodologies. Molecular probes and nanoparticle sensors that operate within the biochemical realm are providing new inroads into detecting events within the brain. These sensors all exhibit varying levels of invasiveness which may cause glial activation depending on the level of aggravation caused during implantation. Devices that can be introduced with no craniotomy and without adverse effects would be ideal for tools such as MRI and Ultrasound. All these probes can give specific readouts specific to neural processes, not just magnetic particle imaging. However, MPI is better than MRI for these purposes because it is not limited by the physical or theoretical boundaries of spin relaxation [7].

MPI is a highly promising, emerging imaging modality capable of recording real-time, local concentrations of magnetic tracer in many different organ systems. Iron oxide nanoparticles can be detected in vivo using real-time perfusion magnetic particle imaging and have been used to monitor ischemic stroke [3] (Videos V1-2). Iron oxide (formulated commercially as Resovist) is

the traditional tracer used within MPI [7]. The rationale for using MPI is that this emerging, rapidly evolving preclinical modality allows for an imaging scheme that is faster, less expensive, higher resolution, and safer which is fully compatible with smaller, simpler, and more robust sensors. MPI has already been used for non-electrophysiological readouts of the brain vasculature [3], and using dynamic magnetoelectric barium titanate – cobalt ferrite rather than passive iron oxide nanoparticles has the capability to further advance wireless electrophysiology of the brain in clinical settings. MPI operates by using a series of coils to deliver AC stimulation to superparamagnetic iron oxide nanoparticles with a "field free point" scanned through a region of interest to produce concentration-dependent readouts that can be directly mapped onto an output image. MPI relies on the principle that a sinusoidal magnetic stimulation waveform will be modulated by the Langevin function of the superparamagnetic tracer to induce a magnetization change which contains odd harmonics whose magnitude is proportional to the concentration of sample present in the field free point (Fig. 2).

Emerging magnetoelectric materials can be efficiently modulated by remote electric or magnetic alternating fields in the presence of a bias magnetic field, with rapid responsiveness at picosecond timescales, heralding new capabilities in diverse fields including bioelectronic medicine [8–10]. Injectable bio-compatible magnetoelectric nanoparticles (MENPs) comprising a magnetostrictive $CoFe_2O_4$ (CFO) core coated with a piezoelectric $BaTiO_3$ (BTO) shell were specifically simulated [11] and shown in recent years [10, 12] to facilitate wireless neural stimulation offering a possible alternative to current bulky clinical stimulators. MENPs were injected into the subthalamic region in mice for magnetic-field-controlled deep brain stimulation using relatively small fields (220 mT bias, 140 Hz 6 mT alternating) successfully eliciting local brain activity changes manifested behaviorally as alterations in gait and movement patterns [12]. This work strongly suggests

potential use for minimally invasive therapeutic amelioration of Parkinsonian symptoms. Additional demonstrations of synchronous neuronal firing activity driven by MENP stimulation at 20 Hz [10] present utilities for modulating neural activity at single neuron resolution. Parallel voltage sensitive dye measurements for detecting electric fields developing proximally to MENPs, and also open avenues for opto-magnetoelectric imaging of neural electrical activity or magnetoelectrically mediated optogenetic stimulation of the brain. MENPs were also recently proposed for brain recording as a specialized variant of magnetic particle imaging (MPI) also termed magnetoelectric particle imaging (MEPI) [13]. Quantifications of the MEPI neural readouts of injected CFO-BTO diffusing in brain tissue demonstrate the feasibility of structural and dynamic functional imaging of neural activity. Further analysis demonstrates optimized core-shell ratios informing future MENP synthesis that can enable direct volumetric imaging of electrophysiology with superior spatiotemporal resolution limited only by scanner performance [14]. The ability of CFO-BTO MENPs to traverse the BBB and maintain relatively long term biocompatibility was affirmed using MRI-directed delivery in non-human primates at clinical fields [15]. Entry into cerebral areas and deeper basal ganglia was confirmed as T2* signal decreases 3 hours following intravenous injection. Moreover, blood profile toxicity verifications and work demonstrating minimal glial inflammatory activation following BBB penetration [16] point to the evolution of MENPs as a viable and broad clinical tool in the near future.

Magnetoelectric materials have also been used to augment wireless micro- and nano-electronic neural probes allowing for the measurement of very small magnetic fields in the brain. A hypersensitive thin bilayer consisting of ferromagnetic iron gallium boron (FeGaB) and piezoelectric aluminum nitride (AlN) were designed as a magnetoelectric microscale antenna sensor array loaded with complex onboard transmission and reception circuitry and theoretically

able to record physiological fields with high sensitivity of up to 40 pT and 200 μm × 10s to 100s of MHz spatiotemporal resolution [17]. Further work affirm that the proposed highly miniaturized magnetoelectric antenna (250 × 174 μm^2) has wireless power transfer efficiency between one and two orders of magnitude above existing miniaturized micro-coils and a lower limit of detection between 300 and 500 pT in neural tissue [18]. These approaches can supersede standard antennas for neural implants replacing sensitive wired probes. This highly elevated power transfer was also shown to enable stimulation using magnetostrictive Metglas layer bonded to piezoelectric as a magnetically powered small (<25 mm^2) neural stimulators at 100-200 Hz [9]. Stimulation of the subthalamic nucleus using such encapsulated wireless magnetoelectric bilayer implants modulated oxidopamine-induced Parkinsonian symptoms in freely moving rats. Furthermore, similar magnetoelectric-powered bio implants (ME-BITs) can be delivered non-surgically through a percutaneous catheter and enable frequency-dependent amplitude modulation-based endovascular stimulation at 1-10 Hz using strain-coupled metglas – lead zirconium titanate bilayer in rat sciatic nerve or pig femoral artery [19]. The same proof-of-concept has been applied previously for peripheral neurostimulation up to 200 Hz mitigating neuropathic pain verified using GCaMP6s *in vivo* [20]. Together, these approaches greatly simplify delivery, power relay and implementation of wireless circuitry.

In this introduction, I surveyed clinical imaging techniques, cutting-edge augmentations to wireless neural probe technologies, the theoretical basis for MPI, and applications of magnetoelectric materials. In particular, I touched upon the need for a novel wireless electrophysiology platform that is unburdened by the disadvantages of traditional clinical imaging technologies and provides the basis for a simple and adaptable method for functional imaging of neural activity. As a proof-of-principle, I describe within this thesis a line of experiments

beginning with detailed finite element simulations of magnetoelectric nanoparticles and their predicted MPI magnetization readout from neuronal morphologies and cortical neural networks *in silico* (Chapter 1). This modeling forms the basis for the simulation and fabrication of magnetoelectric rings with subsequent characterization using magnetic force microscopy of their sensitivity to electric fields (Chapter 2). Lastly, I assess biocompatibility of magnetoelectric structures and utilize arrays of fabricated rings to sense and record electric fields from neural networks and compare these traces to those acquired via microelectrode array electrophysiology (Chapter 3). These results form the basis for MEPI as a wireless imaging tool with high spatiotemporal resolution and sensitivity which transcends the limitations of classic functional brain recording techniques and instrumentation, opening the gates to a wider range of applications and configurations in clinical milleu.

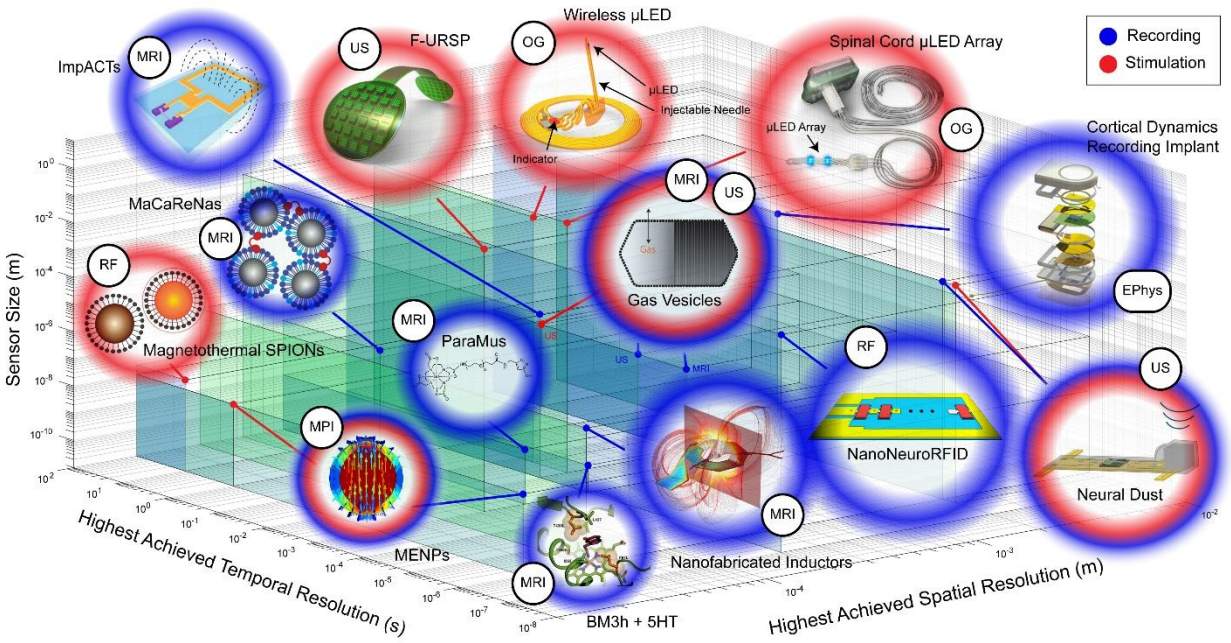

Figure 1: Overview of the approximate sizes and spatiotemporal resolutions of neural transducers.

Blue halos indicate probes used for recording, red halos indicate stimulation and bicolor halos indicate dual recording/stimulation capability, smaller black circles indicate corresponding imaging techniques (MRI = magnetic resonance imaging, MPI = magnetic particle imaging, US = ultrasound, EPhys = electrophysiology, RF = radiofrequency, OG = optogenetics). Tinted blue-green planes are included to facilitate context determination of spatial resolution (x-axis), temporal resolution (y-axis), and sensor size (z-axis).

Chapter 1: *In Silico* Assessment of Electrophysiological Neuronal Recordings Mediated by Magnetoelectric Nanoparticles

Ilhan Bok, Ido Haber, Xiaofei Qu, Aviad Hai

Sci Rep. 2022 May 19;12(1):8386. doi: 10.1038/s41598-022-12303-4.

Abstract

Magnetoelectric materials hold untapped potential to revolutionize biomedical technologies. Sensing of biophysical processes in the brain is a particularly attractive application, with the prospect of using magnetoelectric nanoparticles (MENPs) as injectable agents for rapid brain-wide modulation and recording. Recent studies have demonstrated wireless brain stimulation *in vivo* using MENPs synthesized from cobalt ferrite (CFO) cores coated with piezoelectric barium titanate (BTO) shells. CFO-BTO core-shell MENPs have a relatively high magnetoelectric coefficient and have been proposed for direct magnetic particle imaging (MPI) of brain electrophysiology. However, the feasibility of acquiring such readouts has not been demonstrated or methodically quantified. Here we present the results of implementing a strain-based finite element magnetoelectric model of CFO-BTO core-shell MENPs and apply the model to quantify magnetization in response to neural electric fields. We use the model to determine optimal MENPs-mediated electrophysiological readouts both at the single neuron level and for MENPs diffusing in bulk neural tissue for *in vivo* scenarios. Our results lay the groundwork for MENP

recording of electrophysiological signals and provide a broad analytical infrastructure to validate MENPs for biomedical applications.

Introduction

Current whole-brain imaging technologies are either solely structural or provide some functional readouts that are limited in scope and indirect to electrophysiological signaling[21–24]. Relatively recent attempts at fully functional readouts mediated by injectable indicators include responsive molecular agents for magnetic resonance imaging (MRI)[25–29] and functional ultrasound[30, 31], injectable microelectronic motes interacting wirelessly with noninvasive neuroimaging modalities[32–34], and systemically expressed optogenetic constructs for whole-brain neural imaging in translucent animal preparations[35, 36]. Magnetic particle imaging (MPI) is an emerging whole-body imaging modality exploiting the nonlinear magnetization of injected magnetic nanoparticles to achieve dynamic non-attenuated depth recordings with improved spatiotemporal resolution[7, 37]. Recent studies demonstrate the use of MPI for brain applications including monitoring of neural injury[38], tracking of brain graft cell migration[39], assessing neuropathology requiring surgical interventions[40], and several other functional characterizations of cerebral blood volume during brain activation[41–44]. The majority of MPI studies rely on the injection of superparamagnetic iron oxide nanoparticles (SPIONs) to acquire concentration-dependent readouts of diffused particles. New magnetic particle designs that offer signal modulation specific to biochemical and physiological processes can create a new repertoire of readouts for MPI.

Developments in the synthesis of magnetoelectric nanoparticles (MENPs) and related structures[45–47] have given rise to diverse material traits that could empower MPI with dynamic readouts relevant to physiology and neurophysiology. Recent research on the magnetoelectric

effect has predominantly focused on the characterization of new material substrates[48–50] and the simulation of lattice interfacial coupling[51, 52]. Finite element modeling (FEM) solvers in particular are used to better characterize a diverse range of magnetoelectric geometric arrangements and structures[53–55]. MENPs and similar heterostructures can be externally modulated by electric and magnetic fields, and have been successfully applied for applications including neurostimulation[16, 56], neural recording[17, 57], tumor ablation[58, 59], drug delivery[58–60], and magnetically controlled nanorobots[61]. These studies and further demonstrations of biological compatibility[8] establish MENPs as injectable agents for *in vivo* preparations allowing for both acute and chronic studies. Further development on magnetoelectric transistors[62], biocompatible implantable devices[63], and integrated brain-computer interfaces[17, 64] could serve as powerful new platforms for studying and managing a wide set of pathologies.

One of the most common composites used in these efforts is a cobalt ferrite (CFO) and barium titanate (BTO) core-shell conjugate (CFO-BTO) due to its high magnetoelectric coupling coefficient and relatively low toxicity, but other emerging composites such as BTO/iron oxide[65, 66] (α = 28.78 mV/cm·Oe), cobalt-doped $BiFeO_3$[67, 68] (α = 6.5 V/cm·Oe), CFO/BTO/polydopamine-P(VDF-TrFE)[69] (α_{E33} = 150.58 mV/cm·Oe), and BTO/nickel[70] (α = 225 μV/cm·Oe) are paving the way to an expanded toolkit of magnetoelectric probes and sensors. With appropriate biocompatible surface functionalization, new magnetoelectric compounds are expanding usability and improving safety for both SPIONs and MENPs for MPI[71–73]. Histological analysis of injected CFO-BTO MENPs in mice demonstrates long-term degradation and excretion[8], and additionally, administration across the blood-brain barrier has been shown by way of intranasal injection in mice[74]. These findings lead to proposing MENPs for use in

conjunction with MPI towards enabling direct volumetric readouts of neurophysiological events[75], presenting estimations of MPI signal change in response to macro-scale electric fields in the brain. However, a computational framework that quantifies particle-level magnetostrictive modulation of CFO-BTO MENPs by neuronal electric fields and combines it with realistic cell morphologies, spiking activity, and particle diffusion has not been developed yet. This has precluded proper determination of the conditions whereby MENPs can be used to acquire direct electrophysiological recordings for experimental implementation.

This study lays the theoretical groundwork for using MENPs to detect neuronal electric fields based on the nonlinear magnetization effect exploited in MPI. We first establish a finite element nanoscale model for CFO-BTO MENPs and quantify their modulation by oscillating external fields. We then simulate magnetization modulation by nearby physiologically-relevant electric fields, and optimize the core-shell ratio for maximal responsiveness and to inform synthesis for sensitive MENPs. Finally, we apply the model to different neuronal morphologies and quantify magnetic field strength across cellular compartments during action potentials at a given MENP concentration and diffusion rate in the brain. This work presents a realistic quantification of the expected MPI signal change using MENPs as the agents injected into neural tissue. More broadly, our model offers a framework that can be applied to assess MENPs for versatile sensing applications.

Results

Nonlinear Magnetization Properties of SPIONs and MENPs

We began by validating our model for SPIONs (Fig. 2a, c, and d, blue) compared with known nonlinear magnetization properties used in MPI[7, 37]. Nanoparticles of diameter d = 30 nm

experienced a magnetic field of H = 40 kA/m resulting in a dipole with a maximal absolute magnetic flux density of 62.3 mT across the applied field (Fig. 2a). For an alternating H-field, SPIONs displayed nonlinear magnetization saturation at ± 347.1 kA/m (Fig. 2c-d, green: alternating H-field, blue: SPION magnetization) consistent with reported values[76, 77]. We next evaluated the response of CFO-BTO MENPs under the same conditions (Fig. 2b, c, and d, red). The maximal absolute magnetic flux density for MENPs was 58.4 mT (Fig. 2b) and nonlinear magnetization saturation in response to alternative fields was observed at ± 89.9 kA/m (Fig. 2c-d, red: MENPs magnetization). We quantified signal harmonics used for signal detection with H-field alternating between ±80.0 kA/m at a frequency of 25.25 kHz applied to both SPIONs or MENPs (Fig 1c, bottom right, red and blue, respectively), with values normalized to the first harmonic. MENPs displayed odd harmonics amplitude ratios comparable to SPIONs, with 100%, 15.80%, 3.54%, and 1.36% for first, third, fifth, and seventh harmonics, respectively, for MENPs. This is compared with 100%, 32.48%, 18.98%, and 13.20% for first, third, fifth, and seventh harmonics, respectively, for SPIONs. The addition of a bias field to the oscillating H-field resulted in negligible harmonics for both MENPs and SPIONs that were magnetically saturated. The presence of MENPs can thus be detected at normal MPI settings using odd harmonics of nonlinear magnetization despite differences in magnetic flux density distribution.

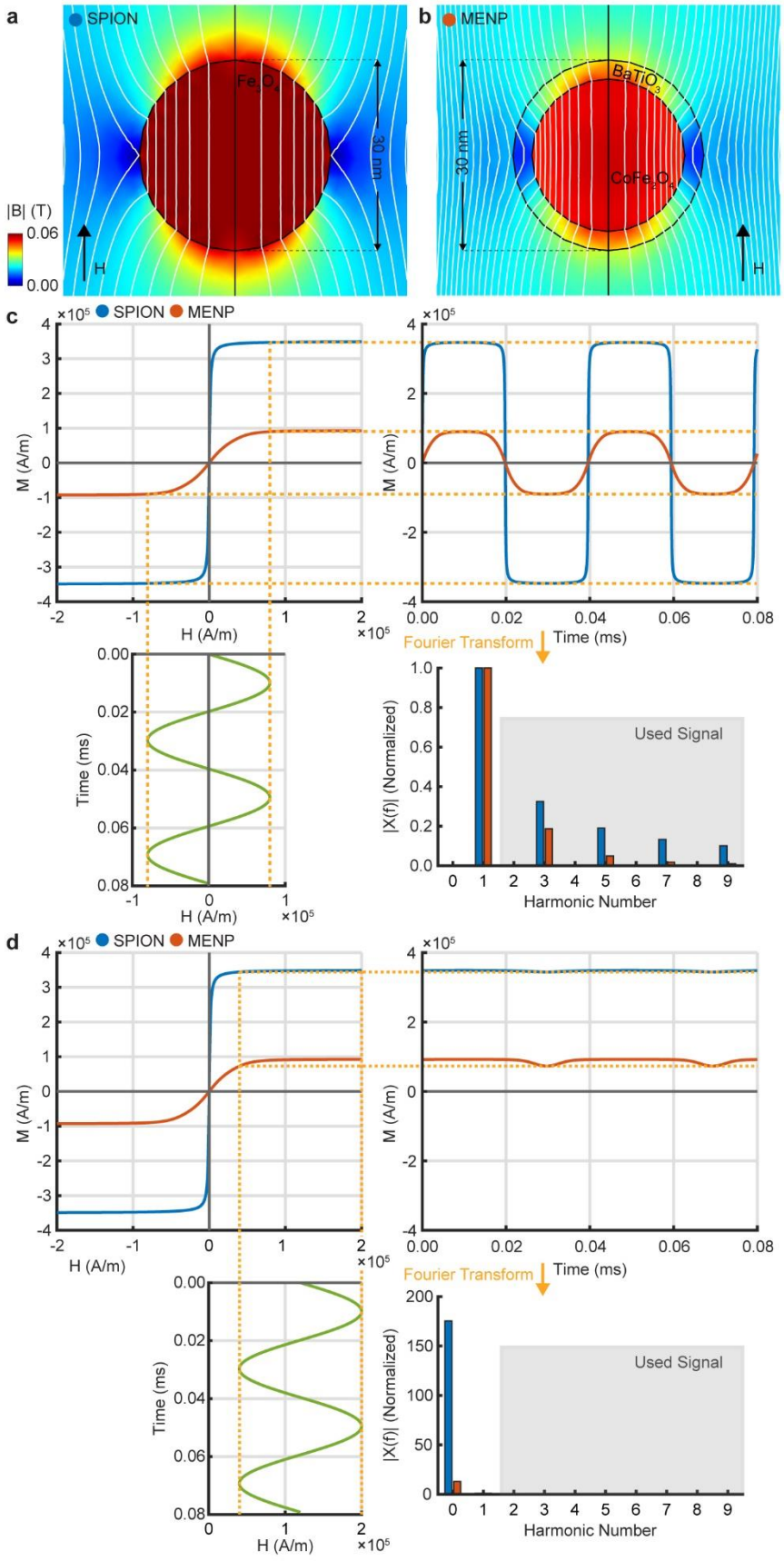
a
SPION
Fe_3O_4
30 nm
|B| (T)
0.06
0.00
H
b
MENP
$BaTiO_3$
30 nm
$CoFe_2O_4$
H
c
×10⁵ SPION MENP
M (A/m)
H (A/m)
×10⁵
Time (ms)
Fourier Transform
|X(f)| (Normalized)
Used Signal
Harmonic Number
d
×10⁵ SPION MENP
M (A/m)
H (A/m)
×10⁵
Time (ms)
Fourier Transform
|X(f)| (Normalized)
Used Signal
Harmonic Number

Figure 2: Magnetic flux density and magnetization harmonics for SPIONs and MENPs.

(a) Magnetic flux density amplitude of a 30 nm SPION in response to 40 kA/m *H*-field (white contour lines - magnetic flux lines). (b) Response of a 30 nm CFO-BTO MENP to the same field. (c) Nonlinear magnetization and Fourier transform harmonics for SPIONs and MENPs in response to a 25.25 kHz, 80 kA/m oscillating *H*-field. (d) Magnetization saturation for SPIONs and MENPs with a 120 kA/m bias field to a 25.25 kHz, 80 kA/m oscillating *H*-field. For (c) and (d) values are normalized to the first harmonic of each particle type.

Effect of Core Size on Magnetization Modulation in Magnetoelectric Nanoparticles

Previous simulations[55] and synthesis[78] of CFO-BTO MENPs with increasing core-shell ratios were shown to directly affect magnetoelectric coupling and can be leveraged to optimize the sensitivity of MENPs to neuronal electric fields. We evaluated the relationship between CFO core size and magnetic flux density amplitude in the presence of physiologically relevant electric fields ranging between 0 and 50 mV/mm (Fig. 3e). An electric field opposing a 4 kA/m *H*-field was applied to 30 nm MENPs with CFO core radii ranging between 5 and 12 nm corresponding to BTO shell thicknesses ranging between 10 and 3 nm (Fig. 3a-b, see also Fig. 14). Overall core-shell average magnetic flux density at 50 mV/mm increased with larger core sizes and ranged between 5.356 mT (5 nm) and 9.629 mT (12 nm) under the same electric field and antiparallel 4.0 kA/m *H*-field configuration (Fig. 3b). Average magnetic flux density in the core at 50 mV/mm remained relatively constant at between 13.92 mT (multiple sizes) and 14.08 mT (12 nm) independent of core size and consistent with the high permeability of CFO relative to BTO. We then quantified the magnetic flux density (Fig. 3c) and corresponding magnetization (Fig. 3d) for different core

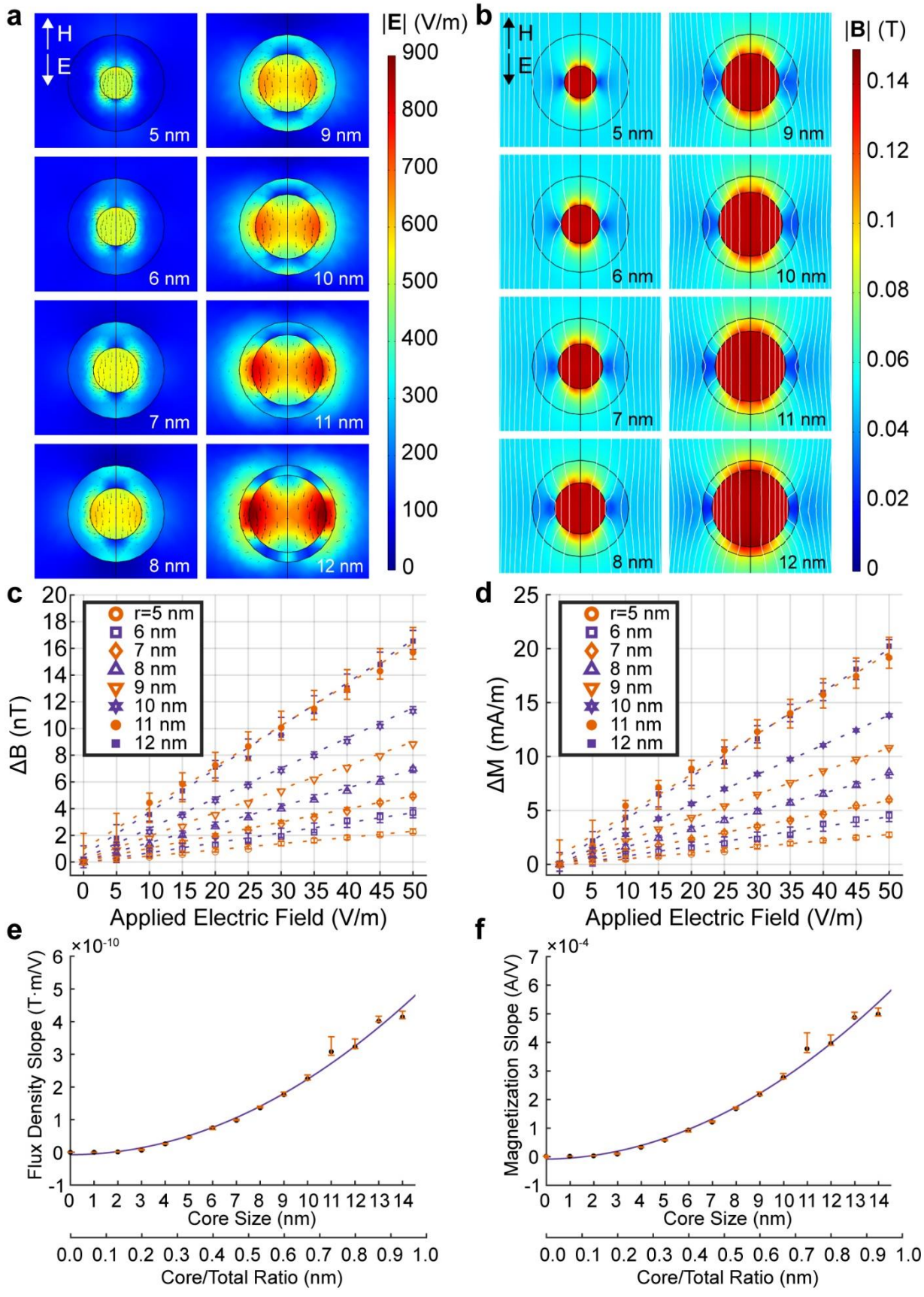
a
H
E
5 nm
9 nm
6 nm
10 nm
7 nm
11 nm
8 nm
12 nm
|E| (V/m)
900
800
700
600
500
400
300
200
100
0
b
H
E
5 nm
9 nm
6 nm
10 nm
7 nm
11 nm
8 nm
12 nm
|B| (T)
0.14
0.12
0.1
0.08
0.06
0.04
0.02
0
c
r=5 nm
6 nm
7 nm
8 nm
9 nm
10 nm
11 nm
12 nm
ΔB (nT)
Applied Electric Field (V/m)
d
r=5 nm
6 nm
7 nm
8 nm
9 nm
10 nm
11 nm
12 nm
ΔM (mA/m)
Applied Electric Field (V/m)
e
×10-10
Flux Density Slope (T·m/V)
Core Size (nm)
Core/Total Ratio (nm)
f
×10-4
Magnetization Slope (A/V)
Core Size (nm)
Core/Total Ratio (nm)

Figure 3: Effect of MENP core size on electric field-based magnetization modulation.

(a) The effect of core size on electric field magnitude (colormap) and direction (vectors) in response to external fields. The core radius ranged from 5 to 12 nm corresponding to shell thickness ranging from 10 to 3 nm. In all cases, E_z = -100 mV/mm antiparallel to H_z = 4 kA/m. (b) Magnetic flux density plots for the same configurations in (a). (c) Volume-averaged changes in magnetic flux in response to electric field for the same core sizes. (d) Volume-averaged changes in magnetization in response to electric field, across the same core sizes. (e) Slope of the magnetic flux modulation versus electric field linear slope. (f) Slope of the magnetization modulation versus electric field linear slope. For both (e) and (f), the abscissa is labeled with both core size and core/total ratio. Error bars denote 95% confidence intervals for all panels.

sizes in response to different electric fields ranging between 0 and 50 mV/mm. We find a nonlinear increase in sensitivity to electric fields reaching 0.414 nT·m/V and 0.497 mA/V for 30 nm CFO-BTO MENPs with 14 nm CFO core radius (Fig. 3e-f). Our findings correlate with similar magnetoelectric structures characterized elsewhere[79–90] and demonstrate comparable shell displacement (Fig. 15)[91], affirming that further optimization will require a large core-shell ratio.

Field Directionality-Dependent Magnetization Amplitude

MPI tomography relies on injected magnetic nanoparticles experiencing an externally applied *H*-field. Directionality of the external field applied on MENPs relative to *in situ* electric fields of diverse neuronal morphologies and orientations is expected to affect detectability. We explored this effect by modifying the angle θ between the electric field and *H*-field for MENPs (Fig. 4). For both electric field (Fig. 4a) and magnetic flux density (Fig. 4b) we find the maximum average effect at 0° and 180° of 539.82 V/m and 10.14 mT, respectively, minimized at 90° and 270° with values decreasing to 35.62 V/m and 0.13 mT (see Fig. 16 for corresponding magnetization plots and diagrams, and Movies S1-S3 for a 360° sweep of all three parameters). Average electric field and magnetic flux density across the particle (Fig. 4c) and decile plots (Fig. 4d) demonstrate that 50% of the magnetization occurs at 22.2% of the total volume of the particle at optimal angles, with 99.942% occurring at the core and 0.058% occurring at the shell. Our directionality estimates allow for proper quantification of the expected MPI signal recorded in response to electric fields generated by excitable cells with diverse compartmental anatomy in the presence of MENPs.

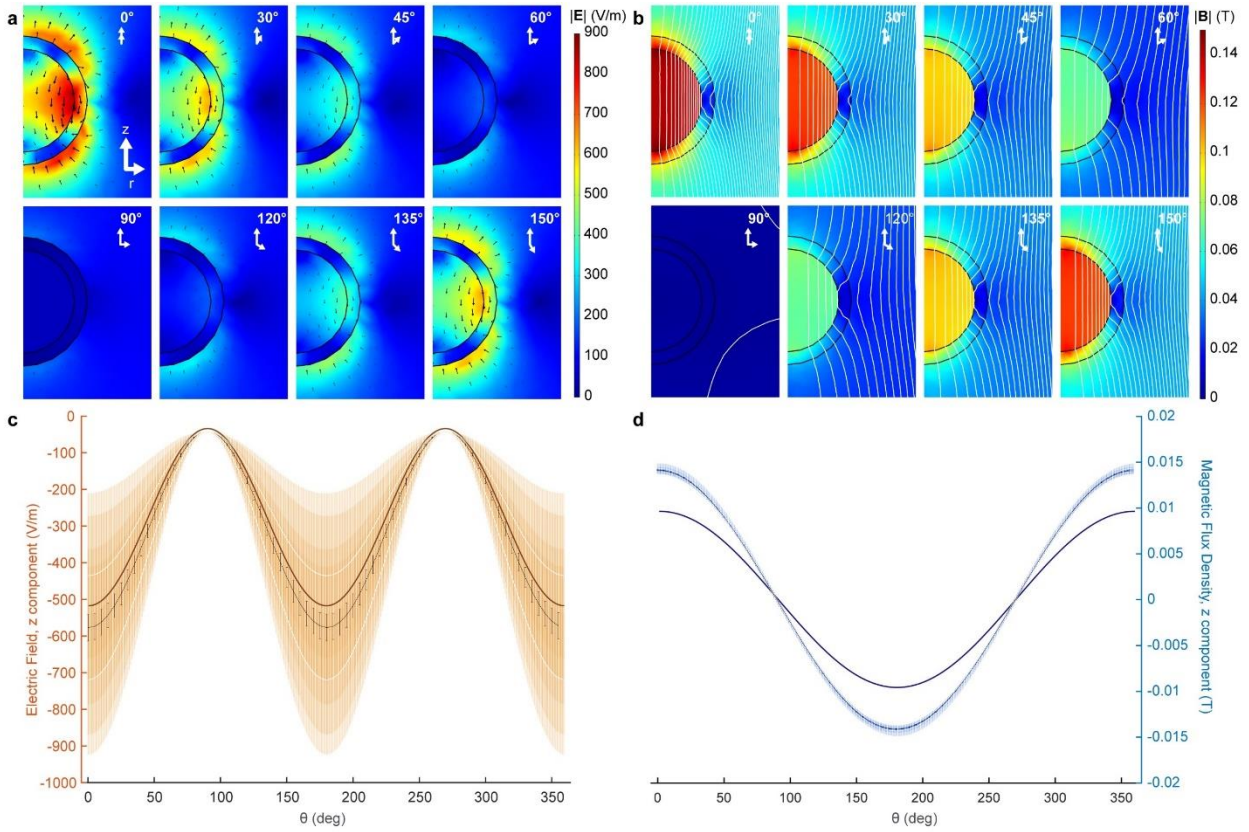

Figure 4: Effect of applied electric field and magnetic field intensity directionality on measured MENP electric field and magnetic flux density.

(a) Electric field norm and vector plots for selected angles (0°, 30°, 45°, 60°, 90°, 120°, 135°, 150°). (b) Magnetic flux density norm and contour plots for the same angles in (a). (c) Mean electric field z component (thick brown trace), interquartile range (thin black traces) and decile plot (shades of orange) relative to the angle between applied electric field and *H*-field. Deciles plotted are (0-100), (10-90), (20-80), (30-70), (40-60), and the mean (50 – central red trace). Deciles closest to the mean are not visible due to their low range. (d) A magnetic flux density plot for the same conditions as in (c); shown are mean magnetic flux density z component (navy blue), interquartile range (black), and deciles (shades of blue). Red error bars denote standard error of the mean for all panels.

Quantification of MENP Magnetization Response from Single Neurons

CFO-BTO MENPs in concentrations ranging between 50 and 200 μg/mL were demonstrated to be compatible with *in vivo* brain applications[56, 16, 60]. We turned to quantifying the expected magnetic field strength arising from the excitation of single neurons for sensing activity in the presence of CFO-BTO MENPs at comparable concentrations (Fig. 5). Maximal absolute magnetization during action potential peak integrated over the morphological volume was between 8.228×10^{-12} and 9.635×10^{-3} A/m surrounding neuronal somata, axons, and neurites of multiple cortical morphology types (layer 3, middle temporal gyrus; layer 6, middle temporal gyrus; layer 3, frontal lobe; layer 3, middle Frontal gyrus; Fig. 5a-d, n = 4 for each type) and varied significantly between all types ($F = 24.5$, $p = 7.90429\times10^{-16}$; one-way ANOVA, Fig. 5e). MENP concentration was 117.5 μM corresponding to 1415 particles/μm^2. Magnetization proximal (r = 20 μm) to somatic *in silico* compartments ranged between 1.901×10^{-6} and 2.147×10^{-4} A/m (absolute value), varying insignificantly between cell types ($F = 1.73$, $p = 0.21473$; one-way ANOVA). Absolute magnetization proximal to axons ranged between 1.033×10^{-7} and 1.016×10^{-4} A/m, also varying insignificantly between cell types ($F = 1.06$, $p = 0.40931$; one-way ANOVA). Absolute magnetization arising from dendritic trees, however, ranged between 1.749×10^{-8} and 2.714×10^{-5} A/m and varied significantly between cell types (MTG3, MTG6, FL3, MFG3; $F = 5.11$, $p = 0.01655$; one-way ANOVA). This magnetization corresponds maximally to 3.41 nM iron (20 nM Fe gives 5% of 4×10^{-9} T/μ_0 – the magnetization of a proton in a 1 T MRI field) and thus detectable fields by MPI[7] and MEG[92]. Significant differences between cell types and subcellular dendritic compartments indicate the ability to differentiate between cell types and brain regions by MENP magnetization amplitude.

Monte Carlo Simulations of Diffusing MENPs in Interconnected Neuronal Networks

To gain a realistic assessment of response to multicellular neural activity *in vivo*, we quantified magnetization of MENPs at a concentration of 27.5 μg/mL within a 700 μm deep cortical section comprising Layers II, III, and IV (150 μm, 350 μm, and 200 μm deep, respectively) and a total of 237,021 extracellular recording sites interspaced by 5 μm (Fig. 6). The network included excitatory and inhibitory cells similar to reported ratios[93, 94] spiking at overall frequencies of 5.30 Hz and 6.34 Hz and up to 16.77 Hz and 19.50 Hz during network bursts, respectively (Fig. 6a). Vectorized extracellular potentials served as inputs to the MENP directionality matrix (Fig. 5) for each recording site, enabling calculation of the magnetization at different coordinates within the cortical voxel over a 140 msec period (Fig. 5a, grayscales traces, magnetization at 237,021 recording sites). The mean signal arising from the network reached maximal amplitudes of 1354.34 μA/m (Fig. 6a, black trace) and mean amplitude of 219.8138 μA/m to 381.1203 μA/m during network bursts (Fig 6a, arrows, and Fig. 6b, four magnetization maps across a cortical slice corresponding to t = 27 ms, 59 ms, 91 ms, and 119 ms).

Nanoparticles injected intravenously travel through vasculature at speeds of 65 ± 12 cm/s[95], with a diffusion coefficient of 48 to 15 $\mu m^2/s$ for sizes ranging from 10.4 to 32.0 nm[3, 96]. We evaluated the signal arising from MENPs perfused through a cortical voxel at 650 μm/ms with a series of 40,000 Monte Carlo simulations of MENPs at the four network bursts originating from random coordinates in the x-z plane (y = 0) and propagating along the y axis over a 1.0 ms period centered at network burst peaks (Fig. 6c). The MENP signal arising from network activity with perfused MENPs reached a mean amplitude of 59.3402 to 417.6602 μA/m during network bursts (Fig. 6c). The maximum collective signal during network bursts arising from static MENPs relevant to particles penetrating through the blood-brain barrier[8] and settling in the brain

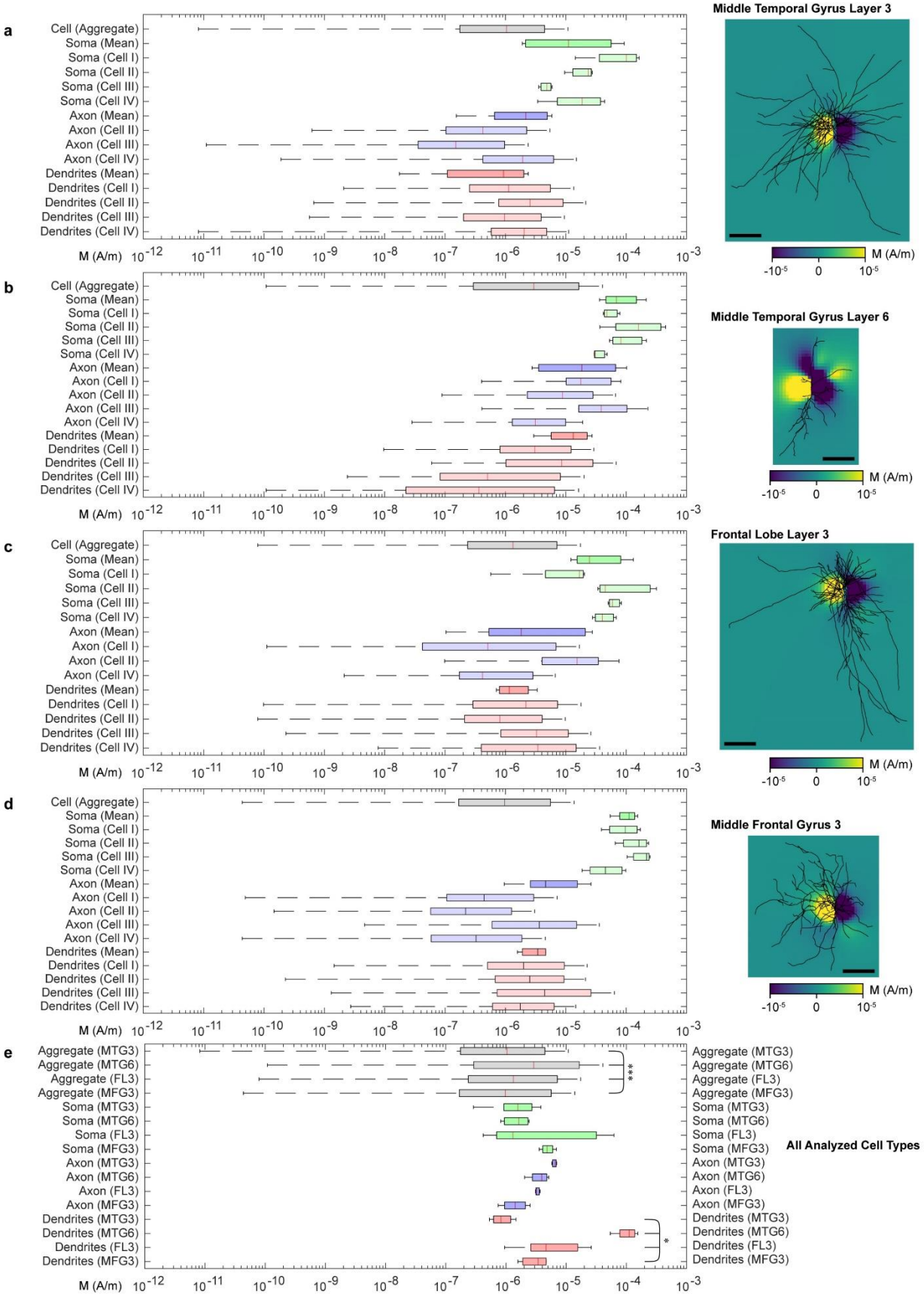
a
Cell (Aggregate)
Soma (Mean)
Soma (Cell I)
Soma (Cell II)
Soma (Cell III)
Soma (Cell IV)
Axon (Mean)
Axon (Cell II)
Axon (Cell III)
Axon (Cell IV)
Dendrites (Mean)
Dendrites (Cell I)
Dendrites (Cell II)
Dendrites (Cell III)
Dendrites (Cell IV)
M (A/m)
Middle Temporal Gyrus Layer 3
M (A/m)
b
Axon (Cell I)
Middle Temporal Gyrus Layer 6
c
Frontal Lobe Layer 3
d
Middle Frontal Gyrus 3
e
Aggregate (MTG3)
Aggregate (MTG6)
Aggregate (FL3)
Aggregate (MFG3)
Soma (MTG3)
Soma (MTG6)
Soma (FL3)
Soma (MFG3)
Axon (MTG3)
Axon (MTG6)
Axon (FL3)
Axon (MFG3)
Dendrites (MTG3)
Dendrites (MTG6)
Dendrites (FL3)
Dendrites (MFG3)
All Analyzed Cell Types

Figure 5: Distribution of magnetization from single spiking neurons.

Shown above are magnetization maps of a spiking cortical layer 3 middle temporal gyrus neuron (a), layer 6 middle temporal gyrus neuron (b), layer 3 frontal lobe neuron (c), and a layer 3 middle frontal gyrus neuron (d). Shown in right panels in (a)-(d) are magnetization magnitude and sign for a bias field in the x direction. The slices are taken from the x-z plane. The left panels show the absolute value magnetization mean (red line), 1^{st} and 3^{rd} quartiles (colored boxes), and outliers (Q1-1.5*IQR; Q3+1.5*IQR) for all regions of all cells, as well as for total aggregated data, on logarithmic scale. Scale bar = 200 μm for a, b, c, and d. e) Salient bar and whisker entries from cell types in panels a, b, c, and d. Note the statistical significance (* = $p < 0.05$, *** = $p < 0.001$, one-way ANOVA) between dendritic compartments and total cell aggregate data.

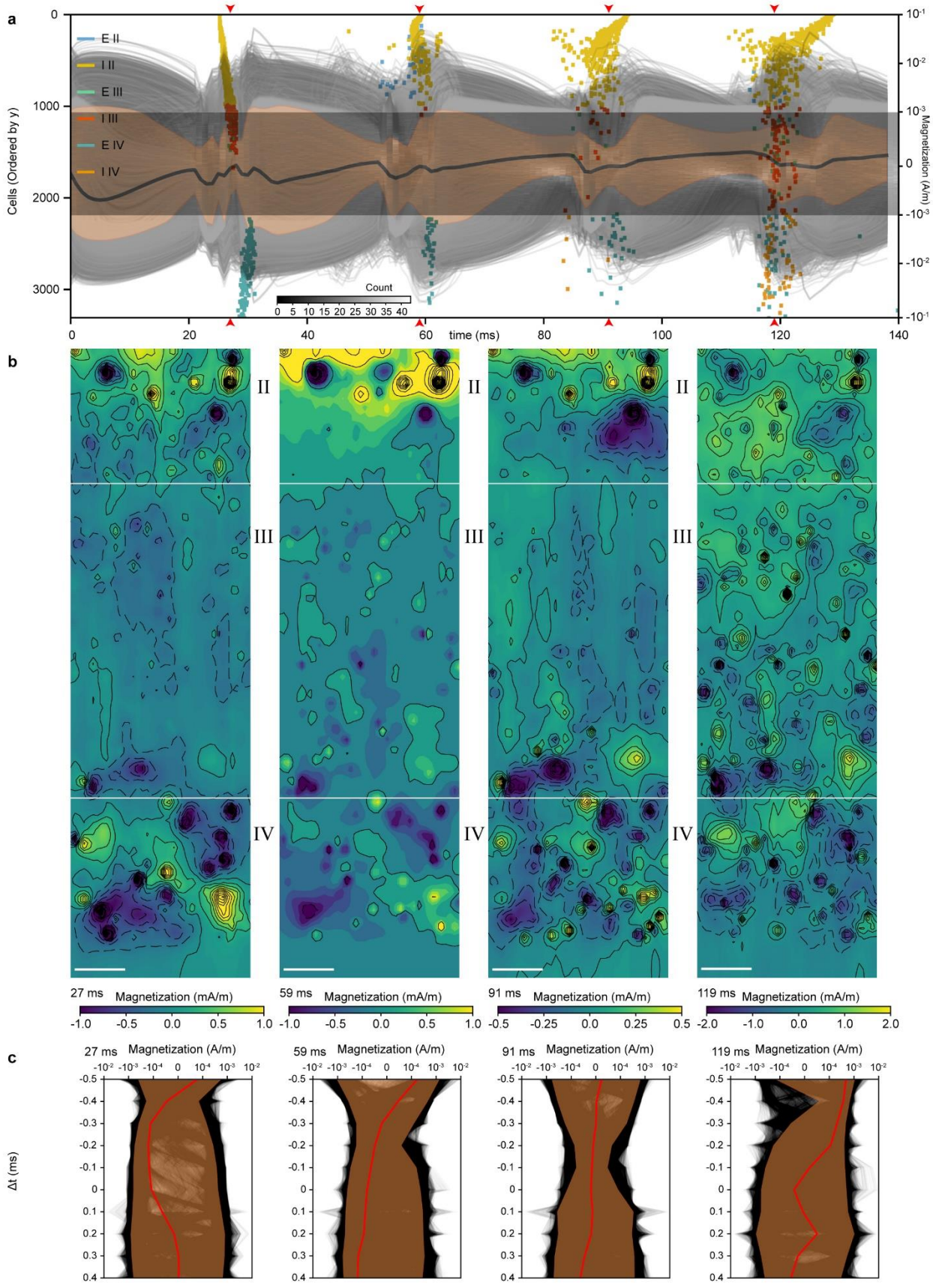
a
E II
I II
E III
I III
E IV
I IV
Cells (Ordered by y)
Count
0 5 10 15 20 25 30 35 40
time (ms)
Magnetization (A/m)
b
II
III
IV
27 ms Magnetization (mA/m)
59 ms Magnetization (mA/m)
91 ms Magnetization (mA/m)
119 ms Magnetization (mA/m)
c
Δt (ms)
27 ms Magnetization (A/m)
59 ms Magnetization (A/m)
91 ms Magnetization (A/m)
119 ms Magnetization (A/m)

Figure 6: Magnetization of MENPs within a simulated cortical voxel.

(a) Firing activity of neurons within the simulated neocortical slice (E = excitatory, I = inhibitory cells) over a 140 ms period. Layers II, III, and IV of the neocortex were simulated, each 150 μm, 350 μm, and 200 μm thick, respectively, (total thickness = 700 μm). Mean firing rates were 6.20 Hz and reached 19.13 Hz during network bursts. Composite magnetization traces (grayscale) overlaid on a time-dependent histogram (grayscale). Grayscale traces are the magnetization at recording sites color-coded by distance from the slice center (lighter = further from center). The thick black line is the mean magnetization in the slice, while the orange swath is the standard deviation. The time-dependent histogram covers the linear regime of the symmetric log plot (from -1 mA/m to 1 mA/m), with bin dimensions of 1 ms by 5 μA/m. (b) Static yz magnetization colormaps through x = 100 μm for each of four timepoints marked by red arrows in panel a). Scale bar = 50 μm. (c) Monte Carlo magnetization simulations for perfused MENPs. Single particles were centered at each of the four times (i.e. 27 ms, 59 ms, 91 ms, 119 ms) and traversed through the neural network vertically from the top (y = 0 μm) to bottom (y = 700 μm) edge. The thick red line is the mean magnetization, and the orange swath is the standard deviation.

interstitium was 36.5399 μA/m lower compared with perfused MENPs traveling through the vasculature and forms a more realistic estimation of using MENP-mediated MPI to record electrophysiological events.

Discussion

This study provides a realistic platform for quantifying the magnetization of magnetoelectric nanoparticles (MENPs) for sensing neurophysiological electric fields with cellular-level precision. We established a finite element strain-based model that emulates piezoelectric deformation of a BTO shell over a CFO nanoparticle core in response to small extracellular electric fields, giving rise to magnetic flux detectable by low-field modalities[97, 98] and suitable for brain recording. CFO-BTO MENPs modeled here are emerging as agents for brain applications[56, 16, 75] and are shown to traverse the blood-brain barrier with minimal adverse effects[8]. Other core-shell combinations are also being developed and offer increased magnetoelectric coupling with comparable biocompatibility[66, 69, 70]. Our model can be generalized for quantifying such diverse compounds by integration with more advanced time-domain equations[99, 100] and serve as a comprehensive tool for characterizing magnetoelectric materials and for quantifying sensitivity to biophysical phenomena in multiple systems.

Patterned magnetoelectric stacks[86, 101], nanowires[102], matrices[103, 104], and heterostructures[81, 105–107] are of particular interest and were introduced as more versatile and scalable platforms responsive to electric fields. These can serve as multiplexed arrays for spatially precise readouts and stimulation of neural activity, and integrate with other magnetoelectric technologies for brain recording[17, 57, 108] and stimulation[56, 64, 109]. Finite element three-dimensional analyses can be specifically leveraged to characterize diverse device geometries in

addition to simple core-shell particles shown here and can be used for optimized sensing of biogenic electric fields.

Our particle model predicts magnetization of MENPs at a physiological concentration of 117.5 μM (27.495 μg/mL) administered extracellularly to excitable neurons with diverse morphologies. We predict an 8.228×10^{-12} to 9.635×10^{-3} A/m response from single neurons at peak membrane depolarization, and 59.3402 to 417.6602 μA/m across a 200 × 700 × 200 μm^3 voxel for multicellular interconnected networks of neurons mimicking *in vivo* scenarios. Sensitivity of detection and spatiotemporal resolution in MPI depend on nanoparticle size[110]. A concentration of 5 mg/mL for nanoparticle diameters of 18.5 nm to 32.1 nm[110–114] corresponds to a FWHM of 16.7 mT/μ_0 to 25.1 mT/μ_0 respectively at 20.25 kHz with a 20 mT input sinusoid, for single volumetric acquisitions. Modulation of 10 mA/m in MENPs is equivalent to a concentration difference of 0.933 ng/mL for simple SPIONs detectable in MPI[114, 115]. Our results suggest sufficient sensitivity to extracellular electric fields assuming MENP concentrations greater than 117.5 μM (27.495 μg/mL) for stationary MENPs and intravenously perfused MENPs. MENPs localized directly on the plasma membrane can increase detectability further assuming particles experience electric fields that correspond to full intracellular membrane potential differences[75]. Wang et al. report 0.3 emu/g saturation for MENPs (1.8 kA/m assuming the particle has a density close to CFO of 6.02 g/cc[116]) for an immobilized single-layer array[117] and Etier et al. report 20 emu/g (120.4 kA/m assuming the same) for both a loose powder and fixed powder. Etier et al. note that hysteresis is not present in the loose powder, because the particles can freely rotate[118]. This is as seen clinically *in vivo*, which our model represents. The temporal resolution for single point recordings used in MPI spectroscopy reaches sub-millisecond scales[119] and exhibits

negligible hysteresis at neuronal time scales[120], allowing for improved temporal sensitivity even to single field potential events.

Existing particle-based neuroimaging systems for neurochemical and neurophysiological readouts require hundreds of milliseconds for single acquisitions[28, 121] and can be enhanced by the high temporal resolution of MENP-based MPI technology. Voltage-sensitive MENPs can also increase coverage in the brain and supplement voltage-sensitive optical dyes currently used as injectable or genetically expressed agents for cell-type-specific readouts[122], in addition to established optogenetic tools for neural stimulation[123]. MENPs are capable of bidirectional brain recording and stimulation and can thus serve as magnetoelectric equivalents of optical tools, enabling greatly increased recording depth and signal penetration.

Conclusion

Magnetoelectric materials are increasingly used for biomedical sensing and modulation, and provide minimally invasive access to different organ systems and the brain in particular. In this study, we describe an *in silico* characterization framework to asses the response of cobalt ferrite (CFO) barium titanate (BTO) core-shell magnetoelectric nanoparticles (MENPs) to neural electric fields and investigate feasibility for wireless electrophysiological readouts using injectable magnetoelectric agents. The magnitude of magnetoelectric coupling from different core-shell ratios is analyzed and optimized, and the direction-dependent electric and magnetic field distributions are presented. The resulting time-dependent magnetoelectric responses from single neuronal morphologies and realistic neural networks during MENP perfusion were statistically quantified, and the induced magnetic fields were found to be within the detectability limits of magnetic particle imaging (MPI). Our model is applicable to numerous other geometries and

material configurations, enabling the validation of other potential magnetoelectric transducer designs and the advent of novel applications of magnetoelectric materials in biomedicine.

Methods

Nanoparticle Modeling

A strain-based finite element model was applied to simulate the magnetoelectric effect for CFO-BTO and SPIO nanoparticles using custom equations in COMSOL Multiphysics 5.6 (COMSOL Inc. Stockholm, Sweden). The Langevin equation was employed to derive the M-H curve for the SPION model[124]. The M-H relationship for BTO was acquired by tracing an M-H curve based on previous studies[125]. For CFO-BTO, two concentric spheres were formed, the inner sphere representing magnetostrictive CFO and the outer shell representing piezoelectric BTO. The *Electrostatics*, *Magnetic Fields*, and *Solid Mechanics* modules were used, along with *Magnetostriction* and *Piezoelectric Effect* multiphysics couplings. Electrostatic modeling of non-piezoelectric media used the *Charge Conservation* boundary condition and was based on Gauss's Law:

$$\nabla \cdot \vec{\boldsymbol{D}} = \rho_v \tag{1}$$

where ∇ is the del operator, $\boldsymbol{D}$ is the electric flux density and ρ_v is the volume charge density. Modeling with piezoelectric media used linear piezoelectric coupling (boundary condition: *Charge Conservation, Piezoelectric*):

$$\nabla \cdot \left(\epsilon_0 \vec{\boldsymbol{E}} + \epsilon_0 \chi_{rs} \vec{\boldsymbol{E}} + \boldsymbol{e}\colon \boldsymbol{\varepsilon}\right) = \rho_v \tag{2}$$

where ϵ_0 is the electric permittivity, $\boldsymbol{E}$ is the electric field intensity, χ_{rs} is the relative electrical susceptibility, $\boldsymbol{e}$ is the piezoelectric Voigt coupling matrix representing the stress tensor, and $\boldsymbol{\varepsilon}$ is the strain tensor. Magnetic field modeling was performed based on Ampere's Law:

$$\vec{\boldsymbol{B}} = \nabla \times \vec{\boldsymbol{A}} \tag{3}$$

and

$$\nabla \times \vec{\boldsymbol{H}} = \vec{\boldsymbol{J}} \tag{4}$$

$$\vec{\boldsymbol{J}} = \sigma\vec{\boldsymbol{E}} + \sigma\vec{\boldsymbol{v}} \times \vec{\boldsymbol{B}} + \vec{\boldsymbol{J_e}} \tag{5}$$

where $\boldsymbol{B}$ is the magnetic flux density, $\boldsymbol{A}$ is the magnetic vector potential, $\boldsymbol{H}$ is the magnetic field intensity, $\boldsymbol{J}$ is the electric volumetric current density, σ is the electrical conductivity, $\boldsymbol{v}$ is net charge velocity, and $\boldsymbol{J_e}$ is electron current density. The constitutive relation between magnetic flux density, magnetic field intensity, and magnetization varied by domain. For cerebrospinal fluid (boundary condition: *Ampere's Law*),

$$\vec{\boldsymbol{B}} = \mu\vec{\boldsymbol{H}} \tag{6}$$

the BTO shell (boundary condition: *Ampere's Law*),

$$\vec{\boldsymbol{B}} = \mu_0\,(\vec{\boldsymbol{H}} + \vec{\boldsymbol{M}}) \tag{7}$$

and for the CFO core (boundary condition: *Ampere's Law, Magnetostrictive*),

$$\vec{\boldsymbol{B}} = \mu_0\,(\vec{\boldsymbol{H}} + \vec{\boldsymbol{M}}(\vec{\boldsymbol{H}}, \boldsymbol{S})) \tag{8}$$

respectively, where μ is the magnetic permeability, $\boldsymbol{M}$ is the magnetization, and $\boldsymbol{S}$ is the stress tensor (see Eq. 12 and Eq. 14). For modeling linear elastic media (boundary condition: *Linear Elastic Material*),

$$0 = \nabla \cdot \boldsymbol{S} + \boldsymbol{F_v} \tag{9}$$

$$\boldsymbol{\varepsilon} = \frac{1}{2}[(\nabla\vec{\boldsymbol{u}})^T + \nabla\vec{\boldsymbol{u}}] \tag{10}$$

where $\boldsymbol{F_v}$ is the volume deformation tensor and $\boldsymbol{u}$ is the solid displacement vector. Piezoelectric stress was modeled by (boundary condition: *Piezoelectric Material*)

$$\boldsymbol{S} = S_0 + \vec{\boldsymbol{C}}\colon \boldsymbol{\varepsilon} - \vec{\boldsymbol{E}} \cdot \boldsymbol{e} \tag{11}$$

(where S_0 is the initial stress, and $\boldsymbol{C}$ is the elastic right Cauchy deformation tensor) and for magnetostrictive stress (boundary condition: *Magnetostrictive Material*)

$$\boldsymbol{S} = S_0 + \boldsymbol{c_H}\colon [\boldsymbol{\varepsilon} - \boldsymbol{\varepsilon_{me}}(\vec{\boldsymbol{M}})] \tag{12}$$

where $\boldsymbol{c_H}$ is the elasticity tensor, and $\boldsymbol{\varepsilon_{me}}$ is the magnetostrictive strain,

$$\boldsymbol{\varepsilon_{me}} = \frac{3}{2}\frac{\lambda_s}{M_s^2} dev\ (\vec{\boldsymbol{M}} \otimes \vec{\boldsymbol{M}}) \tag{13}$$

where λ_s is the saturation magnetostriction, and M_s is the saturation magnetization, matching the behavior of CFO nanoparticles in dispersion. Furthermore,

$$\vec{\boldsymbol{M}} = M_s L\ (|\vec{\boldsymbol{H}}_{\boldsymbol{eff}}|)\frac{\vec{\boldsymbol{H}}_{\boldsymbol{eff}}}{|\vec{\boldsymbol{H}}_{\boldsymbol{eff}}|} \tag{14}$$

where L is the Langevin function, and

$$\vec{\boldsymbol{H}}_{\boldsymbol{eff}} = \vec{\boldsymbol{H}} + \frac{3\lambda_s}{\mu_0 M_s^2} dev(\boldsymbol{S})\vec{\boldsymbol{M}} \tag{15}$$

All established parameters used in the model can be found in Table 1.

Table 1: Parameter values and respective sources for all material constants used within COMSOL

	Barium Titanate	Cobalt Ferrite
Electrical Conductivity	10^{-7} [S/m] [126]	4.2×10^{-5} [S/m] [127]
Initial Magnetic Susceptibility	Not applicable	70 [128]
Saturation Magnetostriction	Not applicable	315 [ppm] [129]
Density	5700 [kg/m^3] (COMSOL)	6060 [kg/m^3] [116]
Saturation Magnetization	Not applicable	181800 [A/m] [130]
Poisson's Ratio	Not applicable	0.33 [131]
Relative Permittivity	[1115.1, 1115.1, 1251.3] (COMSOL)	[9.0355, 9.0355, 10.5037] [132]
Young's Modulus	Not applicable	188.4 [GPa] [133]
Elasticity matrix, Voigt notation	[150.377, 656.308, 150.377, 65.9391, 65.9391, 145.521, 0, 0, 0, 43.8596, 0, 0, 0, 0, 43.8596, 0, 0, 0, 0, 0, 42.3729] [GPa] (COMSOL)	Not applicable
Coupling matrix, Voigt notation	[[0, 0, -4.32015, 0, 0, -4.32015], [0, 0, 17.3624, 0, 11.4035, 0], [11.4035, 0, 0, 0, 0, 0]] [C/m^2] (COMSOL)	Not applicable

Table 1: Parameter values and respective sources for all material constants used within COMSOL

Harmonics measurements of SPIONs and MENPs employed a time-dependent study with f = 25.25 kHz based on the M-H curve of CFO nanoparticles[116] corresponding to the Langevin function and the negligible magnetic susceptibility of the BTO shell. The time step was 1 μsec and the time range was 0 to 80 μsec. The surrounding electrolyte medium was modeled as cerebrospinal fluid, and a cylindrical infinite element domain shell was placed outside the main rectangular region. The *Magnetic Field* boundary condition was applied to all faces immediately inside the infinite element domain, and electric fields were generated by the *Electric Potential* boundary condition applied to the top and bottom faces (Fig. 17). Rotation effects were modeled by fixing the applied electric field and rotating the applied magnetic field. Moreover, only coordinates within the particle were sampled for mean and decile plots, and a physics-controlled mesh with normal element size was used. Both stationary and time-dependent studies used a fully-coupled automatic highly nonlinear Newton node with an iterative linear FGMRES solver.

Core Size Trend Analysis

For core-shell CFO-BTO nanoparticles, the electric field and magnetic flux density plots for core radii ranging between 5 nm and 12 nm were modeled by changing the size of the inner semicircle (CFO) while maintaining the overall radius at 15 nm. 95% confidence intervals were defined as twice the standard error of either regression data or the regression slope. For the slope trend analysis, core sizes were simulated from 0 to 14 nm in increments of 1 nm. Core sizes larger than 14 nm had poor convergence due to numerical instability and were thus excluded from the analysis. Core size-dependent magnetization and magnetic flux density modulation slopes were derived using linear regression. The trend of these slopes with respect to core size was defined as

the second derivative of magnetization (or magnetic flux density) and derived using quadratic curve fitting.

Neuronal Magnetization Simulations

Nanoparticle magnetization changes were linearly mapped to electric field magnitude: a 0.02 A/m magnetization change per 50 mV/mm for a 12 nm core size was used, and the observed direction-dependent effect was applied. Electric field vectors were computed as the gradient of simulated extracellular voltage, and open-source Python libraries LFPy[134] and NetPyNE[135] were used for simulations of extracellular voltage around single neuronal morphologies and neural networks, respectively, integrated with the neural biophysics simulator NEURON[136]. MENP concentration was maintained at 117.5 μM (27.495 μg/mL), corresponding to 1415 particles/μm^3.

Neuronal Morphologies

Biophysical parameters involving Allen Brain Atlas morphologies were obtained from previous studies[137]. The geometries were manually aligned to a three-dimensional template soma and simulated using Python LFPy[134] and NEURON[136]. Human middle temporal gyrus layer 3, middle temporal gyrus layer 6, frontal lobe layer 3, and middle frontal gyrus layer 3 cells were simulated (n = 4 each). Action potentials were induced by raising the membrane potential, raising the sodium Nernst potential, and lowering the potassium Nernst potential. A 20 μm inclusion zone around subcellular compartments defined somatal, axonal, and dendritic voxel categories. Magnetization was quantified during the largest action potential peak within the first 20 ms, and the mean values for each cell compartment class were grouped in aggregate to define the significance between cell types. One-way ANOVA (*anova1*) in MATLAB R2021a (The MathWorks, Inc. Natick, MA, USA) was used to determine significance between cell type groups,

with three different biophysical parameter sets yielding equivalent quantification significance outcomes.

Monte Carlo Simulations of Realistic Neural Networks

Volumetric simulations were performed by reconstructing rat neocortical architecture[138] using the Python library NetPyNE[135]. A 200 μm by 200 μm column of neocortex layers II, III, and IV was simulated, with depths of 150 μm, 350 μm, and 200 μm (total depth was 700 μm), and Excitatory:Inhibitory/Total ratios of 895:95/990, 988:188/1176, and 970:170/1140, respectively. Excitatory synapses were NMDA receptor-based (τ_1 = 0.8 s, τ_2 = 5.3 s, V_{rest} = 0 mV) and inhibitory synapses were GABA receptor-based (τ_1 = 0.6 s, τ_2 = 8.5 s, V_{rest} = -75 mV). Excitatory cells were interconnected while inhibitory cells were only connected to excitatory cells. Excitatory synapses had a weight of $25 \times y_{norm}$ mV (y_{norm} is the normalized neuronal depth) and a connection probability of p = 0.1, while inhibitory synapses had a weight of 5 mV and a connection probability of $p = 0.4e^{-d/\lambda}$ (d is the synaptic distance; λ is the length constant of 150.0 μm[135, 138]). The simulation time step was 100 μs and the extracellular voltage was recorded with a resolution of 5 μm and 1 ms. Nanoparticle concentration was maintained at 27.495 μg/mL. 40,000 particles were normally distributed within the x-z plane (200 μm × 200 μm), with the particle movement modeled by a diffusion coefficient[96] D = 15 $\mu m^2/s$ and a perfusion velocity[95] of 650 μm/ms.

Author Contributions

AH and IB designed the research. IB, IH, and XQ performed the research. AH and IB wrote the manuscript.

Acknowledgments

This work was supported by the National Institute of Neurological Disorders and Stroke and the Office of the Director's Common Fund at the National Institutes of Health (grant DP2NS122605 to AH), the National Institute of Biomedical Imaging and Bioengineering (grant K01EB027184 to AH), the Wisconsin Alumni Research Foundation (WARF) and a Graduate Research Award from the Global Health Institute to IB.

Chapter 2: Nanofabricated Magnetoelectric Structures for Electric Field Sensing

***I. Bok**, T. Zhu, A. Vareberg, A. Hai;

Abstract

Electric field sensing and magnetic field modulation using magnetoelectric heterostructures hold great potential to accelerate high density spintronics, neuromorphic computing, medical imaging and stimulation. However, sensitivity limits and their relationship to geometric and material composition are poorly characterized, precluding the full recruitment of the technology. Here we perform sensitive magnetic force microscopy measurements of geometrically optimized nanofabricated magnetoelectric designs and determine magnetic dipole emergence in response to *in situ* electric fields, revealing a high degree of spatial consistency and radius- and electric-field-dependent modulation. We find exceptional agreement between our measurements and finite element modeling and build upon these findings to investigate more involved geometries. Our results show promise for raising sensitivity to the order of single mV/mm regime relevant to biology and empower new magnetoelectric nanostructure designs and compositions capable of revolutionizing the status quo of novel magnetoelectricity-based technologies.

Introduction

Newly developed magnetoelectric composites are empowering diverse technologies spanning quantum computing[139–143], imaging[144, 145] and medical therapeutics[64, 56, 146, 147]. By harnessing carefully controlled spin power conversion[148–150] and electric field-mediated topological modulation with minimal heating[141, 151–153], rapid nucleation of spin states can be achieved with tailored stability[154, 155] and provide unprecedented platforms to supplant existing sensing capabilities and alter the digital *status quo*. Notwithstanding these advances, the synthesis and characterization of highly responsive magnetoelectric heterostructures, and in particular customizing their sensitivity to a precise range of electric fields, have been challenging, despite playing an integral role in fulfilling the full potential of the technology.

Performance is most directly described by the magnetoelectric coupling coefficient (α) defined as the change in electric field per change in applied magnetic field ($\delta E/\delta H$) which varies by field strength, orientation, DC bias field, and AC frequency. Coupling measurements have been performed using diverse modalities including vibrating sample magnetometry[65, 156], superconducting quantum interference device (SQUID) magnetometry[66], or more recently magnetic force microscopy (MFM)[157], piezoresponse force microscopy (PFM)[103], and optically detected magnetic resonance (ODMR)[150, 155]. These techniques have been used to quantify the magnetoelectric sensitivity of innovative heterostructures such as barium titanate (BTO)/iron oxide[65, 66] (α = 28.78 mV/cm·Oe, E ≈ 9 kV/cm), cobalt-doped $BiFeO_3$[67, 68] (α = 6.5 V/cm·Oe, E ≈ 20 kV/cm), and cobalt ferrite (CFO)/BTO/polydopamine-P(VDF-TrFE)[69] (α_{E33} = 150.58 mV/cm·Oe, E ≈ 80 MV/m), often revealing improved coupling properties. However, these and similar composites are mostly stochastic in design and geometrically coarse, thus offering limited uniformity and control over magnetoelectric properties, and operate around the

MV/m electric field regime. More diverse geometries such as stacks (α = 142.6 mV/cm·Oe, E ≈ 110 MV/m) [158, 159], nanowires (α = 514 ± 27 mV/cm·Oe, E ≈ 2 kV/cm) [102, 160], and matrices (α = 1.4 × 10^6 mV/cm·Oe, E ≈ 140 MV/m)[103] have been developed as tailored alternatives but are often micron- to millimeter scale and operate at similarly large electric fields. Cutting-edge composites such as Y-type hexaferrite $Ba_{0.8}Sr_{1.2}Co_2Fe_{12-x}Al_xO_{22}$ with $x = 0.9$ (BSCFAO)[157] (ΔM = ~2 μ_B per f.u. at 100 K, $\Delta E \approx 5$ MV/m) with microscale interleaved phase domains and polycrystalline film of Ni on a $0.68Pb(Mg_{1/3}Nb_{2/3})O_3$-$0.32PbTiO_3$ substrate[156] (α = 1.6 × 10^{-6} s / m, E ≈ 1 MV/m) are uncovering intricacies of the magnetoelectric effect although they require complex synthesis techniques and are difficult to utilize.

Recently, superior geometries have been achieved using electron beam nanolithography enabling magnetoelectric spin-orbit (MESO) nanodevices for ultra-low power (down to attojoule) magnetization switching due to tight interfacial coupling between $BiFeO_3$ and cobalt-iron alloy[150, 161]. The precise features of the devices enable efficient spin cycloid-based switching in response to externally applied fields as verified by PFM and MFM. This adds to other examples of nanopatterened magnetoelectrics that do not require feature alignment or etching[162]. CFO-PZT magnetoelectric rings have been nanofabricated by leveraging a bilayer of resist materials with varying electron beam sensitivity to create a structural undercut that can be filled with piezoelectric PZT and then occupied with magnetostrictive CFO. These examples emphasize the advantage of using precision fabrication techniques to enable the creation of topographically well-defined structures, which, if properly characterized, can unlock the exploration of a wider parameter space for optimized designs.

Here we present a first and fundamental MFM characterization of electric field dose sensitivity of magnetoelectric nanoring structures realized by nanolithography, by applying a precise range of

electric fields directly to the device substrate containing geometrically-varied nanoring arrays. Our MFM scans reveal clear electric-field dependent dipole and magnetoelectric modulation from single CFO/BTO core/shell structures in agreement with finite element modeling. Moreover, our analyses of MFM data reveal diameter- and electric field-dependent magnetoelectric modulation providing the basis for applications involving multiplexing. Finally, we perform a geometric exploration of magnetoelectric nanostructures with increased layer count thereby informing future fabrication efforts. Our methodologies and results shed new light on the effect of structure geometry on electric field responsivity in magnetoelectric heterostructures and open new routes for improved devices across a slew of rapidly emerging fields.

Results

Geometric Optimization and Topographic Characterization of Nanofabricated Magnetoelectric Rings

The geometric parameters and resulting nanofabricated core-shell CFO-BTO structures for electric field sensing are characterized in Fig. 7. The nanofabrication process is introduced in Fig. 7a with fabrication steps presented sequentially from top to bottom. Plotted in Fig. 7b is the dependence of magnetization modulation on nanoring diameter and height in response to a 5 kV/m electric field in the ***-z*** direction according to finite element analysis. Within the region displayed, magnetization modulation increases with increasing nanoring height and radius. A scanning electron microscopy (SEM) image of an array of nanorings and an inset of a single nanoring with clear delineation between its core (CFO), shell (BTO), and substrate (SiO_2) are presented in Fig. 7c. These regions are explicitly labeled in Fig. 7d where an atomic force microscopy (AFM) scan is overlaid on the SEM image from Fig. 7c inset with the tallest region displayed with higher

magnification in Fig. 7e. By radially unwrapping the AFM image superimposed the SEM image we determine that the mean radial AFM magnitude for this nanoring ranges between 17.46 nm and 22.33 nm (19.38 ± 1.39 nm : $\mu(\mu) \pm \sigma(\mu)$) and the standard deviation ranges between 5.86 nm and 11.10 nm (8.41 ± 1.54 nm : $\mu(\sigma) \pm \sigma(\sigma)$) (Fig. 7f), with a maximum measured height of 40.02 nm (47.76 nm for all rings) representing significant uniformity with respect to angle. Our rigorous assessments form a robust justification for fabricating larger rings with increasing height. To build on these initial results, we proceeded to perform detailed MFM imaging of electric field response of single rings.

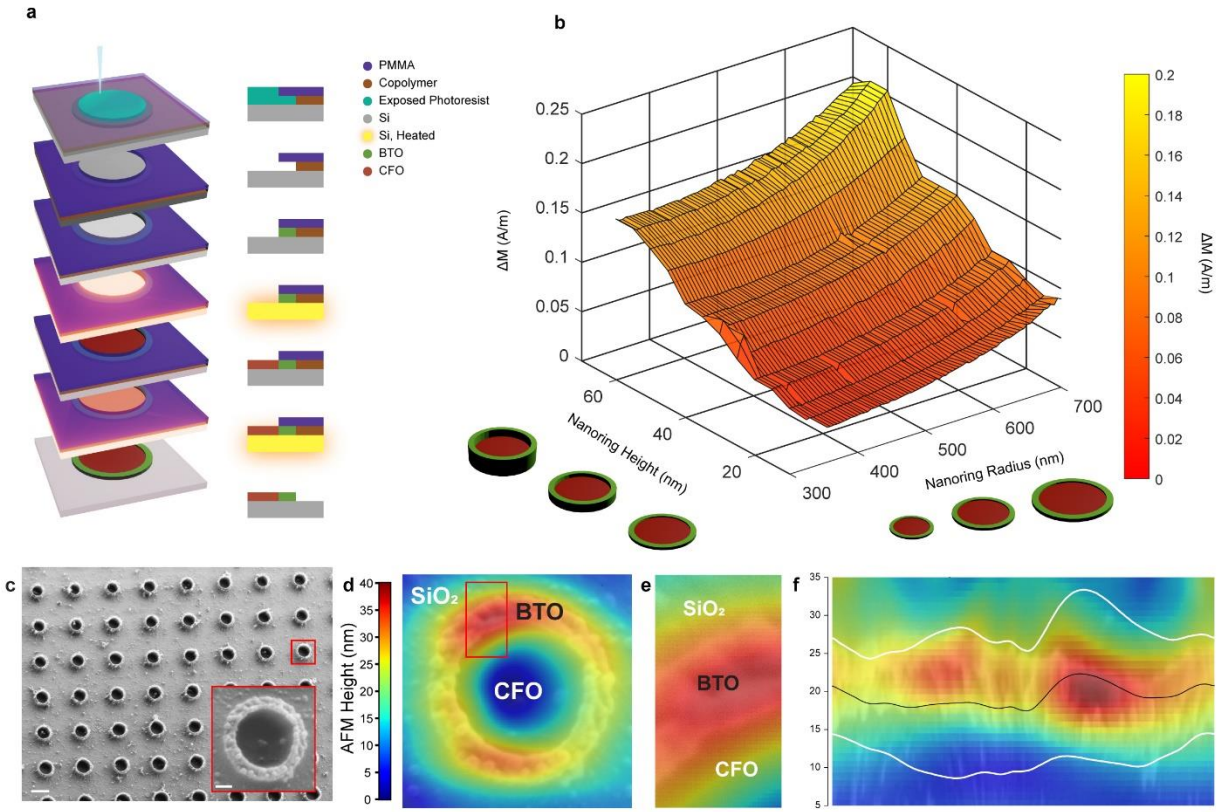

Figure 7: Geometric Optimization and Topographic Characterization of Nanofabricated CFO-BTO Rings.

(a) Fabrication process diagram consisting of the following steps from top to bottom (see Methods for more details): expose PMMA/copolymer bilayer; develop using MIBK/IPA; spin coat BTO; bake sample; spin coat CFO; bake sample; liftoff using acetone. (b) surface plot of magnetization modulation versus nanoring radius and height, in response to a 5 kV/m electric field in the ***-z*** direction. Within this region, magnetization modulation increases with increasing nanoring height and radius. (c) Scanning electron microscopy (SEM) images of nanorings (scale bar = 1 μm) including inset (red) of single nanoring (scale bar = 200 nm). (d) AFM scan overlaid on SEM image of ring from inset panel (c) with the tallest region displayed with higher magnification in (e). (f) Anisotropy line plot of radially unwrapped overlaid AFM and SEM images, with y-axis

labels corresponding to line graph of mean (black line) and standard deviation (white lines) with respect to angle.

Radius- and Electric Field-Dependent Magnetoelectric Modulation from Single Nanofabricated Rings

To accurately characterize electric field-dependent magnetoelectric modulation, we turned to applying static electric fields onto wafer substrate containing an assortment of CFO-BTO arrays and imaged the resulting magnetization change using MFM (Fig. 8). The configuration is depicted at the microscale in Fig. 8a with an exploded view of a single-ring perspective outlined in red. Fig. 8b highlights a close vantage point including BTO (pale green), CFO (light brown), and the silicon oxide (SiO_2) wafer substrate (gray). Using this configuration, electric fields of 7.97 V/mm, 15.46 V/mm, 24.22 V/mm, and 32.99 V/mm were applied to samples of geometrically precise arrays of nanorings with varying radii (728, 778, 828, 878, 928 nm). By subtracting images with applied electric field from baseline, we found a trend of increasing modulation with increasing electric fields and higher sensitivity for larger sizes (Fig. 8c). More specifically, at the lowest electric field of 7.97 V/mm, we observed a $\boldsymbol{\Delta M}$ of 545.19, 439.28, 320.08, 298.49, and 343.99 A/m for the diameters tested. At the highest electric field of 32.99 V/mm, we observed a $\boldsymbol{\Delta M}$ of 1297.04, 1649.56, 1487.65, 1720.22 A/m. This equates to a difference in $\boldsymbol{\Delta M}$ of 751.85, 1210.27, 1372.27, 1189.16, 1376.23 for 728, 778, 828, 878, 928 nm diameter rings, respectively. Corresponding scans reveal a prominent dipole in Fig. 8d(i-iv) (identical ranges) and Fig. 8d(v-viii) (adjusted ranges) which graphically illustrate increasing magnetoelectric modulation with increasing electric field strength. With negligible effects of external fields and assuming $\mu = \mu_0$, these values lie near the millitesla regime (1 kA/m ≈ 12.57 Oe = 1.257 mT).

Based on these results, we turned to quantifying the dependence of nanoring magnetization modulation on device radius. Fig. 8e demonstrates magnetization change with respect to nanoring size between designated electric field values. Separating and quantifying positive (Fig. 8f) and

negative (Fig. 8g) dipole magnitude versus nanoring diameter and applied *in situ* electric field also elucidates electric field- and size-dependence of magnetization change. MFM scans (Fig. 8k-2m) reveal differences in $\boldsymbol{\Delta M}$ with (Fig. 8k) and without (Fig. 8l) an applied electric field as seen in the subtraction (Fig. 8m) with features of magnetoelectric modulation and calculated magnitude resembling those predicted *in silico* (Fig. 8n). For the inner CFO dipole (finite element simulation), we find the 0^{th} (minimum), 10^{th}, 25^{th}, **50^{th} (mean)**, 75^{th}, 90^{th}, and 100^{th} (maximum) percentiles to be -3.58 (-3.55), -1.04 (-1.16), -0.29 (-0.40), **0.45 (-0.01)**, 1.20 (0.20), 2.10 (1.02), 5.24 (4.62) A/m, respectively; for the outer BTO dipole (FEM), -4.78 (-2.74), -1.64 (-0.78), -0.74 (-0.43), **0.45 (0.03)**, 1.20 (0.40), 1.95 (1.00), 5.39 (2.89) A/m, indicating slight differences likely due to signal drifts and noise fluctuations present in MFM recordings. We report linear magnetoelectric coefficients of 30.43, 49.79, 55.46, 47.09, and 57.70 mA/V (equivalent to 0.38, 0.63, 0.70, 0.59, 0.73×10^{-6} s/m for $\mu = \mu_0$; R^2 = 0.97, 0.96, 0.95, 0.98, 0.98) for 728, 778, 828, 878, 928 nm diameter rings which is substantially higher than computational predictions[145, 163, 164] and direct measurements[165–167], and comparable to the highest values reported in the literature for similar composites[168, 169].

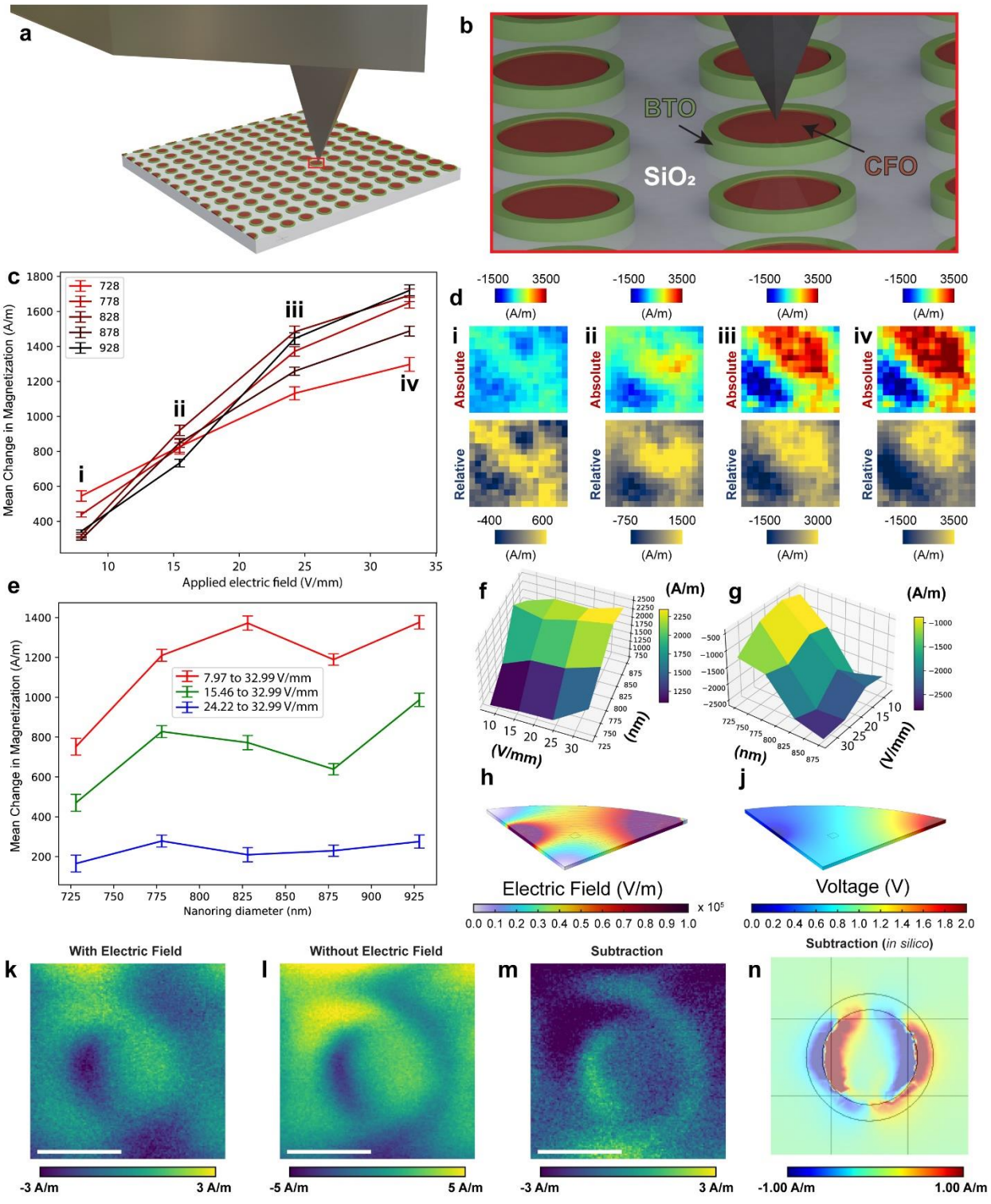
a
b
BTO
SiO₂
CFO
c
Mean Change in Magnetization (A/m)
Applied electric field (V/mm)
728
778
828
878
928
i
ii
iii
iv
d
(A/m)
Absolute
Relative
e
Mean Change in Magnetization (A/m)
Nanoring diameter (nm)
7.97 to 32.99 V/mm
15.46 to 32.99 V/mm
24.22 to 32.99 V/mm
f
g
(V/mm)
(nm)
h
Electric Field (V/m)
j
Voltage (V)
k
With Electric Field
l
Without Electric Field
m
Subtraction
n
Subtraction (in silico)
-3 A/m
3 A/m
-5 A/m
5 A/m
-1.00 A/m
1.00 A/m

Figure 8: Radius- and Electric Field-Dependent Magnetoelectric Modulation from Single Nanofabricated CFO-BTO Rings.

(a) Three-dimensional depiction of scanning probe microscopy setup with (b) exploded view of single-ring perspective outlined in red. Labels and arrows denote computer-rendered structures for BTO (pale green), CFO (light brown), and silicon oxide (SiO_2) wafer substrate (gray). (c) Electric fields of 7.97 V/mm, 15.46 V/mm, 24.22 V/mm, and 32.99 V/mm were applied to samples of geometrically varied nanorings. By subtracting images with and without varying in situ electric field, we found a positive trend with increasing electric fields and higher sensitivity for larger sizes (see legend) in agreement with *in silico* predictions. These correspond to panels d(i)-(iv) which illustrate increasing magnetoelectric modulation with increasing electric field strength quantified as both absolute and relative maps (top and bottom panels, respectively). Individual pixels are 39.0625 nm in width and height. Panel (e) delineates trends in magnetization change with respect to nanoring size between designated electric field ranges. Quantifying positive (f) and negative (g) dipole magnitude versus nanoring diameter and applied in situ electric field also elucidates electric field- and size-dependence of magnetization change. MFM scans (k-m; scale bar = 1 μm) reveal differences in amplitude modulation with (k) and without (l) an applied electric field as seen in the difference (m) with features of magnetoelectric modulation and calculated magnitude resembling *in silico* MFM of BTO/CFO nanorings (n; outer diameter = 800 nm). All error bars represent standard error of the mean of each corresponding region of interest.

Advanced designs and sensitivity predictions for multilayer CFO-BTO nanoscale geometries

To guide future nanofabrication efforts of magnetoelectric geometries and relying on our experimental validations, we turned to quantifying the response of advanced designs with increased layer count that are relatively easy to manufacture. Displayed in the top gallery of Fig. 9 are three-dimensional cross sections of magnetoelectric nanoring (Fig. 9a and b), nanocake (Fig. 9c and d), and nanostack (Fig. 9e and f) geometries. Three-dimensional electric field (Fig. 9a,c,e) and magnetic flux density (Fig. 9b,d,f) plots for 2 (i), 8 (ii), 14 (iii) and 20 (iv) paired layers highlight intricately evolving electromagnetic field patterns with varying layer count. Presented in Fig. 9g is the mean magnetization z-component change (solid line) and standard error of the mean (error bars) for rings, cakes, and stacks with 1 to 7 pairs of CFO/BTO layers (starting with CFO at the center for rings and cakes, or bottom for stacks) for an electric field varying between 0 mV/mm and 50 mV/mm. The peaks for each geometric family are as follows: 2 layers (133.33 nm layer thickness, 266.67 nm total thickness; 14.90 ± 4.64 mA/m) for nanorings, 4 layers (80 nm layer thickness, 56.67 nm total vertical height; 29.4 ± 3.55 mA/m) for nanocakes, and 4 layers (100 nm layer thickness; 4.11 ± 1.07 mA/m) for nanostacks. We hypothesize that structural impedance between layers results in relatively lower modulation with increasing layer count although increased interfacial surface area appears to counteract this effect towards the highest layer counts analyzed. In addition to layer count, geometric trends are further expounded in Fig. 9h(i)-(iii) and indicate dependence on (i) total versus layer thickness for rings, (ii) total height vs. layer thickness for cakes, and (iii) layer height vs. number of layers for stacks. For rings (Fig. 9h(i)), the data suggest that total thickness exerts greater influence than layer thickness on modulation, concomitant with our previous modeling where total particle radius was fixed and shell thickness (interfacial surface area) was decreased (increased). For cakes (Fig. 9h(ii)), this effect appears to

be dampened with ΔM recovering towards higher values with increasing layer count and higher ΔM overall likely due to vertical stacking allowing for greater freedom of movement. For stacks (Fig. 9h(iii)), we similarly find a tradeoff between layer continuity and layer count affecting ΔM with greater instability possibly due to the lack of radial symmetry that is present in rings and cakes. This analysis suggests that relatively minute changes in dimensions and configuration can significantly perturb sensitivity for designs tested, serving as a benchmark for testing additional design families.

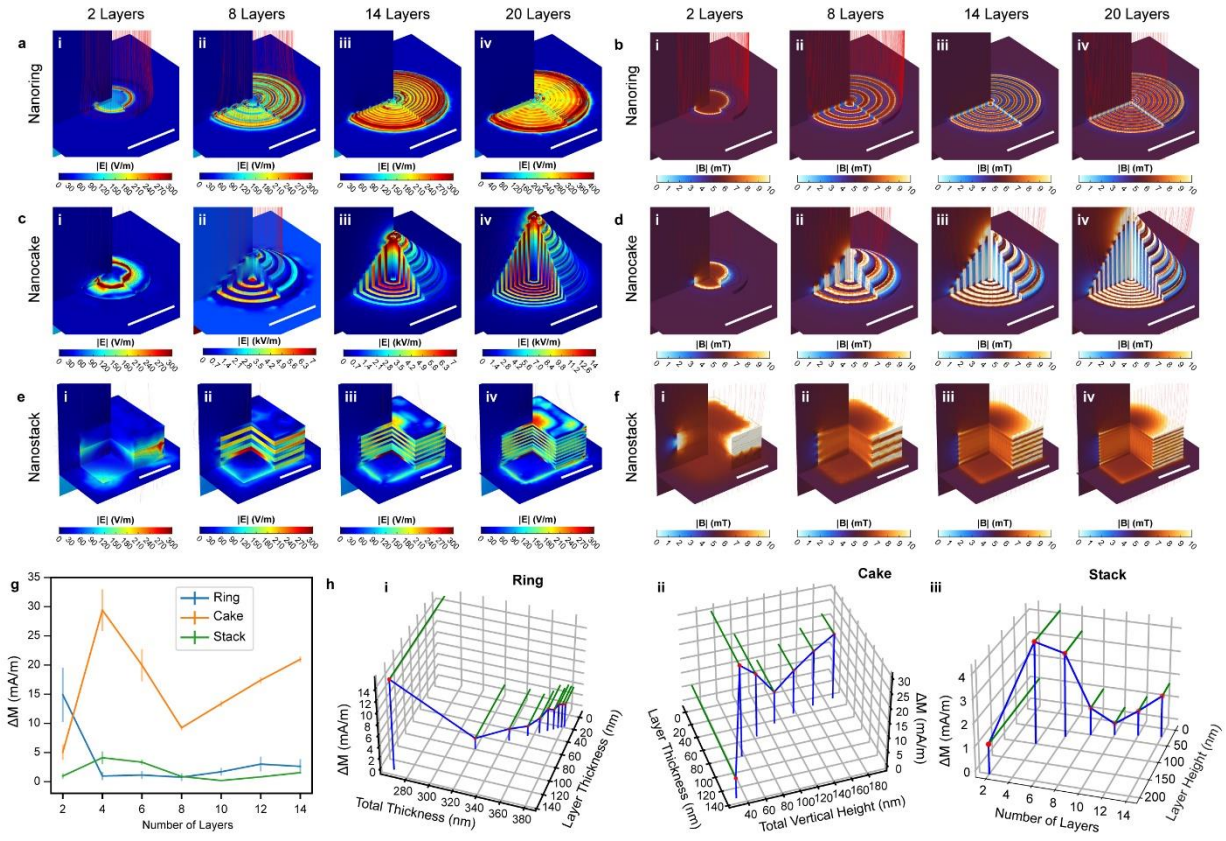

Figure 9: Finite element analysis of complex hypothetical multilayered BTO-CFO geometries.

Displayed in the top gallery are three-dimensional profiles of electromagnetic simulations involving nanoring (a,b), nanocake (c,d), and nanostack (e,f) geometries also arranged by field type (electric field (a,c,e) and magnetic flux density (b,d,f)) and subdivided by layer count (2 (i), 8 (ii), 14 (iii) and 20 (iv) layers). Presented in (g) is the mean magnetization z-component change (solid line) and standard error of the mean (error bars) for rings, cakes, and stacks with 2 to 14 paired CFO/BTO layers (starting with CFO at the center (rings and cakes) or bottom (stacks)) for an electric field change from 0 mV/mm to 50 mV/mm. Geometric trends are further expounded in sub-panels (i)-(iii) and indicate dependence on (i) total vs. layer thickness for rings, (ii) total vertical height vs. layer thickness for cakes, and (iii) layer height vs. number of layers for stacks.

Discussion and Conclusion

In this study we introduce unprecedented sensitivity measurements for nanofabricated magnetoelectric structures at nano-scale spatial resolution by MFM. The measurements were acquired in conjunction with the application of electric fields that are significantly smaller than those examined previously, towards applications in environmental and biological sensing. Our scans were performed with frequencies <1 Hz per line circumventing any high frequency noise that could result in artifacts unrelated to the magnetoelectric effect. Nonetheless, possible applications of novel magnetoelectric composites may involve more rapid events and would therefore benefit from faster single-point scans on tailored MFM/SPM and other modalities reaching tens of kHz[170]. This range of temporal resolution combined with the nanoscale spatial resolution presented here will open the gates for more advanced characterizations for fast wireless data manipulation[171, 172] or sensing, stimulation and electric field characterization in biological media[145, 163, 173–176]. A particularly exciting application is related to sensing of physiological electric fields[145]. We have recently established sensitivity levels for non-toxic concentration of ME nanoparticles (117.5 μM) in biological settings, allowing for ME particle imaging (MEPI) of brain activity. Here, we find a sensitivity level of 57.70 mA/V for the largest (928 nm diameter) rings compared to 0.497 mA/V (14 nm / 1 nm) for chemically synthesized core/shell nanoparticles reported. This constitutes a 116.10-fold advantage corresponding to a concentration of 1.012 μM of nanorings in tissue. This represents a potential breakthrough for sensing of biogenic electromagnetic fields using dilute concentrations of ME nanostructures. Moreover, we note an electric field detectability threshold of 450.293 mV/mm using MFM, which can be further improved by adjusting scan parameters and averaging rapid single-point scans down to several mV/mm as is present within the cortex[177]. Additionally, the designs presented here can be

patterned as scalable multiplexed on-chip arrays with precise clustering geometry[178] and serve as versatile high density modules for sensing and stimulation. Another important outcome of this study is the observation of clear positive correlation between sensitivity and nanoring diameter and thickness. While there exists a spectrum of sizes, geometries, and core/shell ratios in recent work[65–69, 174, 179–181] , large-scale fabrication of ME nanostructures using exact dimensions has not been achieved until now. The exceptional consistency of our nanofabrication scheme lends itself to improved evaluation of electric field sensitivity that can inform more precise designs. Our analysis greatly improves the quantification of ME response and its dependent on electric field strength compared with more crude measurements reported in the literature[80–90]. Finally, we presented modeling results of geometries which exhibit changes in $\boldsymbol{\Delta M}$ that vary substantially with layer count, in contrast to our simulation sweeps of bilayer rings which shows gradual changes with respect to varying proportions. To better characterize dependence of $\boldsymbol{\Delta M}$ on nanoscale proportions, further evaluations of geometry should incorporate finite element modeling and nanofabrication of advanced classes such as polygonal and jagged rings which may yield improvements in sensitivity without increasing fabrication process complexity. In conclusion, our results herald prospects for elevating performance to the order of single mV/mm detection regime and can help to empower new ME nanostructure designs and compositions capable of revolutionizing the *status quo* of novel magnetoelectricity-based technologies.

.

Methods

Fabrication of CFO-BTO Nanorings

To fabricate rings on silicon substrate, we used a protocol modified from Pan et al.[162] First, a 76.2mm N-type P-doped <100> 1-10 Ω · cm 380um single-sided polish (SSP) silicon wafer (UniversityWafer, Catalog number 1455) with 300 nm wet thermal oxide was spin coated at 4000 rpm for 45 seconds with MMA(8.5)MAA EL 11% (Cat # M310011-0500L1GL, Kayaku) diluted to 6% in anisole (Cat # M030100-1000L1GL, Kayaku)). The wafer was baked at 150 °C for 90 sec, then PMMA 495 A4 (Cat # M130004-0500L1GL, Kayaku) was spin coated at 4000 rpm for 45 seconds. The wafer was again baked at 150 °C for 90 sec. The wafer was diced into 20 mm × 20 mm pieces and patterned using electron beam lithography (Elionix ELS G-100, Elionix Inc., Tokyo, Japan) using the parameters in Table 1. Samples were developed at -11.5 °C in 1:3 methyl isobutyl ketone (Thermo Fisher Scientific Inc., Waltham, MA, USA, Cat. Number M2131):isopropanol (MIBK:IPA) for 75 sec and rinsed first with IPA, then with deionized (DI) water.

CFO sol gel was produced by dissolving cobalt acetate tetrahydrate $Co(CH_3COO)_2 \cdot 4\ H2O$ (Cat # AC293062500, Acros Organics) and iron nitrate nonahydrate (Cat # 470301-400’ Ward's Science) in methoxyethanol (Cat # AA31733AK, Thermo Fisher) with 10% v/v ethanolamine (Cat # AC149582500, Acros Organics). BTO sol gel was made with 35 mL ethylene glycol (Cat # E8270-500ML, Aqua Solutions) and 3.2 mL diethanolamine (Cat # I000825G, TCI America) which was melted beforehand in a warm water bath at 96 ºC. 0.51 g Barium Acetate (Cat # 22879-100G, Chem-Impex International) was added to the solvents at 60 ºC. 0.9725 g (962.5 uL) of Titanium Diisopropoxide bis(acetylacetonate) (75% wt solution in propanol) (Cat # B3395-25G, TCI

America) was added dropwise and the mixture was stirred at 70 ºC until clean and transparent (for appx. 3 hours). This mixture was diluted 1:1 with methoxyethanol immediately before usage. Wafer samples were spin coated with BTO sol gel, baked on a hotplate at 150 ºC for 5 mins, then spin coated with CFO sol gel and again baked on a hotplate at 150 ºC for 5 min. Spin coating consisted of the following steps, with the objective to safely spin coat for around 40 seconds at 6000 rpm. 5 sec ramp up, 500 rpm for 10 sec; 6 sec ramp up, 4000 rpm for 1 sec; 20 sec ramp up, 6000 rpm for 40 sec; 15 sec ramp down. After inverting and soaking in acetone for 20 to 40 minutes, samples were rinsed in isopropanol, then DI water, and immediately dried with nitrogen gas.

Table 2: Parameters for patterning magnetoelectric nanorings using electron beam lithography

Field size (um)	Dot number	Dose (uC/cm^2)	Feed pitch	Scan pitch	Beam current (nA)	Dose time (us/dot)
250	500,000	800,1600,2400	10	10	10	0.06, 0.08, 0.10, 0.12

Sample preparation and magnetic force microscopy scans

To apply controlled electric fields to nanoring samples, silver polish (PELCO® Conductive Silver Paint, Ted Pella, Inc., Prod No: 16062-15, Redding, CA, United States of America) was applied to opposite edges of the sample, 32 AWG magnet wire (Newark, Chicago, United States of

America) was soldered onto the applied polish, alligator clips were connected to the magnet wire, and wired to a DC variable voltage supply (E3630A Triple Output DC Power Supply, Hewlett Packard, Palo Alto, CA, United States of America).

We used Python 3.8 with the PySPM library to analyze our AFM scans and radially unwrapped images via linear polar mapping to determine homogeneity. MFM phase images were used to discern trends from our data. For electric-field- and size-dependent modulation, we subtracted scans with and without applied electric fields of 7.97 V/mm, 15.46 V/mm, 24.22 V/mm, and 32.99 V/mm, partitioned the image into sections representing each ring size (n=4 each) and extracted and plotted the mean and the SEM of the mean. Dipolar quantification of magnetization was performed on subtracted images by taking the mean of the positive and negative regions between 6 and 25 pixels (each pixel being 39.0625 nm) from the center of each nanoring.

Finite element modeling of three-dimensional nanostructures

COMSOL Multiphysics 6.0 (COMSOL Inc. Stockholm, Sweden) was used to simulate CFO-BTO geometries and for dipole modeling. Details of model parameters can be found in our previous work[145]. We used a Si substrate with its based clamped using a Fixed Constraint boundary condition to support the geometry, submerged it in cerebrospinal fluid, surrounded the whole simulation volume with an infinite element domain, applied a 4 kA/m magnetic field to the outside of the simulation arena, and electric field of 50 mV/mm between the top and bottom faces of the arena in the -*z* direction. For the dipole, we added remanent magnetization of 63.66 kA/m in the ***y*** direction to the CFO core and modeled the geometry in air as opposed to cerebrospinal fluid. Data were exported to Python 3.8 for further analysis. $\boldsymbol{\Delta M}$ was computed as the average across the nanostructure interior.

Author Contributions

AH and IB designed the research. IB performed nanofabrication and MFM measurements. IB performed finite element analysis with TZ and AV. AH and IB wrote the manuscript with TZ and AV.

Acknowledgements

The authors gratefully acknowledge the use of facilities and instrumentation supported by NSF through the University of Wisconsin Materials Research Science and Engineering Center (DMR-1720415). This work was supported by the National Institute of Neurological Disorders and Stroke and the Office of the Director's Common Fund at the National Institutes of Health (Grant DP2NS122605 to AH) and the National Institute of Biomedical Imaging and Bioengineering (Grant K01EB027184 to AH). This material is also based on research supported by the US Office of Naval Research under award numbers N00014-23–1-2006 and N00014-22–1-2371 to A.H. through Dr. Timothy Bentley and the Wisconsin Alumni Research Foundation (WARF).

Chapter 3: Wireless magnetoelectric particle recording of neural activity

***I. Bok**, T. Larson, M. Nornberg, I. Haber, T. Kearse, X. Wang, A. Hai

Abstract

Wireless imaging of neural electric and magnetic fields with high spatiotemporal resolution and sensitivity, low invasiveness, and minimal signal attenuation in the body with a large potential field of view is an unmet need in neuroscience, biomedical engineering, and general clinical practice. Magnetic particle imaging (MPI) is a novel, preclinical imaging methodology which has been able to detect injected iron oxide nanoparticle tracers [3, 42, 182] thereby allowing for structural and perfusion readouts *in vivo*. Magnetoelectric nanoparticles (MENPs) and nanostructures have concurrently been developed and possess untapped potential for detecting biologically relevant electric fields on the order of mV/mm. Combining the electric-to-magnetic field transduction of MENPs with MPI to wirelessly transduce neural electric fields to MPI-detectable magnetization readouts forms the basis for wireless magnetoelectric particle imaging (MEPI) of neurobiological events and neuropathological states which fulfills all unmet criteria mentioned prior. In this chapter, I assess the biocompatibility of cobalt ferrite (CFO) nanoparticles and nanofabricated arrays of magnetoelectric CFO core, barium titanate (BTO) shell nanostructures and perform MEPI point recordings of neural networks reading out local field potentials and single unit activity both not present in sham. Our data form the basis for deploying more advanced, semi-automatic and fully automatic MEPI configurations for whole-brain imaging with high spatiotemporal resolution and sensitivity.

Introduction

A novel form of wireless electrophysiology with high spatiotemporal resolution and sensitivity, low invasiveness, and minimal signal attenuation by biological substrates is an unmet need and potentially revolutionary addition to the repertoire of recording techniques used within clinical neuroimaging. However, recent attempts at fully functional readouts encompassing novel fMRI acquisition[183, 184] and processing methodologies[185], optogenetic implants[186], and modular brain-machine interfaces (BMIs)[5, 187–189] suffer from a tradeoff between one or more of spatial and temporal resolution, sensitivity, invasiveness, and accessibility. BMIs in particular are a product of multiple decades of innovation and iterative improvement beginning with the Michigan probe[190, 191] and Utah array[4, 192] and progressing through increasingly complicated designs, which have assisted paralyzed patients in regaining mobility, communicating, receiving sensory input, and producing sensory output. However, these remain dependent on primitive neurological interface technologies, especially different variants of invasive electrophysiology, thereby inheriting all associated limitations[5, 187–189].

Magnetic particle imaging (MPI) provides a robust foundation for wireless, non-invasive neuroimaging, but has remained predominantly structural since its inception[7, 37]. Augmentations have focused on streamlining acquisition[193], optimizing resolution[194, 195], and maximizing sensitivity[41]. Multiple readouts in parallel have been demonstrated[196] as a method for improving as well as parallel MPI/MRI[197] and MPI/CT[198]. Perfusion-based functional magnetic particle imaging of the brain has been demonstrated for detection of neuropathology *in vivo*[3, 42, 182] and shows promise for application to humans[43, 44, 199]. While most of these studies utilize passive superparamagnetic iron oxide nanoparticles (SPIONs)

to acquire concentration-dependent readouts of diffused particles, new active magnetic particle designs that offer signal modulation specific to biochemical and physiological processes can create a new repertoire of readouts for MPI. In particular, magnetoelectric nanoparticles (MENPs) have been found to be highly biocompatible in vitro[200] and in vivo[8, 200–202] and have been repeatedly used for stimulation of the brain to treat neuropathological symptoms in vivo[16, 201–203]. The superior biocompatibility of barium titanate (BTO) makes it an excellent candidate for the piezoelectric portion of nanoparticles and structures[204–206]. Previous work has established sensitivity levels for non-toxic concentration of ME nanoparticles (117.5 μM) in biological settings, allowing for ME particle imaging (MEPI) of brain activity. The ability of MENPs used in parallel with MPI or magnetoelectric particle imaging (MEPI) is theorized to allow for detection of neural activity[207], and additional experiments within this thesis have further demonstrated magnetoelectric modulation optimization of nanoscale rings but this methodology has not yet been demonstrated.

In this chapter, I present a method for recording the intrinsic electric fields from neural networks using specialized magnetoelectric nanoparticles with intimate electrical junctions between nanostructures and neuron allowing for maximal transduction as previously predicted[208] and analyze both low frequency, network-level local field potentials and high frequency, single-unit action potentials from neurons *in vitro*. Additionally, we assess the biocompatibility of cobalt ferrite (CFO) nanoparticles and nanofabricated arrays of magnetoelectric CFO core, barium titanate (BTO) shell nanostructures and perform MEPI recordings of neural networks reading out local field potentials and single unit activity absent in sham recordings. Our data form the basis for deploying more advanced MEPI configurations for whole-brain imaging with high spatiotemporal resolution and sensitivity.

Results

Biocompatibility Assessments

Before introducing the nanofabricated rings to *in vitro* neural networks for MEA and MEPI recordings, we first assessed biocompatibility of our devices to neural networks (Fig. 10) both functionally in the shorter term by injecting CFO (Fig. 10(a-d)) and structurally on DIV 16 (Fig. 10(e-f)). Within the recording we find synchronous neuronal firing with 31 network spikes pre-CFO vs. 32 network spikes post-CFO (see top row of Fig.10a). These data are supported by raw fluorescence traces with similar activity before and after CFO injection (red line). $[Ca]^{2+}$ images of a single neuronal aggregate are shown in Fig. 1b before network spike (Fig. 10b(i)) and at network spike peak (Fig. 10b(ii)) with red arrows indicating areas of low fluorescence due to presence of CFO nanoparticles. Displayed in Fig. 10c is a heatmap of differing CFO nanoparticle densities per voxel determined automatic image segmentation analysis. A histogram Fig. 1d of firing rates before (orange) and after (blue) injection of CFO shows that neuronal activity is unchanged ($p = 0.0579$, n.s). Fig. 1e is a cluster of neurons with red arrow indicating gap junction formed by a neuron which voluntarily engulfed a single CFO-BTO nanoring and formed a gap junction (Fig. 10f) with that ring. The data from these evaluations affirms the biocompatibility of our nanostructures.

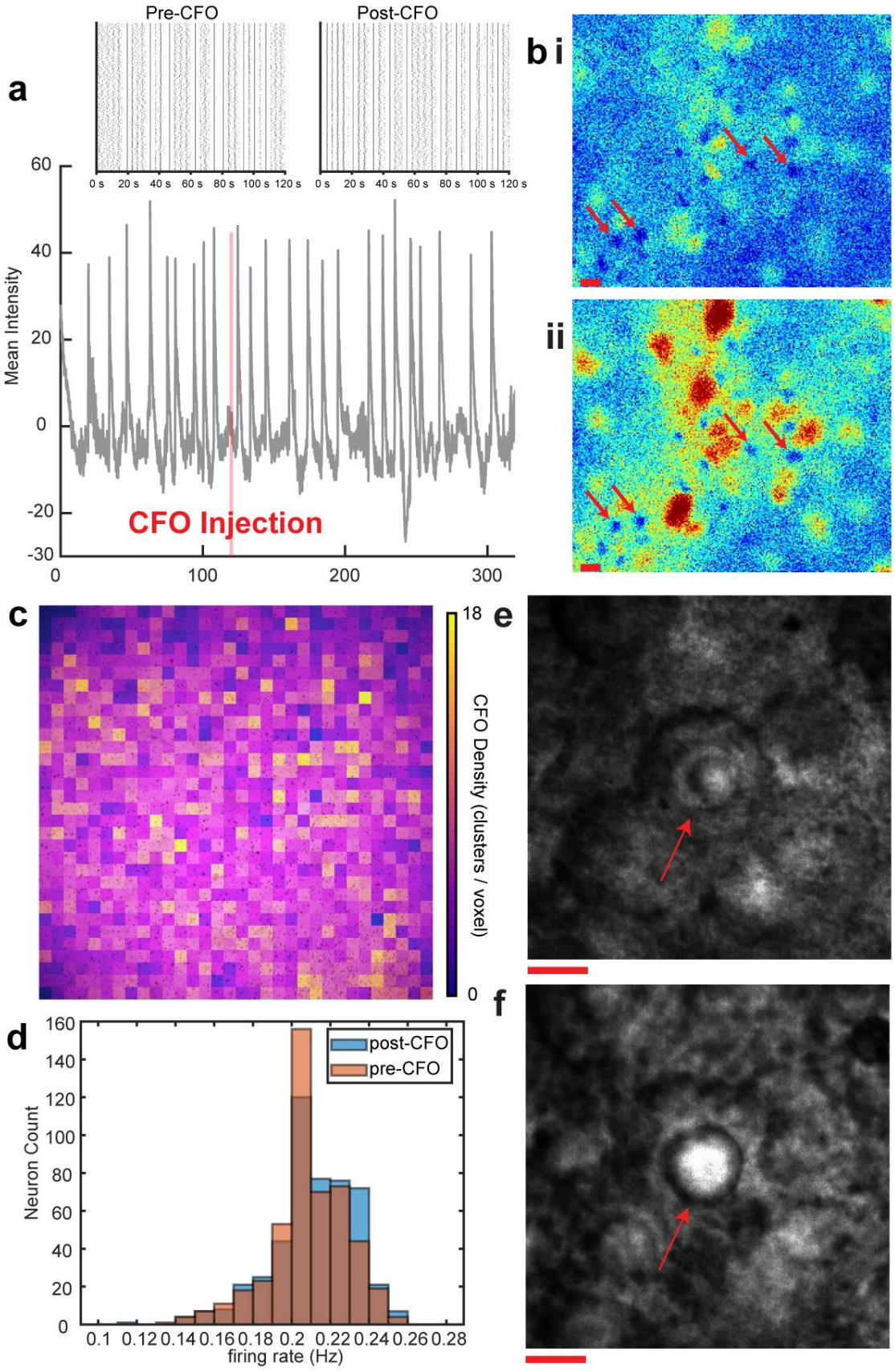
a
Pre-CFO
Post-CFO
0 s 20 s 40 s 60 s 80 s 100 s 120 s
Mean Intensity
CFO Injection
b i
ii
c
18
0
CFO Density (clusters / voxel)
d
post-CFO
pre-CFO
Neuron Count
firing rate (Hz)
e
f

Figure 10: Neural network biocompatibility around CFO nanoparticles and magnetoelectric CFO-BTO rings in vitro.

We find synchronous neuronal firing with 31 network spikes pre-CFO vs. 32 network spikes post-CFO (see top row of panel a). These data are supported by raw fluorescence traces with similar activity before and after CFO injection. $[Ca]^{2+}$ images of a single neuronal aggregate are shown in (b) before network spike (i, frame 5235/6062) and at network spike peak (ii, frame 5238/6062) (frame rate 10 Hz), with red arrows indicating areas of low fluorescence due to presence of CFO nanoparticles. Displayed in (c) is a heatmap of differing CFO nanoparticle densities per voxel determined via image segmentation analysis using Python. A histogram (d) of firing rates before (orange) and after (blue) shows that neuronal activity is unchanged ($p = 0.0579$) due to CFO nanoparticle injection. Panel (e) is a neuron that voluntarily engulfed a single CFO-BTO nanoring and formed (f) a gap junction with that ring (junction indicated by red arrow), both on DIV 16.

Magnetoelectric Particle Imaging (MEPI)

To undertake MEPI scans, we applied a custom-built magnetic particle imaging scanner with components arranged as shown in Fig. 11. A microelectrode array electrophysiology setup and magnetic particle imaging scanner were combined into a single system (Fig. 11a) with integral MPI components placed as indicated (side view displayed in Fig. 11b). Using this configuration and placing magnetoelectric ring onto neural networks, we acquired multiple datasets and converted raw traces to Spectrograms. Short time Fourier transform frequency bins near the 3rd harmonic (75.75 kHz given 25.25 kHz fundamental) for a range of experimental conditions indicate that nanorings are amplifying intrinsic fields from neural networks allowing for wireless electrophysiology of neuronal activity (Fig. 12). Magnetic particle imaging scans of neurons grown on microelectrode arrays interfaced with magnetoelectric ring samples (Fig. 12a) indicate increased energy compared to: (b) the same as (Fig 12a) except without rings (MEA with only neural networks), (c) the same as (Fig 12a) without neurons (MEA filled with cell culture media and only rings), and (d) absence of rings and neurons (empty MEA filled with cell culture media). To ascertain the detectability of single-unit activity throughout scans, we recorded multiple datasets and performed event classification, extracting inter-event interval histograms for microelectrode array (MEA) and magnetoelectric particle imaging (MEPI) data (Fig. 13). Data streamed from a single microelectrode thresholded using running time-averaged standard deviation ($\sigma = 6.5$, $\tau = 5$ s) is plotted in Fig. 13a. The resulting spikes are presented in Fig. 13b and the shaded gray region from panel (a) is enlarged in Fig. 13c with the inset showing inter-spike interval (ISI). Data recorded by magnetoelectric particle imaging also thresholded using running time-averaged standard deviation (different parameters $\sigma = 6$, $\tau = 2$ s) is plotted in Fig. 13d with resulting spikes presented in Fig. 13e and shaded gray region

enlarged in Fig. 13f, ISI again shown as an inset. These results solidly indicate modulation of the third harmonic within MPI via neural activity geometrically optimal nanorings.

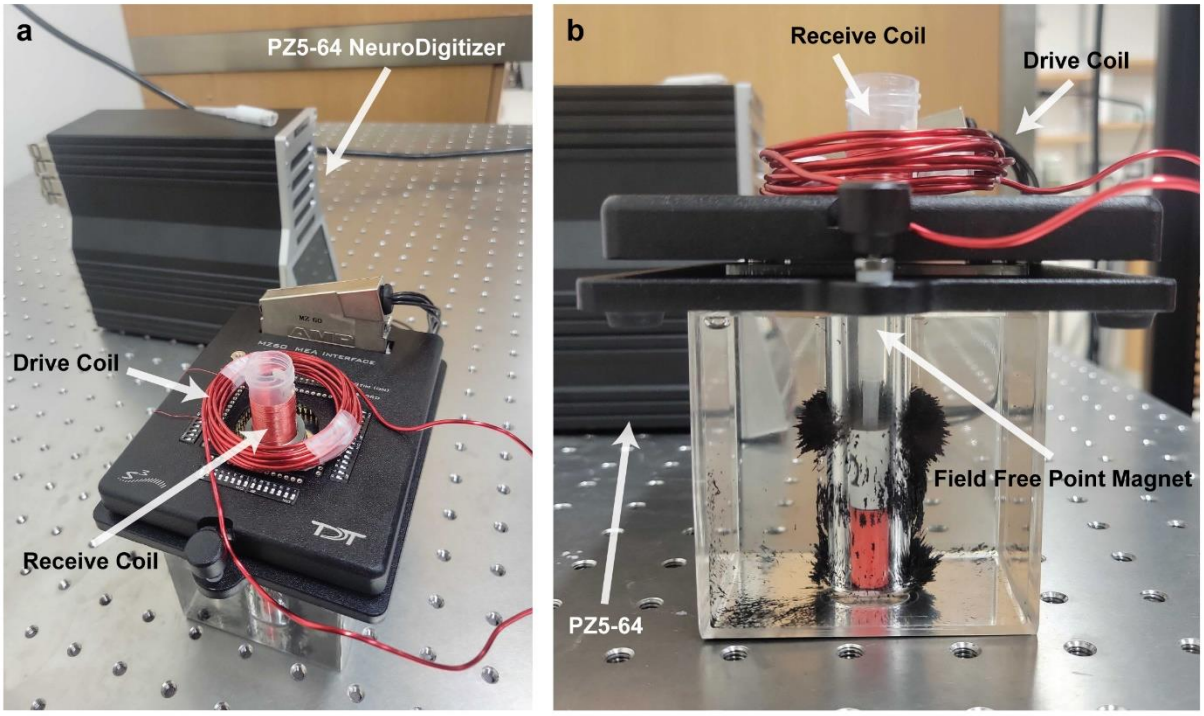

Figure 11: Dual microelectrode array and magnetoelectric particle electrophysiology and imaging scanner schematic.

MEPI scans were acquired using a custom-built system (a) consisting of drive and receive coils and field-free point magnets mounted on a commercial MZ60 microelectrode array headstage from Tucker-Davis Technologies. A side view of the arrangement (b) shows the alignment of the FFP below the receive coil and placement of the receive (i.e. cancellation) coil with respect to the drive coil for harmonic minimization.

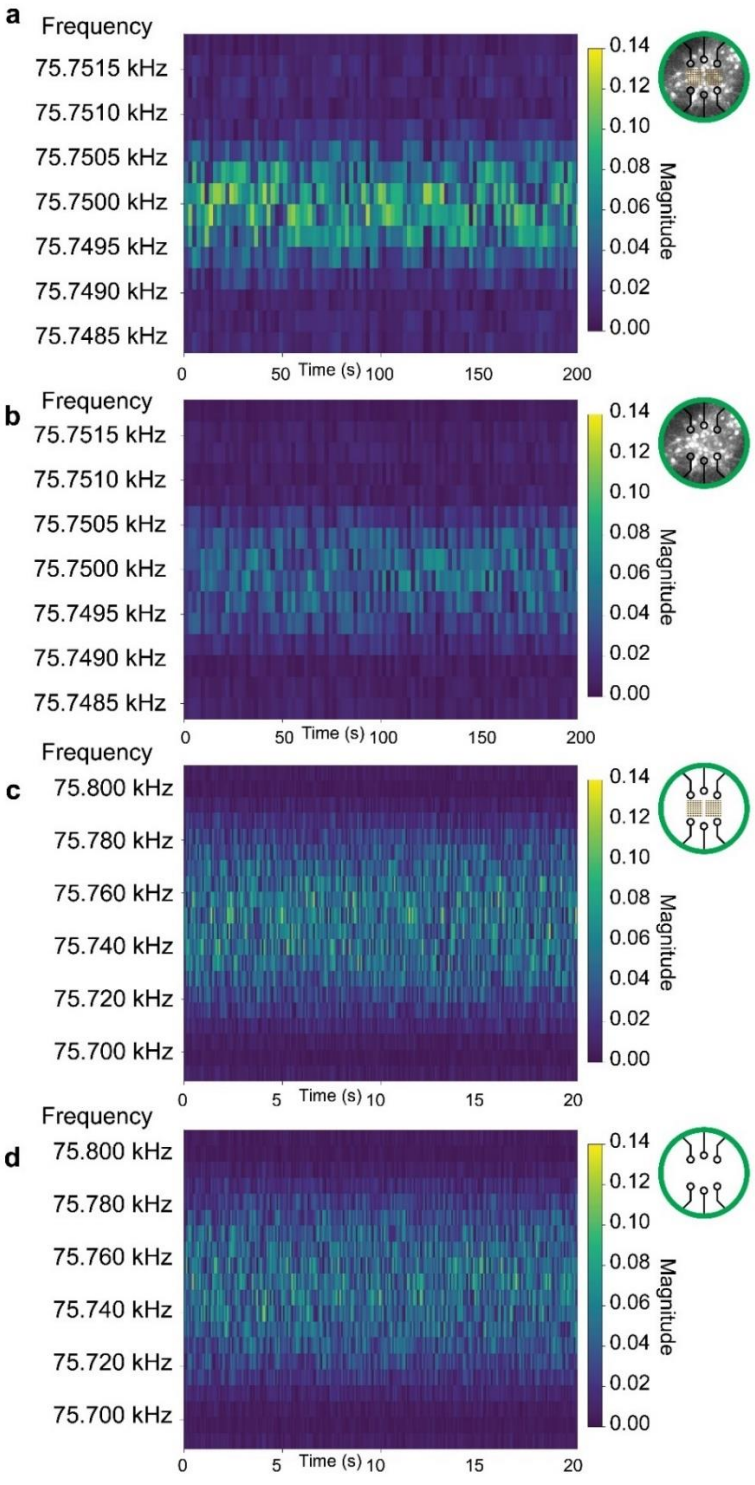

Figure 12: 3rd Harmonic Spectrograms of Magnetoelectric Particle Imaging of Neuronal Networks. Spectrograms near the 3rd harmonic (75.75 kHz given 25.25 kHz fundamental) for a range of experimental conditions allow for wireless electrophysiology of neuronal activity. (a) Magnetic particle imaging scans of neurons grown on microelectrode arrays interfaced with magnetoelectric ring samples, (b) the same as (a) except without rings, (c) the same as (a) without neurons, and (d) absence of rings and neurons by transduction of intrinsic neuronal fields

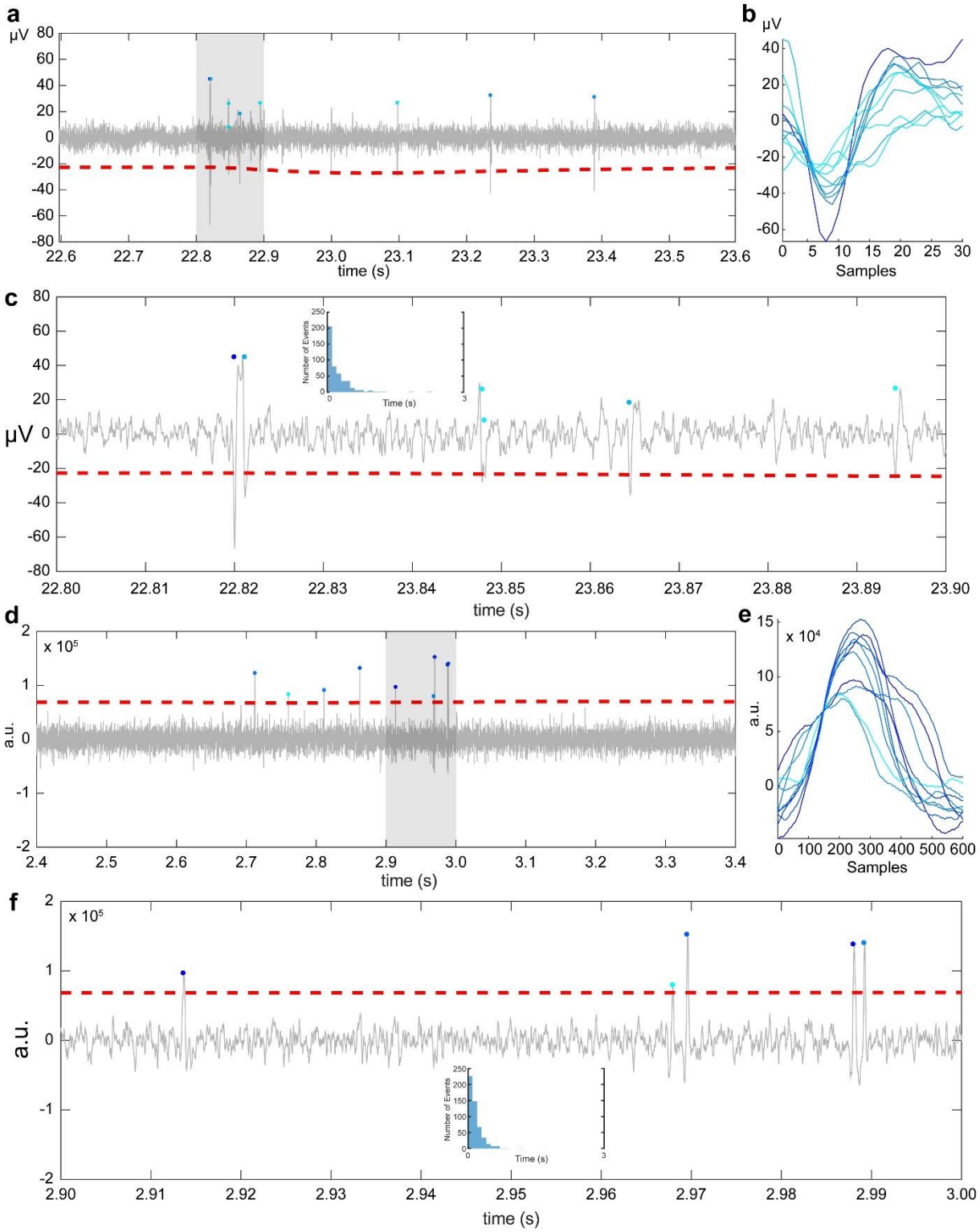
a
μV
time (s)
b
μV
Samples
c
μV
Number of Events
Time (s)
time (s)
d
x 10^5
a.u.
time (s)
e
x 10^4
a.u.
Samples
f
x 10^5
a.u.
Number of Events
Time (s)
time (s)

Figure 13: Event classification and inter-event interval for microelectrode array (MEA) and magnetoelectric particle imaging (MEPI) data.

(a) Data streamed from a microelectrode thresholded using running time-averaged standard deviation ($\sigma = 6.5$, $\tau = 5$ s) with resulting spikes presented in (b) and shaded gray region enlarged in (c) and inset showing inter-spike interval (ISI). **(**d) Data recorded by magnetoelectric particle imaging system thresholded using running time-averaged standard deviation ($\sigma = 6$, $\tau = 2$ s) with resulting spikes presented in (e) and shaded gray region enlarged in (f), ISI shown as inset.

Methods

Cell culture

Primary cortical rat neurons were prepared as described previously [275] and cultured using the following protocol: briefly, glass coverslips were sterilized with ethanol for 15 minutes, with MEA sterilization performed under UV light. Culture surfaces were prepared with a 50 µL (coverslip) or 100 µL (magnetoelectric wafer sample) droplet of sterile filtered aqueous 0.1 mg/mL poly-d-lysine (PDL, Gibco A38904-01) and 4 µg/mL laminin (Gibco 23017-015). Cells were seeded in plating media at a density of 4×10^6 cells/mL (Neurobasal Plus, Gibco A3582901; 10% FBS Gibco 10437010; 1x GlutaMAX, Gibco 35050-061), cultures were incubated for 4 hours, and media was changed to 3 mL of maintenance media (Neurobasal Plus, 1x B27 Plus Gibco A3582801, 1x GlutaMAX). Media changes were performed every 3-4 days (Mondays and Fridays), at half (1.5 mL) and all (3 mL) of the volume for the first and subsequent weeks, respectively. Between cultures, device culture surfaces were cleaned with Tergazyme enzymatic detergent (Alconox, White Plains, NY) per the manufacturer's instructions.

Calcium Imaging

Fluo-4 AM calcium sensitive dye (Invitrogen, F14201) was dissolved in 1% Pluronic F-127 surfactant (Invitrogen, P3000MP) in dimethyl sulfoxide (DMSO) at a concentration of 1 mg/mL Stock solution was added to maintenance media at a final concentration of 10 µg/mL in loading solution. Cultures were stained with 2 mL of loading solution for 20 minutes at room temperature, loading solution was replaced with maintenance media, and cultures were left in the incubator for 20 minutes to hydrolyze the AM esters. Cultures were imaged within two

hours after hydrolysis was complete at a frame rate of 10 Hz. CFO nanoparticles (American Elements) were diluted in cell culture maintenance solution, vortexed thoroughly, and injected via micropipette.

Magnetoelectric Particle Imaging (MEPI) and Microelectrode Array Electrophysiology

MEAs were used for recordings on DIV 13 using an MZ60 headstage interface streamed at 24,414 Hz through PZ5-64 NeuroDigitizer amplifier and RZ5P base processor (Tucker-Davis Technologies, Alachua, FL). MEPI scans were acquired using a custom-built system comprised of the following components: a Multicomp PRO MP750064 Arbitrary Waveform Generator (input waveform), AE Techron 7224 (drive field amplifier), drive coil (AWG 14 Magnet Wire, Belden Cat #8073, 28 turns), miniature neodymium field free point magnets, receive coil (3D printed, cancellation coil with AWG 32 Magnet Wire, Belden Cat# 8056), notch filter (KR Electronics 3373-23.4-SMA 23.4 kHz Notch), high-pass filter (Mini-Circuits ZFHP-0R055-S+), and preamplifier (Mini-Circuits ZFL-500+; unpowered). Recordings were either plotted as a spectrogram using the short time Fourier transform in Python 3.8 or filtered between 250 Hz and 3000 Hz and processed further in MATLAB (The MathWorks, Inc. Natick, MA, USA).

Conclusion

Computational modeling

To model nanoparticle response to electromagnetic fields, I used industry-standard finite element analysis software (COMSOL Multiphysics 6.0, COMSOL Inc. Stockholm, Sweden), enabling other research groups to expand upon my work [164, 209]. Moreover, by leveraging finite element modeling it is possible to visualize intra-nanostructural field profiles thereby facilitating understanding of nanoparticle response to biological phenomena and external magnetic fields. I was able to affirm that CFO-BTO nanoparticles have the capability to perform both structural and functional magnetic particle imaging in a paradigm termed magnetoelectric particle imaging (MEPI). I found that nearly all the magnetization from CFO-BTO nanoparticles resides in the core and that increasing core-shell ratio yields higher modulation, supporting production of nanostructures thinly encased in BTO for maximal responsivity. However, thinner layers exhibit more stochastic field responsivity across geometries *in silico* and may prove more difficult to fabricate. Because the magnitude of the modulation also is a function of the angle between extrinsic electric and magnetic fields, exposing neural parenchyma to high densities of CFO-BTO nanostructures will maximize the magnetometrically detectable signal. Because these structures are ~10 to ~1000 times smaller than neuronal somata, this is not only feasible but also probable. Furthermore, large volumes of nanoscale magnetoelectric sensors traversing through the cerebral vasculature and settling upon the brain parenchyma were found to efficiently harness neuronal electric fields and supply detectable changes in MPI magnetization signal. In addition to these analyses, the presented finite element paradigm can further be utilized to test not-yet realized nanoparticle core-shell composites such as Terfenol-D/BTO to expand the scope of

magnetoelectric device utility and direct material selection for nanostructure fabrication. This same finite element modeling was leveraged for hexagonal clusters of iron oxide nanoparticles affixed to a silicon wafer substrate and diverse distributions of magnetic fields components were found upon application of a 4.7 T magnetic field. Multiphysics finite element modeling of both iron oxide nanoparticle clusters and magnetoelectric nanostructures has therefore served well overall as a foundation upon which to build experiments using real nanoparticles and nanostructures for various forms of magnetometry.

Nanofabrication

For this dissertation, I fabricated both iron oxide control and dynamic magnetoelectric nanoparticles using multi-step nanolithography consisting of novel procedures thereby allowing for a large degree of customizability. I leveraged nanoscale imaging and analysis tools (scanning probe microscopy, scanning electron microscopy, and optical microscopy) to verify the structure of my devices and applied MRI and MPI to affirm their magnetic responsivity profile. Although electron beam nanolithography provides excellent control over nanoscale sensor size and shape, preliminary experiments with photolithography show promising results for more rapid larger-scale production of magnetoelectric sensors (Supplementary Fig. S4.1). Detachment from native substrates will require transfer printing [210] or other delicate liftoff practices such as a selective linker layer to prepare arrays of particles for injection into neuronal networks. Having identically spaced arrays confers another nanofabrication advantage for custom multi-step alignment and assembly for more complex structures such as those presented in Fig. 9.

Biocompatibility and phagocytosis of nanorings in vitro and in vivo

The exceptional biocompatibility *in vitro* of the nanoscale CFO-BTO structures fabricated agrees with previous studies on CFO-BTO nanostructures [10, 12, 16, 211, 212]. I found that neurons were undisturbed both structurally and functionally by short- and long-term exposure to CFO-BTO structures, exhibiting no defects or perturbations because of the interactions with the materials. Injection of CFO nanoparticles caused aggregation that can be mitigated via functionalization with surfactants [10, 16], which can also improve biostability. Neuronal phagocytosis and transport of single nanorings gives credence to the high biocompatibility of our in-house fabrication method as explored extensively for three-dimensional microelectrode array protrusions by Hai et. al [213–218] with neuronal engulfment of individual electrodes. Tight coupling between neurons and individual rings increases magnetoelectric transduction efficiency thereby enhancing MEPI signal and reducing scanner overhead for in vivo and clinical applications, but sensor clearance may require more involved extraction such as by using a large magnetic field gradient to pull nanostructures across the blood-brain barrier [74, 211].

Neuroimaging

Magnetic particle imaging is a rapidly evolving preclinical imaging platform [219] that has been used in the brain *in vivo* for perfusion imaging [182, 220] and stimulation [12, 16]. The sensitivity of magnetic particle imaging rivals that of archetypal tools such as fMRI and electrophysiology but it cannot yet compete with hypersensitive tools such as SQUID magnetometry or OPM with sensitivity down to femtotesla levels, although these techniques require pristine conditions (i.e. supercooling for SQUID and magnetic shielding for SQUID and OPM) for proper recording. It therefore is most sensible to persevere with magnetic particle imaging and utilize the modulation of odd harmonics to affirm the neuroelectrophysiological modulation of magnetoelectricity to strain relationship. The cumulative magnetization of large collections of magnetoelectric

nanoparticles residing in brain parenchyma adds linearly to MEPI signal [219] although the local neuronal electric field vector profile may vary resulting in sub-linear cumulative signal from each voxel. Continuing improvements in MPI acquisition speed and sensitivity will provide a means to ultra-sensitive readouts from large fields of view over long periods of time without significant unwanted heating or stimulation in human subjects [221]. Targeted delivery of sensors to specific regions of the brain will require precise magnetic field gradients which can be facilitated with high specificity using MPI gradient coils.

While here I focused on magnetic particle imaging for neuroelectrophysiological sensors, I anticipate the advent of novel modalities and the rapid evolution of established techniques such as optically detected magnetic resonance and electron paramagnetic resonance imaging which will provide additional venues for recording using the described devices. Parallel MRI and MPI of magnetoelectric sensors is clearly unfeasible due to the large field gradients interference, but serial MRI and MPI [197] has been performed in vivo as well as parallel CT and MPI [198]. A more feasible bimodal imaging paradigm is traditional electrophysiology with MEPI for which we have performed pilot tests using microelectrode arrays and found minimal interference between the two when configured properly. Due to the delicate nature of biogenic electric fields and the inherent stimulation of the field free point from MPI, I also note that significant flux amplification is required for detectability of the MEPI signal even from large swaths of neuronal populations firing in synchrony. It may therefore be necessary to combine modulation from higher harmonics [222] or acquire lower resolution data with higher averages to discern signals from samples *in vitro* and *in vivo*. MPI is approaching clinical use with the primary barriers being the size of the scanner relative to its speed, sensitivity, and resolution also taking into account safety limits of specific absorption rate and nerve stimulation [223].

Clinical significance

Within this thesis I brought forward a new and powerful form of electrophysiology which has the capacity to serve as a novel platform for detecting neurogenic electric fields throughout the brain parenchyma using established magnetic particle imaging infrastructure. CFO-BTO nanoparticles can readily be injected into human subjects for clinical trials providing a streamlined pathway towards a new method of clinical neuroelectrophysiology. The biocompatibility assessments performed herein agree with the literature [8, 56, 146] and support further miniaturization and densification of sensors in preparation for implantation/injection into the brain with rapid clearance as observed *in vivo* [212]. The robustness and homogeneity of these sensors will allow for efficient detachment from substrates and suspension into injectable solution forming the basis for a safe and easily manufacturable and mass-producible system for detecting and managing neuropathology in clinical settings.

MEPI forms the basis for achieving a whole brain readout directly related to electrophysiology, while blood oxygenation level-dependent functional magnetic resonance imaging (BOLD-fMRI) is more closely related to hemodynamics, however both forms of neuroimaging are volumetric platforms. [224–226]. BOLD-fMRI remains a standard tool for many researchers and clinicians but is not without serious controversy [21, 22, 227–231]. Molecular fMRI forms the basis for detecting biochemical events using injectable agents and has been utilized for measurement of neurotransmitters and ionic fluctuations *in vivo* (see Section Introduction: Rational design of injectable molecular neural probes). However, MEPI operates on expedited timescales due to rapid [232] and precise [91] transduction via the magnetoelectric effect and high sensitivity of MPI [41, 207]. This rationale and theoretical basis for the high spatiotemporal resolution as well as exceptional sensitivity tunable via geometric optimization provides a robust stage for the ultimate

adoption of MEPI as an essential neurotechnology for understanding the brain and its various pathologies. The minimal risk associated with these sensors and their low overhead provide impetus not only for rapid, broad adoption but also for rapid evaluation and approval by the FDA. Conventional neuroimaging or neuromodulation techniques currently endure low spatial and/or temporal resolution and are often highly invasive. For example, clinically approved deep brain stimulation techniques involve performing a highly invasive craniotomy and implanting electrodes into regions of the brain associated with malfunctioning Parkinsonian circuitry. These implants also require the use of a battery which must be either recharged or replaced on a regular basis creating further complications for patients and clinicians alike. Magnetoelectric nanostructures have already been demonstrated for neuromodulation in vivo [203] and could similarly provide high resolution readouts from the human nervous system.

Bibliography

1. Berninger, W. H., Axel, L., Norman, D., Napel, S. & Redington, R. W. Functional imaging of the brain using computed tomography. *Radiology* **138**, 711–716 (1981).

2. Mier, W. & Mier, D. Advantages in functional imaging of the brain. *Front. Hum. Neurosci.* **9**, (2015).

3. Ludewig, P., Gdaniec, N., Sedlacik, J., Forkert, N. D., Szwargulski, P., Graeser, M., Adam, G., Kaul, M. G., Krishnan, K. M., Ferguson, R. M., Khandhar, A. P., Walczak, P., Fiehler, J., Thomalla, G., Gerloff, C., Knopp, T. & Magnus, T. Magnetic Particle Imaging for Real-Time Perfusion Imaging in Acute Stroke. *ACS Nano* **11**, 10480–10488 (2017).

4. Hochberg, L. R., Serruya, M. D., Friehs, G. M., Mukand, J. A., Saleh, M., Caplan, A. H., Branner, A., Chen, D., Penn, R. D. & Donoghue, J. P. Neuronal ensemble control of prosthetic devices by a human with tetraplegia. *Nature* **442**, 164–171 (2006).

5. Topalovic, U., Barclay, S., Ling, C., Alzuhair, A., Yu, W., Hokhikyan, V., Chandrakumar, H., Rozgic, D., Jiang, W., Basir-Kazeruni, S., Maoz, S. L., Inman, C. S., Stangl, M., Gill, J., Bari, A., Fallah, A., Eliashiv, D., Pouratian, N., Fried, I., Suthana, N. & Markovic, D. A wearable platform for closed-loop stimulation and recording of single-neuron and local field potential activity in freely moving humans. *Nat. Neurosci.* **26**, 517–527 (2023).

6. Kleinfeld, D., Luan, L., Mitra, P. P., Robinson, J. T., Sarpeshkar, R., Shepard, K., Xie, C. & Harris, T. D. Can One Concurrently Record Electrical Spikes from Every Neuron in a Mammalian Brain? *Neuron* **103**, 1005–1015 (2019).

7. Gleich, B. & Weizenecker, J. Tomographic imaging using the nonlinear response of magnetic particles. *Nature* **435**, 1214–1217 (2005).

8. Hadjikhani, A., Rodzinski, A., Wang, P., Nagesetti, A., Guduru, R., Liang, P., Runowicz, C., Shahbazmohamadi, S. & Khizroev, S. Biodistribution and clearance of magnetoelectric nanoparticles for nanomedical applications using energy dispersive spectroscopy. *Nanomed.* **12**, 1801–1822 (2017).

9. Singer, A., Dutta, S., Lewis, E., Chen, Z., Chen, J. C., Verma, N., Avants, B., Feldman, A. K., O'Malley, J., Beierlein, M., Kemere, C. & Robinson, J. T. Magnetoelectric Materials for Miniature, Wireless Neural Stimulation at Therapeutic Frequencies. *Neuron* **107**, 631-643.e5 (2020).

10. Zhang, E., Abdel-Mottaleb, M., Liang, P., Navarrete, B., Yildirim, Y. A., Campos, M. A., Smith, I. T., Wang, P., Yildirim, B., Yang, L., Chen, S., Smith, I., Lur, G., Nguyen, T., Jin, X., Noga, B. R., Ganzer, P. & Khizroev, S. Magnetic-field-synchronized wireless modulation of neural activity by magnetoelectric nanoparticles. *Brain Stimulat.* **15**, 1451–1462 (2022).

11. Yue, K., Guduru, R., Hong, J., Liang, P., Nair, M. & Khizroev, S. Magneto-Electric Nano-Particles for Non-Invasive Brain Stimulation. *PLOS ONE* **7**, e44040 (2012).

12. Kozielski, K. L., Jahanshahi, A., Gilbert, H. B., Yu, Y., Erin, Ö., Francisco, D., Alosaimi, F., Temel, Y. & Sitti, M. Nonresonant powering of injectable nanoelectrodes enables wireless deep brain stimulation in freely moving mice. *Sci. Adv.* **7**, eabc4189 (2021).

13. Guduru, R., Liang, P., Yousef, M., Horstmyer, J. & Khizroev, S. Mapping the Brain's electric fields with Magnetoelectric nanoparticles. *Bioelectron. Med.* **4**, 10 (2018).

14. Bok, I., Haber, I., Qu, X. & Hai, A. In silico assessment of electrophysiological neuronal recordings mediated by magnetoelectric nanoparticles. *Sci. Rep.* **12**, 8386 (2022).

15. Kaushik, A., Rodriguez, J., Rothen, D., Bhardwaj, V., Jayant, R. D., Pattany, P., Fuentes, B., Chand, H., Kolishetti, N., El-Hage, N., Khalili, K., Kenyon, N. S. & Nair, M. MRI-Guided, Noninvasive Delivery of Magneto-Electric Drug Nanocarriers to the Brain in a Nonhuman Primate. *ACS Appl. Bio Mater.* **2**, 4826–4836 (2019).

16. Nguyen, T., Gao, J., Wang, P., Nagesetti, A., Andrews, P., Masood, S., Vriesman, Z., Liang, P., Khizroev, S. & Jin, X. In Vivo Wireless Brain Stimulation via Non-invasive and Targeted Delivery of Magnetoelectric Nanoparticles. *Neurother. J. Am. Soc. Exp. Neurother.* (2021) doi:10.1007/s13311-021-01071-0.

17. Zaeimbashi, M., Lin, H., Dong, C., Liang, X., Nasrollahpour, M., Chen, H., Sun, N., Matyushov, A., He, Y., Wang, X., Tu, C., Wei, Y., Zhang, Y., Cash, S. S., Onabajo, M., Shrivastava, A. & Sun, N. NanoNeuroRFID: A Wireless Implantable Device Based on Magnetoelectric Antennas. *IEEE J. Electromagn. RF Microw. Med. Biol.* **3**, 206–215 (2019).

18. Zaeimbashi, M., Nasrollahpour, M., Khalifa, A., Romano, A., Liang, X., Chen, H., Sun, N., Matyushov, A., Lin, H., Dong, C., Xu, Z., Mittal, A., Martos-Repath, I., Jha, G., Mirchandani, N., Das, D., Onabajo, M., Shrivastava, A., Cash, S. & Sun, N. X. Ultra-compact dual-band smart NEMS magnetoelectric antennas for simultaneous wireless energy harvesting and magnetic field sensing. *Nat. Commun.* **12**, 3141 (2021).

19. Chen, J. C., Kan, P., Yu, Z., Alrashdan, F., Garcia, R., Singer, A., Lai, C. S. E., Avants, B., Crosby, S., Li, Z., Wang, B., Felicella, M. M., Robledo, A., Peterchev, A. V., Goetz, S. M., Hartgerink, J. D., Sheth, S. A., Yang, K. & Robinson, J. T. A wireless millimetric magnetoelectric implant for the endovascular stimulation of peripheral nerves. *Nat. Biomed. Eng.* **6**, 706–716 (2022).

20. Yu, Z., Chen, J. C., Alrashdan, F. T., Avants, B. W., He, Y., Singer, A., Robinson, J. T. & Yang, K. MagNI: A Magnetoelectrically Powered and Controlled Wireless Neurostimulating Implant. *IEEE Trans. Biomed. Circuits Syst.* **14**, 1241–1252 (2020).

21. Bandettini, P. A., Petridou, N. & Bodurka, J. Direct detection of neuronal activity with MRI: Fantasy, possibility, or reality? *Appl. Magn. Reson.* **29**, 65–88 (2005).

22. Logothetis, N. K. What we can do and what we cannot do with fMRI. *Nature* **453**, 869–878 (2008).

23. Bandettini, P. A. What's new in neuroimaging methods? *Ann. N. Y. Acad. Sci.* **1156**, 260–293 (2009).

24. Larsson, E.-M. & Wikström, J. Chapter 37 - Overview of neuroradiology. in *Handbook of Clinical Neurology* (eds. Kovacs, G. G. & Alafuzoff, I.) vol. 145 579–599 (Elsevier, 2018).

25. Lee, T., Cai, L. X., Lelyveld, V. S., Hai, A. & Jasanoff, A. Molecular-Level Functional Magnetic Resonance Imaging of Dopaminergic Signaling. *Science* **344**, 533–535 (2014).

26. Hai, A. & Jasanoff, A. Molecular fMRI. in *Brain Mapping* (ed. Toga, A. W.) 123–129 (Academic Press, Waltham, 2015). doi:10.1016/B978-0-12-397025-1.00013-0.

27. Hai, A., Cai, L. X., Lee, T., Lelyveld, V. S. & Jasanoff, A. Molecular fMRI of Serotonin Transport. *Neuron* **92**, 754–765 (2016).

28. Barandov, A., Bartelle, B. B., Williamson, C. G., Loucks, E. S., Lippard, S. J. & Jasanoff, A. Sensing intracellular calcium ions using a manganese-based MRI contrast agent. *Nat. Commun.* **10**, 897 (2019).

29. Li, N. & Jasanoff, A. Local and global consequences of reward-evoked striatal dopamine release. *Nature* **580**, 239–244 (2020).

30. Szablowski, J. O., Lee-Gosselin, A., Lue, B., Malounda, D. & Shapiro, M. G. Acoustically targeted chemogenetics for the non-invasive control of neural circuits. *Nat. Biomed. Eng.* **2**, 475–484 (2018).

31. Rabut, C., Yoo, S., Hurt, R. C., Jin, Z., Li, H., Guo, H., Ling, B. & Shapiro, M. G. Ultrasound Technologies for Imaging and Modulating Neural Activity. *Neuron* **108**, 93–110 (2020).

32. Seo, D., Neely, R. M., Shen, K., Singhal, U., Alon, E., Rabaey, J. M., Carmena, J. M. & Maharbiz, M. M. Wireless Recording in the Peripheral Nervous System with Ultrasonic Neural Dust. *Neuron* **91**, 529–539 (2016).

33. Hai, A., Spanoudaki, V. C., Bartelle, B. B. & Jasanoff, A. Wireless resonant circuits for the minimally invasive sensing of biophysical processes in magnetic resonance imaging. *Nat. Biomed. Eng.* **3**, 69–78 (2019).

34. Jasanoff, A. P., Spanoudaki, V. & Hai, A. Tunable detectors. (2020).

35. Ahrens, M. B., Orger, M. B., Robson, D. N., Li, J. M. & Keller, P. J. Whole-brain functional imaging at cellular resolution using light-sheet microscopy. *Nat. Methods* **10**, 413–420 (2013).

36. Prevedel, R., Yoon, Y.-G., Hoffmann, M., Pak, N., Wetzstein, G., Kato, S., Schrödel, T., Raskar, R., Zimmer, M., Boyden, E. S. & Vaziri, A. Simultaneous whole-animal 3D imaging of neuronal activity using light-field microscopy. *Nat. Methods* **11**, 727–730 (2014).

37. Weizenecker, J., Gleich, B., Rahmer, J., Dahnke, H. & Borgert, J. Three-dimensional real-timein vivomagnetic particle imaging. *Phys. Med. Biol.* **54**, L1–L10 (2009).

38. Orendorff, R., Peck, A. J., Zheng, B., Shirazi, S. N., Ferguson, R. M., Khandhar, A. P., Kemp, S. J., Goodwill, P., Krishnan, K. M., Brooks, G. A., Kaufer, D. & Conolly, S. Firstin vivotraumatic brain injury imaging via magnetic particle imaging. *Phys. Med. Biol.* **62**, 3501–3509 (2017).

39. Zheng, B., Vazin, T., Goodwill, P. W., Conway, A., Verma, A., Saritas, E. U., Schaffer, D. & Conolly, S. M. Magnetic Particle Imaging tracks the long-term fate of in vivo neural cell implants with high image contrast. *Sci. Rep.* **5**, 14055 (2015).

40. Meola, A., Rao, J., Chaudhary, N., Song, G., Zheng, X. & Chang, S. D. Magnetic Particle Imaging in Neurosurgery. *World Neurosurg.* **125**, 261–270 (2019).

41. Cooley, C. Z., Mandeville, J. B., Mason, E. E., Mandeville, E. T. & Wald, L. L. Rodent Cerebral Blood Volume (CBV) changes during hypercapnia observed using Magnetic Particle Imaging (MPI) detection. *NeuroImage* **178**, 713–720 (2018).

42. Herb, K., Mason, E., Mattingly, E., Mandeville, J., Mandeville, E., Cooley, C. & Wald, L. Functional MPI (fMPI) of hypercapnia in rodent brain with MPI time-series imaging. *Int. J. Magn. Part. Imaging* **6**, (2020).

43. Mason, E. E., Cooley, C. Z., Cauley, S. F., Griswold, M. A., Conolly, S. M. & Wald, L. L. Design analysis of an MPI human functional brain scanner. *Int. J. Magn. Part. Imaging* **3**, 1703008 (2017).

44. Graeser, M., Thieben, F., Szwargulski, P., Werner, F., Gdaniec, N., Boberg, M., Griese, F., Möddel, M., Ludewig, P., van de Ven, D., Weber, O. M., Woywode, O., Gleich, B. & Knopp, T. Human-sized magnetic particle imaging for brain applications. *Nat. Commun.* **10**, 1936 (2019).

45. Eerenstein, W., Mathur, N. D. & Scott, J. F. Multiferroic and magnetoelectric materials. *Nature* **442**, 759–765 (2006).

46. Hu, J.-M., Chen, L.-Q. & Nan, C.-W. Multiferroic Heterostructures Integrating Ferroelectric and Magnetic Materials. *Adv. Mater.* **28**, 15–39 (2016).

47. Liang, X., Dong, C., Chen, H., Wang, J., Wei, Y., Zaeimbashi, M., He, Y., Matyushov, A., Sun, C. & Sun, N. A Review of Thin-Film Magnetoelastic Materials for Magnetoelectric Applications. *Sensors* **20**, 1532 (2020).

48. Komalavalli, P., Banu, I. B. S., Mamat, M. H., Anwar, M. S., Hussain, S., Basha, S. S. & Rajesh, R. Enhanced magnetoelectric effect in heterogeneous multiferroic (x)CuFe2O4 − (1 − x)KNbO3 nanocomposite. *Emergent Mater.* (2022) doi:10.1007/s42247-022-00382-y.

49. Sharko, S. A., Serokurova, A. I., Novitskii, N. N., Poddubnaya, N. N., Ketsko, V. A. & Stognij, A. I. Elastically stressed state at the interface in the layered ferromagnetic / ferroelectric structures with magnetoelectric effect. *Ceram. Int.* **48**, 12387–12394 (2022).

50. Shen, J., Tada, T., Toyoki, K., Kotani, Y., Nakatani, R. & Shiratsuchi, Y. Low pressure drive of the domain wall in Pt/Co/Au/Cr2O3/Pt thin films by the magnetoelectric effect. *Appl. Phys. Lett.* **120**, 092404 (2022).

51. Li, P., Zhou, X.-S. & Guo, Z.-X. Intriguing magnetoelectric effect in two-dimensional ferromagnetic/perovskite oxide ferroelectric heterostructure. *Npj Comput. Mater.* **8**, 1–7 (2022).

52. Li, W., Lee, J. & Demkov, A. A. Extrinsic magnetoelectric effect at the BaTiO3/Ni interface. *J. Appl. Phys.* **131**, 054101 (2022).

53. Elakkiya, V. S., Sudersan, S. & Arockiarajan, A. Stress-dependent nonlinear magnetoelectric effect in press-fit composites: A numerical and experimental study. *Eur. J. Mech. - ASolids* **93**, 104536 (2022).

54. Newacheck, S. & Youssef, G. Microscale magnetoelectricity: Effect of particles geometry, distribution, and volume fraction. *J. Intell. Mater. Syst. Struct.* **33**, 1338–1348 (2022).

55. Lehmann Fernández, C. S., Pereira, N., Lanceros-Méndez, S. & Martins, P. Evaluation and optimization of the magnetoelectric response of CoFe2O4/poly(vinylidene fluoride) composite spheres by computer simulation. *Compos. Sci. Technol.* **146**, 119–130 (2017).

56. Kozielski, K. L., Jahanshahi, A., Gilbert, H. B., Yu, Y., Erin, Ö., Francisco, D., Alosaimi, F., Temel, Y. & Sitti, M. Nonresonant powering of injectable nanoelectrodes enables wireless deep brain stimulation in freely moving mice. *Sci. Adv.* **7**, eabc4189 (2021).

57. Martos-Repath, I., Mittal, A., Zaeimbashi, M., Das, D., Sun, N. X., Shrivastava, A. & Onabajo, M. Modeling of Magnetoelectric Antennas for Circuit Simulations in Magnetic Sensing Applications. in *2020 IEEE 63rd International Midwest Symposium on Circuits and Systems (MWSCAS)* 49–52 (Springfield, Massachussets, U.S.A., 2020). doi:10.1109/MWSCAS48704.2020.9184568.

58. Guduru, R. & Khizroev, S. Magnetic Field-Controlled Release of Paclitaxel Drug from Functionalized Magnetoelectric Nanoparticles. *Part. Part. Syst. Charact.* **31**, 605–611 (2014).

59. Rodzinski, A., Guduru, R., Liang, P., Hadjikhani, A., Stewart, T., Stimphil, E., Runowicz, C., Cote, R., Altman, N., Datar, R. & Khizroev, S. Targeted and controlled anticancer drug delivery and release with magnetoelectric nanoparticles. *Sci. Rep.* **6**, 20867 (2016).

60. Nair, M., Guduru, R., Liang, P., Hong, J., Sagar, V. & Khizroev, S. Externally controlled on-demand release of anti-HIV drug using magneto-electric nanoparticles as carriers. *Nat. Commun.* **4**, 1707 (2013).

61. Betal, S., Saha, A. K., Ortega, E., Dutta, M., Ramasubramanian, A. K., Bhalla, A. S. & Guo, R. Core-shell magnetoelectric nanorobot – A remotely controlled probe for targeted cell manipulation. *Sci. Rep.* **8**, 1755 (2018).

62. Dowben, P. A., Binek, C., Zhang, K., Wang, L., Mei, W.-N., Bird, J. P., Singisetti, U., Hong, X., Wang, K. L. & Nikonov, D. Towards a Strong Spin–Orbit Coupling Magnetoelectric Transistor. *IEEE J. Explor. Solid-State Comput. Devices Circuits* **4**, 1–9 (2018).

63. Mukherjee, D. & Mallick, D. Experimental Demonstration of Miniaturized Magnetoelectric Wireless Power Transfer System For Implantable Medical Devices. in *2022 IEEE 35th International Conference on Micro Electro Mechanical Systems Conference (MEMS)* 636–639 (2022). doi:10.1109/MEMS51670.2022.9699779.

64. Singer, A., Dutta, S., Lewis, E., Chen, Z., Chen, J. C., Verma, N., Avants, B., Feldman, A. K., O'Malley, J., Beierlein, M., Kemere, C. & Robinson, J. T. Magnetoelectric Materials for Miniature, Wireless Neural Stimulation at Therapeutic Frequencies. *Neuron* **107**, 631-643.e5 (2020).

65. Revathy, R., Kalarikkal, N., Varma, M. R. & Surendran, K. P. Exotic magnetic properties and enhanced magnetoelectric coupling in Fe3O4-BaTiO3 heterostructures. *J. Alloys Compd.* **889**, 161667 (2021).

66. Reaz, M., Haque, A. & Ghosh, K. Synthesis, Characterization, and Optimization of Magnetoelectric BaTiO3–Iron Oxide Core–Shell Nanoparticles. *Nanomaterials* **10**, 563 (2020).

67. Shrimali, V. G., Rathod, K. N., Dhruv, D., Zankat, A., Sagapariya, K., Solanki, S., Solanki, P. S., Shah, N. A. & Kataria, B. R. Magnetoelectric properties of Co-doped BiFeO3 nanoparticles. *Int. J. Mod. Phys. B* **32**, 1850143 (2018).

68. Matin, M. A., Hossain, M. N., Rizvi, M. H., Zubair, M. A., Hakim, M. A., Hussain, A. & Islam, M. F. Enhancing magnetoelectric and optical properties of co-doped bismuth ferrite multiferroic nanostructures. in *2017 IEEE 19th Electronics Packaging Technology Conference (EPTC)* 1–7 (2017). doi:10.1109/EPTC.2017.8277568.

69. Xia, W., Zhou, J., Hu, T., Ren, P., Zhu, G., Yin, Y., Li, J. & Zhang, Z. Enhanced magnetoelectric coefficient and interfacial compatibility by constructing a three-phase CFO@BT@PDA/P(VDF-TrFE) core-shell nanocomposite. *Compos. Part Appl. Sci. Manuf.* **131**, 105805 (2020).

70. Revathy, R., Thankachan, R. M., Kalarikkal, N., Varma, M. R. & Surendran, K. P. Sea urchin-like Ni encapsulated with BaTiO3 to form multiferroic core-shell structures for room temperature magnetoelectric sensors. *J. Alloys Compd.* **881**, 160579 (2021).

71. Song, G., Kenney, M., Chen, Y.-S., Zheng, X., Deng, Y., Chen, Z., Wang, S. X., Gambhir, S. S., Dai, H. & Rao, J. Carbon-coated FeCo nanoparticles as sensitive magnetic-particle-imaging tracers with photothermal and magnetothermal properties. *Nat. Biomed. Eng.* **4**, 325–334 (2020).

72. Kratz, H., Mohtashamdolatshahi, A., Eberbeck, D., Kosch, O., Wiekhorst, F., Taupitz, M., Hamm, B., Stolzenburg, N. & Schnorr, J. Tailored Magnetic Multicore Nanoparticles for Use as Blood Pool MPI Tracers. *Nanomaterials* **11**, 1532 (2021).

73. Israel, L. L., Galstyan, A., Holler, E. & Ljubimova, J. Y. Magnetic iron oxide nanoparticles for imaging, targeting and treatment of primary and metastatic tumors of the brain. *J. Controlled Release* **320**, 45–62 (2020).

74. Pardo, M., Roberts, E. R., Pimentel, K., Yildirim, Y. A., Navarrete, B., Wang, P., Zhang, E., Liang, P. & Khizroev, S. Size-dependent intranasal administration of magnetoelectric nanoparticles for targeted brain localization. *Nanomedicine Nanotechnol. Biol. Med.* **32**, 102337 (2021).

75. Guduru, R., Liang, P., Yousef, M., Horstmyer, J. & Khizroev, S. Mapping the Brain's electric fields with Magnetoelectric nanoparticles. *Bioelectron. Med.* **4**, 10 (2018).

76. Starmans, L. W. E., Burdinski, D., Haex, N. P. M., Moonen, R. P. M., Strijkers, G. J., Nicolay, K. & Grüll, H. Iron Oxide Nanoparticle-Micelles (ION-Micelles) for Sensitive (Molecular) Magnetic Particle Imaging and Magnetic Resonance Imaging. *PLoS ONE* **8**, e57335 (2013).

77. Maldonado-Camargo, L., Unni, M. & Rinaldi, C. Magnetic Characterization of Iron Oxide Nanoparticles for Biomedical Applications. in *Biomedical Nanotechnology: Methods and Protocols* (eds. Petrosko, S. H. & Day, E. S.) 47–71 (Springer, New York, NY, 2017). doi:10.1007/978-1-4939-6840-4_4.

78. Corral-Flores, V., Bueno-Baques, D., Carrillo-Flores, D. & Matutes-Aquino, J. A. Enhanced magnetoelectric effect in core-shell particulate composites. *J. Appl. Phys.* **99**, 08J503 (2006).

79. Brivio, S., Petti, D., Bertacco, R. & Cezar, J. C. Electric field control of magnetic anisotropies and magnetic coercivity in Fe/$BaTiO_3$(001) heterostructures. *Appl. Phys. Lett.* **98**, 092505 (2011).

80. Yang, Y. T., Song, Y. Q., Wang, D. H., Gao, J. L., Lv, L. Y., Cao, Q. Q. & Du, Y. W. Electric field control of magnetism in FePd/PMN-PT heterostructure for magnetoelectric memory devices. *J. Appl. Phys.* **115**, 024903 (2014).

81. Vaz, C. A. F. Electric field control of magnetism in multiferroic heterostructures. *J. Phys. Condens. Matter* **24**, 333201 (2012).

82. Zhang, C., Wang, F., Dong, C., Gao, C., Jia, C., Jiang, C. & Xue, D. Electric field mediated non-volatile tuning magnetism at the single-crystalline Fe/Pb($Mg_{1/3}Nb_{2/3}$)$_{0.7}Ti_{0.3}O_3$ interface. *Nanoscale* **7**, 4187–4192 (2015).

83. Chen, S., Zhang, H., Liu, F., Ye, Q., Tang, L., Huang, Z. & Wang, D. Electric field modulation of magnetism and electric properties in La-Ca-MnO_3/Pb($Zr_{0.52}Ti_{0.48}$)O_3 magnetoelectric laminate. *J. Appl. Phys.* **113**, 17C712 (2013).

84. Zhang, Y., Wang, Z., Wang, Y., Luo, C., Li, J. & Viehland, D. Electric-field induced strain modulation of magnetization in Fe-Ga/Pb($Mg_{1/3}Nb_{2/3}$)-$PbTiO_3$ magnetoelectric heterostructures. *J. Appl. Phys.* **115**, 084101 (2014).

85. Wang, J., Hu, J., Wang, H., Jiang, H., Wu, Z., Ma, J., Wang, X., Lin, Y. & Nan, C. W. Electric-field modulation of magnetic properties of Fe films directly grown on $BiScO_3$–$PbTiO_3$ ceramics. *J. Appl. Phys.* **107**, 083901 (2010).

86. Wu, T., Bur, A., Wong, K., Zhao, P., Lynch, C. S., Amiri, P. K., Wang, K. L. & Carman, G. P. Electrical control of reversible and permanent magnetization reorientation for magnetoelectric memory devices. *Appl. Phys. Lett.* **98**, 262504 (2011).

87. Thiele, C., Dörr, K., Bilani, O., Rödel, J. & Schultz, L. Influence of strain on the magnetization and magnetoelectric effect in $La_{0.7}A_{0.3}MnO_3$/PMN-PT(001)(A=Sr,Ca). *Phys. Rev. B* **75**, 054408 (2007).

88. Tournerie, N., Engelhardt, A. P., Maroun, F. & Allongue, P. Influence of the surface chemistry on the electric-field control of the magnetization of ultrathin films. *Phys. Rev. B* **86**, 104434 (2012).

89. Li, J., Li, Y., Zhu, D., Wang, Q., Zhang, Y., Zhu, Y. & Li, M. Magnetoelectric effect modulation in a PVDF/Metglas/PZT composite by applying DC electric fields on the PZT phase. *J. Alloys Compd.* **661**, 38–42 (2016).

90. Ren, S. & Wuttig, M. Magnetoelectric nano-Fe_3O_4/$CoFe_2O_4$‖$PbZr_{0.53}Ti_{0.47}O_3$ composite. *Appl. Phys. Lett.* **92**, 083502 (2008).

91. Lindemann, S., Irwin, J., Kim, G.-Y., Wang, B., Eom, K., Wang, J., Hu, J., Chen, L.-Q., Choi, S.-Y., Eom, C.-B. & Rzchowski, M. S. Low-voltage magnetoelectric coupling in membrane heterostructures. *Sci. Adv.* **7**, eabh2294.

92. Gerginov, V., Pomponio, M. & Knappe, S. Scalar Magnetometry Below 100 fT/Hz1/2 in a Microfabricated Cell. *IEEE Sens. J.* **20**, 12684–12690 (2020).

93. Ghosh, I., Liu, C. S., Swardfager, W., Lanctôt, K. L. & Anderson, N. D. The potential roles of excitatory-inhibitory imbalances and the repressor element-1 silencing transcription factor in aging and aging-associated diseases. *Mol. Cell. Neurosci.* **117**, 103683 (2021).

94. Nelson, S. B. & Valakh, V. Excitatory/Inhibitory Balance and Circuit Homeostasis in Autism Spectrum Disorders. *Neuron* **87**, 684–698 (2015).

95. Müller, M. & Österreich, M. Cerebral Microcirculatory Blood Flow Dynamics During Rest and a Continuous Motor Task. *Front. Physiol.* **10**, 1355 (2019).

96. d'Orlyé, F., Varenne, A. & Gareil, P. Determination of nanoparticle diffusion coefficients by Taylor dispersion analysis using a capillary electrophoresis instrument. *J. Chromatogr. A* **1204**, 226–232 (2008).

97. Hayes, P., Jovičević Klug, M., Toxværd, S., Durdaut, P., Schell, V., Teplyuk, A., Burdin, D., Winkler, A., Weser, R., Fetisov, Y., Höft, M., Knöchel, R., McCord, J. & Quandt, E. Converse Magnetoelectric Composite Resonator for Sensing Small Magnetic Fields. *Sci. Rep.* **9**, 16355 (2019).

98. Li, Y., Wang, Z., Yao, J., Yang, T., Wang, Z., Hu, J.-M., Chen, C., Sun, R., Tian, Z., Li, J., Chen, L.-Q. & Viehland, D. Magnetoelectric quasi-(0-3) nanocomposite heterostructures. *Nat. Commun.* **6**, 6680 (2015).

99. Sukhov, A., Jia, C., Horley, P. P. & Berakdar, J. Polarization and magnetization dynamics of a field-driven multiferroic structure. *J. Phys. Condens. Matter* **22**, 352201 (2010).

100. Yu, W., Lan, J. & Xiao, J. Magnetic Logic Gate Based on Polarized Spin Waves. *Phys. Rev. Appl.* **13**, 024055 (2020).

101. Irwin, J., Lindemann, S., Maeng, W., Wang, J. J., Vaithyanathan, V., Hu, J. M., Chen, L. Q., Schlom, D. G., Eom, C. B. & Rzchowski, M. S. Magnetoelectric Coupling by Piezoelectric Tensor Design. *Sci. Rep.* **9**, 19158 (2019).

102. Bauer, M. J., Wen, X., Tiwari, P., Arnold, D. P. & Andrew, J. S. Magnetic field sensors using arrays of electrospun magnetoelectric Janus nanowires. *Microsyst. Nanoeng.* **4**, 1–12 (2018).

103. Mushtaq, F., Torlakcik, H., Vallmajo-Martin, Q., Siringil, E. C., Zhang, J., Röhrig, C., Shen, Y., Yu, Y., Chen, X.-Z., Müller, R., Nelson, B. J. & Pané, S. Magnetoelectric 3D scaffolds for enhanced bone cell proliferation. *Appl. Mater. Today* **16**, 290–300 (2019).

104. Prabhakaran, T. & Hemalatha, J. Magnetoelectric investigations on poly(vinylidene fluoride)/NiFe 2 O 4 flexible films fabricated through a solution casting method. *RSC Adv.* **6**, 86880–86888 (2016).

105. Hu, J.-M., Duan, C.-G., Nan, C.-W. & Chen, L.-Q. Understanding and designing magnetoelectric heterostructures guided by computation: progresses, remaining questions, and perspectives. *Npj Comput. Mater.* **3**, 1–21 (2017).

106. Chen, X.-Z., Hoop, M., Shamsudhin, N., Huang, T., Özkale, B., Li, Q., Siringil, E., Mushtaq, F., Di Tizio, L., Nelson, B. J. & Pané, S. Hybrid Magnetoelectric Nanowires for Nanorobotic Applications: Fabrication, Magnetoelectric Coupling, and Magnetically Assisted In Vitro Targeted Drug Delivery. *Adv. Mater.* **29**, 1605458 (2017).

107. Vadla, S. S., Costanzo, T., John, S., Caruntu, G. & Roy, S. C. Local probing of magnetoelectric coupling in BaTiO3-Ni 1–3 composites. *Scr. Mater.* **159**, 33–36 (2019).

108. Caruso, L., Wunderle, T., Lewis, C. M., Valadeiro, J., Trauchessec, V., Trejo Rosillo, J., Amaral, J. P., Ni, J., Jendritza, P., Fermon, C., Cardoso, S., Freitas, P. P., Fries, P. & Pannetier-Lecoeur, M. In Vivo Magnetic Recording of Neuronal Activity. *Neuron* **95**, 1283-1291.e4 (2017).

109. Dong, M., Wang, X., Chen, X.-Z., Mushtaq, F., Deng, S., Zhu, C., Torlakcik, H., Terzopoulou, A., Qin, X.-H., Xiao, X., Puigmartí-Luis, J., Choi, H., Pêgo, A. P., Shen, Q.-D., Nelson, B. J. & Pané, S. 3D-Printed Soft Magnetoelectric Microswimmers for Delivery and Differentiation of Neuron-Like Cells. *Adv. Funct. Mater.* **30**, 1910323 (2020).

110. Ferguson, R. M., Minard, K. R. & Krishnan, K. M. Optimization of nanoparticle core size for magnetic particle imaging. *J. Magn. Magn. Mater.* **321**, 1548–1551 (2009).

111. Tay, Z. W., Hensley, D. W., Vreeland, E. C., Zheng, B. & Conolly, S. M. The Relaxation Wall: Experimental Limits to Improving MPI Spatial Resolution by Increasing Nanoparticle Core size. *Biomed. Phys. Eng. Express* **3**, 035003 (2017).

112. Tay, Z. W., Savliwala, S., Hensley, D. W., Fung, K. L. B., Colson, C., Fellows, B. D., Zhou, X., Huynh, Q., Lu, Y., Zheng, B., Chandrasekharan, P., Rivera-Jimenez, S. M., Rinaldi-Ramos, C. M. & Conolly, S. M. Superferromagnetic Nanoparticles Enable Order-of-Magnitude Resolution & Sensitivity Gain in Magnetic Particle Imaging. *Small Methods* **5**, 2100796 (2021).

113. Ferguson, R. M., Minard, K. R., Khandhar, A. P. & Krishnan, K. M. Optimizing magnetite nanoparticles for mass sensitivity in magnetic particle imaging. *Med. Phys.* **38**, 1619–1626 (2011).

114. Ferguson, R. M., Khandhar, A. P., Arami, H., Hua, L., Hovorka, O. & Krishnan, K. M. Tailoring the magnetic and pharmacokinetic properties of iron oxide magnetic particle imaging tracers. *Biomed. Tech. Eng.* **58**, 493–507 (2013).

115. Shi, G., Takeda, R., Trisnanto, S. B., Yamada, T., Ota, S. & Takemura, Y. Enhanced specific loss power from Resovist® achieved by aligning magnetic easy axes of nanoparticles for hyperthermia. *J. Magn. Magn. Mater.* **473**, 148–154 (2019).

116. Stein, C. R., Bezerra, M. T. S., Holanda, G. H. A., André-Filho, J. & Morais, P. C. Structural and magnetic properties of cobalt ferrite nanoparticles synthesized by co-precipitation at increasing temperatures. *AIP Adv.* **8**, 056303 (2018).

117. Wang, P., Zhang, E., Toledo, D., Smith, I. T., Navarrete, B., Furman, N., Hernandez, A. F., Telusma, M., McDaniel, D., Liang, P. & Khizroev, S. Colossal Magnetoelectric Effect in Core–Shell Magnetoelectric Nanoparticles. *Nano Lett.* **20**, 5765–5772 (2020).

118. Etier, M., Schmitz-Antoniak, C., Salamon, S., Trivedi, H., Gao, Y., Nazrabi, A., Landers, J., Gautam, D., Winterer, M., Schmitz, D., Wende, H., Shvartsman, V. V. & Lupascu, D. C.

Magnetoelectric coupling on multiferroic cobalt ferrite–barium titanate ceramic composites with different connectivity schemes. *Acta Mater.* **90**, 1–9 (2015).

119. Garraud, N., Dhavalikar, R., Maldonado-Camargo, L., Arnold, D. P. & Rinaldi, C. Design and validation of magnetic particle spectrometer for characterization of magnetic nanoparticle relaxation dynamics. *AIP Adv.* **7**, 056730 (2017).

120. Eggeman, A. S., Majetich, S. A., Farrell, D. & Pankhurst, Q. A. Size and Concentration Effects on High Frequency Hysteresis of Iron Oxide Nanoparticles. *IEEE Trans. Magn.* **43**, 2451–2453 (2007).

121. Okada, S., Bartelle, B. B., Li, N., Breton-Provencher, V., Lee, J. J., Rodriguez, E., Melican, J., Sur, M. & Jasanoff, A. Calcium-dependent molecular fMRI using a magnetic nanosensor. *Nat. Nanotechnol.* **13**, 473–477 (2018).

122. Adam, Y., Kim, J. J., Lou, S., Zhao, Y., Xie, M. E., Brinks, D., Wu, H., Mostajo-Radji, M. A., Kheifets, S., Parot, V., Chettih, S., Williams, K. J., Gmeiner, B., Farhi, S. L., Madisen, L., Buchanan, E. K., Kinsella, I., Zhou, D., Paninski, L., Harvey, C. D., Zeng, H., Arlotta, P., Campbell, R. E. & Cohen, A. E. Voltage imaging and optogenetics reveal behaviour-dependent changes in hippocampal dynamics. *Nature* **569**, 413–417 (2019).

123. Yizhar, O., Fenno, L. E., Davidson, T. J., Mogri, M. & Deisseroth, K. Optogenetics in Neural Systems. *Neuron* **71**, 9–34 (2011).

124. Chen, D.-X., Sanchez, A., Taboada, E., Roig, A., Sun, N. & Gu, H.-C. Size determination of superparamagnetic nanoparticles from magnetization curve. *J. Appl. Phys.* **105**, 083924 (2009).

125. Dung, C. T. M., Thi, N. H. T., Ta, K. H. T., Tran, V. C., Nguyen, B. T. L., Le, V. H., Do, P. A., Dang, A. T., Ju, H. & Phan, B. T. Relaxor Behaviors in $xBaTiO_3$-$(1-x)CoFe_2O_4$ Materials. *J. Magn.* **20**, 353–359 (2015).

126. Panwar, N. S. & Semwal, B. S. Study of electrical conductivity of barium titanate ceramics. *Ferroelectrics* **115**, 1–6 (1991).

127. Ajroudi, L., Mliki, N., Bessais, L., Madigou, V., Villain, S. & Leroux, Ch. Magnetic, electric and thermal properties of cobalt ferrite nanoparticles. *Mater. Res. Bull.* **59**, 49–58 (2014).

128. de Vicente, J., Bossis, G., Lacis, S. & Guyot, M. Permeability measurements in cobalt ferrite and carbonyl iron powders and suspensions. *J. Magn. Magn. Mater.* **251**, 100–108 (2002).

129. Khaja Mohaideen, K. & Joy, P. A. High magnetostriction and coupling coefficient for sintered cobalt ferrite derived from superparamagnetic nanoparticles. *Appl. Phys. Lett.* **101**, 072405 (2012).

130. George, T., Sunny, A. T. & Varghese, T. Magnetic properties of cobalt ferrite nanoparticles synthesized by sol-gel method. *IOP Conf. Ser. Mater. Sci. Eng.* **73**, 012050 (2015).

131. Bueno-Baques, D., Corral-Flores, V., Morales-Carrillo, N. A., Torres, A., Camacho-Montes, H. & Ziolo, R. F. Structural and Magnetic Properties of Cobal Ferrite - Barium Titanate Nanotube Arrays. *MRS Online Proc. Libr.* **1368**, 108 (2011).

132. Avakian, A. & Ricoeur, A. Constitutive modeling of nonlinear reversible and irreversible ferromagnetic behaviors and application to multiferroic composites. *J. Intell. Mater. Syst. Struct.* **27**, 2536–2554 (2016).

133. Li, Z., Fisher, E. S., Liu, J. Z. & Nevitt, M. V. Single-crystal elastic constants of Co-Al and Co-Fe spinels. *J. Mater. Sci.* **26**, 2621–2624 (1991).

134. Lindén, H., Hagen, E., Leski, S., Norheim, E., Pettersen, K. & Einevoll, G. LFPy: a tool for biophysical simulation of extracellular potentials generated by detailed model neurons. *Front. Neuroinformatics* **7**, 41 (2014).

135. Dura-Bernal, S., Suter, B. A., Gleeson, P., Cantarelli, M., Quintana, A., Rodriguez, F., Kedziora, D. J., Chadderdon, G. L., Kerr, C. C., Neymotin, S. A., McDougal, R. A., Hines, M., Shepherd, G. M. & Lytton, W. W. NetPyNE, a tool for data-driven multiscale modeling of brain circuits. *eLife* **8**, e44494 (2019).

136. Carnevale, N. T. & Hines, M. L. *The NEURON Book*. (Cambridge University Press, 2006).

137. Aberra, A. S., Peterchev, A. V. & Grill, W. M. Biophysically realistic neuron models for simulation of cortical stimulation. *J. Neural Eng.* **15**, 066023 (2018).

138. Markram, H., Muller, E., Ramaswamy, S., Reimann, M. W., Abdellah, M., Sanchez, C. A., Ailamaki, A., Alonso-Nanclares, L., Antille, N., Arsever, S., Kahou, G. A. A., Berger, T. K., Bilgili, A., Buncic, N., Chalimourda, A., Chindemi, G., Courcol, J.-D., Delalondre, F., Delattre, V., Druckmann, S., Dumusc, R., Dynes, J., Eilemann, S., Gal, E., Gevaert, M. E., Ghobril, J.-P., Gidon, A., Graham, J. W., Gupta, A., Haenel, V., Hay, E., Heinis, T., Hernando, J. B., Hines, M., Kanari, L., Keller, D., Kenyon, J., Khazen, G., Kim, Y., King, J. G., Kisvarday, Z., Kumbhar, P., Lasserre, S., Le Bé, J.-V., Magalhães, B. R. C., Merchán-Pérez, A., Meystre, J., Morrice, B. R., Muller, J., Muñoz-Céspedes, A., Muralidhar, S., Muthurasa, K., Nachbaur, D., Newton, T. H., Nolte, M., Ovcharenko, A., Palacios, J., Pastor, L., Perin, R., Ranjan, R., Riachi, I., Rodríguez, J.-R., Riquelme, J. L., Rössert, C., Sfyrakis, K., Shi, Y., Shillcock, J. C., Silberberg, G., Silva, R., Tauheed, F., Telefont, M., Toledo-Rodriguez, M., Tränkler, T., Van Geit, W., Díaz, J. V., Walker, R., Wang, Y., Zaninetta, S. M., DeFelipe, J., Hill, S. L., Segev, I. & Schürmann, F. Reconstruction and Simulation of Neocortical Microcircuitry. *Cell* **163**, 456–492 (2015).

139. Spaldin, N. A. & Ramesh, R. Advances in magnetoelectric multiferroics. *Nat. Mater.* **18**, 203–212 (2019).

140. Manipatruni, S., Nikonov, D. E., Lin, C.-C., Gosavi, T. A., Liu, H., Prasad, B., Huang, Y.-L., Bonturim, E., Ramesh, R. & Young, I. A. Scalable energy-efficient magnetoelectric spin–orbit logic. *Nature* **565**, 35–42 (2019).

141. Wang, Y., Wang, L., Xia, J., Lai, Z., Tian, G., Zhang, X., Hou, Z., Gao, X., Mi, W., Feng, C., Zeng, M., Zhou, G., Yu, G., Wu, G., Zhou, Y., Wang, W., Zhang, X. & Liu, J. Electric-field-driven non-volatile multi-state switching of individual skyrmions in a multiferroic heterostructure. *Nat. Commun.* **11**, 3577 (2020).

142. Baumgaertl, K. & Grundler, D. Reversal of nanomagnets by propagating magnons in ferrimagnetic yttrium iron garnet enabling nonvolatile magnon memory. *Nat. Commun.* **14**, 1490 (2023).

143. Dieny, B., Prejbeanu, I. L., Garello, K., Gambardella, P., Freitas, P., Lehndorff, R., Raberg, W., Ebels, U., Demokritov, S. O., Akerman, J., Deac, A., Pirro, P., Adelmann, C., Anane, A., Chumak, A. V., Hirohata, A., Mangin, S., Valenzuela, S. O., Onbaşlı, M. C., d'Aquino, M., Prenat, G., Finocchio, G., Lopez-Diaz, L., Chantrell, R., Chubykalo-Fesenko, O. & Bortolotti, P. Opportunities and challenges for spintronics in the microelectronics industry. *Nat. Electron.* **3**, 446–459 (2020).

144. Apu, E. H., Nafiujjaman, M., Sandeep, S., V. Makela, A., Khaleghi, A., Vainio, S., H. Contag, C., Li, J., Balasingham, I., Kim, T. & Ashammakhi, N. Biomedical applications of multifunctional magnetoelectric nanoparticles. *Mater. Chem. Front.* **6**, 1368–1390 (2022).

145. Bok, I., Haber, I., Qu, X. & Hai, A. In silico assessment of electrophysiological neuronal recordings mediated by magnetoelectric nanoparticles. *Sci. Rep.* **12**, 8386 (2022).

146. Nguyen, T., Gao, J., Wang, P., Nagesetti, A., Andrews, P., Masood, S., Vriesman, Z., Liang, P., Khizroev, S. & Jin, X. In Vivo Wireless Brain Stimulation via Non-invasive and Targeted Delivery of Magnetoelectric Nanoparticles. *Neurother. J. Am. Soc. Exp. Neurother.* **18**, 2091–2106 (2021).

147. Bok, I., Vareberg, A., Gokhale, Y., Bhatt, S., Masterson, E., Phillips, J., Zhu, T., Ren, X. & Hai, A. Wireless agents for brain recording and stimulation modalities. *Bioelectron. Med.* **9**, 20 (2023).

148. Zhang, J., Chen, M., Chen, J., Yamamoto, K., Wang, H., Hamdi, M., Sun, Y., Wagner, K., He, W., Zhang, Y., Ma, J., Gao, P., Han, X., Yu, D., Maletinsky, P., Ansermet, J.-P., Maekawa, S., Grundler, D., Nan, C.-W. & Yu, H. Long decay length of magnon-polarons in BiFeO3/La0.67Sr0.33MnO3 heterostructures. *Nat. Commun.* **12**, 7258 (2021).

149. Liu, C., Luo, Y., Hong, D., Zhang, S. S.-L., Saglam, H., Li, Y., Lin, Y., Fisher, B., Pearson, J. E., Jiang, J. S., Zhou, H., Wen, J., Hoffmann, A. & Bhattacharya, A. Electric field control of magnon spin currents in an antiferromagnetic insulator. *Sci. Adv.* **7**, eabg1669 (2021).

150. Vaz, D. C., Lin, C.-C., Plombon, J. J., Choi, W. Y., Groen, I., Arango, I. C., Chuvilin, A., Hueso, L. E., Nikonov, D. E., Li, H., Debashis, P., Clendenning, S. B., Gosavi, T. A.,

Huang, Y.-L., Prasad, B., Ramesh, R., Vecchiola, A., Bibes, M., Bouzehouane, K., Fusil, S., Garcia, V., Young, I. A. & Casanova, F. Voltage-based magnetization switching and reading in magnetoelectric spin-orbit nanodevices. *Nat. Commun.* **15**, 1902 (2024).

151. Ba, Y., Zhuang, S., Zhang, Y., Wang, Y., Gao, Y., Zhou, H., Chen, M., Sun, W., Liu, Q., Chai, G., Ma, J., Zhang, Y., Tian, H., Du, H., Jiang, W., Nan, C., Hu, J.-M. & Zhao, Y. Electric-field control of skyrmions in multiferroic heterostructure via magnetoelectric coupling. *Nat. Commun.* **12**, 322 (2021).

152. Hayami, S., Okubo, T. & Motome, Y. Phase shift in skyrmion crystals. *Nat. Commun.* **12**, 6927 (2021).

153. Yao, F., Multian, V., Wang, Z., Ubrig, N., Teyssier, J., Wu, F., Giannini, E., Gibertini, M., Gutiérrez-Lezama, I. & Morpurgo, A. F. Multiple antiferromagnetic phases and magnetic anisotropy in exfoliated CrBr3 multilayers. *Nat. Commun.* **14**, 4969 (2023).

154. Juge, R., Sisodia, N., Larrañaga, J. U., Zhang, Q., Pham, V. T., Rana, K. G., Sarpi, B., Mille, N., Stanescu, S., Belkhou, R., Mawass, M.-A., Novakovic-Marinkovic, N., Kronast, F., Weigand, M., Gräfe, J., Wintz, S., Finizio, S., Raabe, J., Aballe, L., Foerster, M., Belmeguenai, M., Buda-Prejbeanu, L. D., Pelloux-Prayer, J., Shaw, J. M., Nembach, H. T., Ranno, L., Gaudin, G. & Boulle, O. Skyrmions in synthetic antiferromagnets and their nucleation via electrical current and ultra-fast laser illumination. *Nat. Commun.* **13**, 4807 (2022).

155. Xu, S., Wang, J., Chen, P., Jin, K., Ma, C., Wu, S., Guo, E., Ge, C., Wang, C., Xu, X., Yao, H., Wang, J., Xie, D., Wang, X., Chang, K., Bai, X. & Yang, G. Magnetoelectric coupling in multiferroics probed by optical second harmonic generation. *Nat. Commun.* **14**, 2274 (2023).

156. Ghidini, M., Mansell, R., Maccherozzi, F., Moya, X., Phillips, L. C., Yan, W., Pesquera, D., Barnes, C. H. W., Cowburn, R. P., Hu, J.-M., Dhesi, S. S. & Mathur, N. D. Shear-strain-mediated magnetoelectric effects revealed by imaging. *Nat. Mater.* **18**, 840–845 (2019).

157. Kocsis, V., Nakajima, T., Matsuda, M., Kikkawa, A., Kaneko, Y., Takashima, J., Kakurai, K., Arima, T., Kagawa, F., Tokunaga, Y., Tokura, Y. & Taguchi, Y. Magnetization-polarization cross-control near room temperature in hexaferrite single crystals. *Nat. Commun.* **10**, 1247 (2019).

158. Ren, L., Guo, K., Cui, R., Zhang, M., Wang, X. & Deng, C. Tuning magnetoelectric effect in Bi6Fe1.6Co0.2Ni0.2Ti3O18/La0.7Sr0.3MnO3/Bi6Fe1.6Co0.2Ni0.2Ti3O18 sandwich films employing micromagnetic moments and force on dipole. *Appl. Surf. Sci.* **638**, 158092 (2023).

159. Peddigari, M., Woo, K., Kim, S.-D., Kwak, M. S., Jeong, J. W., Kang, J.-H., Lee, S.-H., Park, J. H., Park, K.-I., Annapureddy, V., Jang, J., Min, Y., Ahn, C.-W., Choi, J.-J., Hahn, B.-D., Yoon, W.-H., Ryu, J. & Hwang, G.-T. Ultra-magnetic field sensitive magnetoelectric composite with sub-pT detection limit at low frequency enabled by flash photon annealing. *Nano Energy* **90**, 106598 (2021).

160. Guan, G., Gao, G., Xiang, J., Yang, J., Gong, L., Chen, X., Zhang, Y., Zhang, K. & Meng, X. CoFe2/BaTiO3 Hybrid Nanofibers for Microwave Absorption. *ACS Appl. Nano Mater.* **3**, 8424–8437 (2020).

161. Prasad, B., Huang, Y.-L., Chopdekar, R. V., Chen, Z., Steffes, J., Das, S., Li, Q., Yang, M., Lin, C.-C., Gosavi, T., Nikonov, D. E., Qiu, Z. Q., Martin, L. W., Huey, B. D., Young, I., Íñiguez, J., Manipatruni, S. & Ramesh, R. Ultralow Voltage Manipulation of Ferromagnetism. *Adv. Mater. Deerfield Beach Fla* **32**, e2001943 (2020).

162. Pan, Z., Donthu, S. K., Wu, N., Li, S. & Dravid, V. P. Directed Fabrication of Radially Stacked Multifunctional Oxide Heterostructures Using Soft Electron-Beam Lithography. *Small* **2**, 274–280 (2006).

163. Fiocchi, S., Chiaramello, E., Marrella, A., Suarato, G., Bonato, M., Parazzini, M. & Ravazzani, P. Modeling of core-shell magneto-electric nanoparticles for biomedical applications: Effect of composition, dimension, and magnetic field features on magnetoelectric response. *PLOS ONE* **17**, e0274676 (2022).

164. Marrella, A., Suarato, G., Fiocchi, S., Chiaramello, E., Bonato, M., Parazzini, M. & Ravazzani, P. Magnetoelectric nanoparticles shape modulates their electrical output. *Front. Bioeng. Biotechnol.* **11**, (2023).

165. Etier, M., Shvartsman, V. V., Salamon, S., Gao, Y., Wende, H. & Lupascu, D. C. The Direct and the Converse Magnetoelectric Effect in Multiferroic Cobalt Ferrite–Barium Titanate Ceramic Composites. *J. Am. Ceram. Soc.* **99**, 3623–3631 (2016).

166. Etier, M., Schmitz-Antoniak, C., Salamon, S., Trivedi, H., Gao, Y., Nazrabi, A., Landers, J., Gautam, D., Winterer, M., Schmitz, D., Wende, H., Shvartsman, V. V. & Lupascu, D. C. Magnetoelectric coupling on multiferroic cobalt ferrite–barium titanate ceramic composites with different connectivity schemes. *Acta Mater.* **90**, 1–9 (2015).

167. Shvartsman, V. V., Alawneh, F., Borisov, P., Kozodaev, D. & Lupascu, D. C. Converse magnetoelectric effect in CoFe2O4–BaTiO3composites with a core–shell structure. *Smart Mater. Struct.* **20**, 075006 (2011).

168. Patel, S. K., Karaba, C. T., Robertson, D. D., Chang, J., Fitzell, K., Salamat, C. Z., Chang, J. P. & Tolbert, S. H. Increased Magnetoelectric Coupling in Porous Nanocomposites of CoFe2O4 and BiFeO3 with Residual Porosity for Switchable Magnetic Devices. *ACS Appl. Nano Mater.* **6**, 4141–4150 (2023).

169. Tang, X., Viswan, R., Gao, M., Leung, C. M., Folger, C., Luo, H., Howe, B., Li, J. & Viehland, D. Nanopillars with E-field accessible multi-state ($N \geq 4$) magnetization having giant magnetization changes in self-assembled BiFeO3-CoFe2O4/Pb(Mg1/3Nb2/3)-38at%PbTiO3 heterostructures. *Sci. Rep.* **8**, 1628 (2018).

170. JPK NanoWizard ULTRA Speed 2. https://www.bruker.com/en/products-and-solutions/microscopes/bioafm/jpk-nanowizard-ultra-speed-2.html.

171. Zhang, Y., Sun, W., Cao, K., Yang, X.-X., Yang, Y., Lu, S., Du, A., Hu, C., Feng, C., Wang, Y., Cai, J., Cui, B., Piao, H.-G., Zhao, W. & Zhao, Y. Electric-field control of nonvolatile resistance state of perpendicular magnetic tunnel junction via magnetoelectric coupling. *Sci. Adv.* **10**, eadl4633 (2024).

172. Wittrock, S., Perna, S., Lebrun, R., Ho, K., Dutra, R., Ferreira, R., Bortolotti, P., Serpico, C. & Cros, V. Non-hermiticity in spintronics: oscillation death in coupled spintronic nano-oscillators through emerging exceptional points. *Nat. Commun.* **15**, 971 (2024).

173. Ramezani, Z., André, V. & Khizroev, S. Modeling the effect of magnetoelectric nanoparticles on neuronal electrical activity: An analog circuit approach. *Biointerphases* **19**, 031001 (2024).

174. Chen, S., Zhang, E., Navarrete, B., Yildrim, Y. A., Abdel-Mottaleb, M., Campos, M. A., Smith, I. T., Liang, P. & Khizroev, S. Magnetic Properties of Magnetoelectric Nanoparticles With Varying Core–Shell Ratios and Their Effects on In Vitro Neuron Stimulation. *IEEE Trans. Magn.* **59**, 1–4 (2023).

175. Alosaimi, F., Dominguez-Paredes, D., Knoben, R., Almasabi, F., Hescham, S., Kozielski, K., Temel, Y. & Jahanshahi, A. Wireless stimulation of the subthalamic nucleus with nanoparticles modulates key monoaminergic systems similar to contemporary deep brain stimulation. *Behav. Brain Res.* **444**, 114363 (2023).

176. Kumari, P., Wunderlich, H., Milojkovic, A., López, J. E., Fossati, A., Jahanshahi, A. & Kozielski, K. Multiscale Modeling of Magnetoelectric Nanoparticles for the Analysis of Spatially Selective Neural Stimulation. *Adv. Healthc. Mater.* **n/a**, 2302871 (2024).

177. Anastassiou, C. A., Perin, R., Markram, H. & Koch, C. Ephaptic coupling of cortical neurons. *Nat. Neurosci.* **14**, 217–223 (2011).

178. Bok, I., Rauch, B., Ashtiani, A. & Hai, A. Direct observation of NMR transverse relaxation in nanopatterned clusters of iron oxide particles. *Magn. Reson. Med.* **91**, 687–698 (2024).

179. Abraham, A. R., Raneesh, B., Woldu, T., Aškrabić, S., Lazović, S., Dohčević-Mitrović, Z., Oluwafemi, O. S., Thomas, S. & Kalarikkal, N. Realization of Enhanced Magnetoelectric Coupling and Raman Spectroscopic Signatures in 0–0 Type Hybrid Multiferroic Core–Shell Geometric Nanostructures. *J. Phys. Chem. C* **121**, 4352–4362 (2017).

180. Kumar Saha, S., Azizar Rahman, M. & Akther Hossain, A. K. M. Tuning the magnetic and magnetoelectric response in Bi1-xYxFe0.7Mn0.3O3 multiferroics. *J. Magn. Magn. Mater.* **581**, 170988 (2023).

181. Islam, R. A. & Priya, S. Effect of piezoelectric grain size on magnetoelectric coefficient of Pb(Zr0.52Ti0.48)O3–Ni0.8Zn0.2Fe2O4 particulate composites. *J. Mater. Sci.* **43**, 3560–3568 (2008).

182. Ludewig, P., Graeser, M., Forkert, N. D., Thieben, F., Rández-Garbayo, J., Rieckhoff, J., Lessmann, K., Förger, F., Szwargulski, P., Magnus, T. & Knopp, T. Magnetic particle

imaging for assessment of cerebral perfusion and ischemia. *WIREs Nanomedicine Nanobiotechnology* **14**, e1757 (2022).

183. Hike, D., Liu, X., Xie, Z., Zhang, B., Choi, S., Zhou, X. A., Liu, A., Murstein, A., Jiang, Y., Devor, A. & Yu, X. High-resolution awake mouse fMRI at 14 Tesla. *eLife* **13**, (2024).

184. Feinberg, D. A., Beckett, A. J. S., Vu, A. T., Stockmann, J., Huber, L., Ma, S., Ahn, S., Setsompop, K., Cao, X., Park, S., Liu, C., Wald, L. L., Polimeni, J. R., Mareyam, A., Gruber, B., Stirnberg, R., Liao, C., Yacoub, E., Davids, M., Bell, P., Rummert, E., Koehler, M., Potthast, A., Gonzalez-Insua, I., Stocker, S., Gunamony, S. & Dietz, P. Next-generation MRI scanner designed for ultra-high-resolution human brain imaging at 7 Tesla. *Nat. Methods* **20**, 2048–2057 (2023).

185. Nenning, K.-H. & Langs, G. Machine learning in neuroimaging: from research to clinical practice. *Radiol. Heidelb. Ger.* **62**, 1–10 (2022).

186. Wang, S., Li, L., Zhang, S., Jiang, Q., Li, P., Wang, C., Xiao, R., Li, X.-M. & Song, J. Multifunctional ultraflexible neural probe for wireless optogenetics and electrophysiology. *Giant* **18**, 100272 (2024).

187. Silva, A. B., Liu, J. R., Metzger, S. L., Bhaya-Grossman, I., Dougherty, M. E., Seaton, M. P., Littlejohn, K. T., Tu-Chan, A., Ganguly, K., Moses, D. A. & Chang, E. F. A bilingual speech neuroprosthesis driven by cortical articulatory representations shared between languages. *Nat. Biomed. Eng.* 1–15 (2024) doi:10.1038/s41551-024-01207-5.

188. Chaudhary, U., Vlachos, I., Zimmermann, J. B., Espinosa, A., Tonin, A., Jaramillo-Gonzalez, A., Khalili-Ardali, M., Topka, H., Lehmberg, J., Friehs, G. M., Woodtli, A., Donoghue, J. P. & Birbaumer, N. Spelling interface using intracortical signals in a completely locked-in patient enabled via auditory neurofeedback training. *Nat. Commun.* **13**, 1236 (2022).

189. Lee, K., Paulk, A. C., Ro, Y. G., Cleary, D. R., Tonsfeldt, K. J., Kfir, Y., Pezaris, J. S., Tchoe, Y., Lee, J., Bourhis, A. M., Vatsyayan, R., Martin, J. R., Russman, S. M., Yang, J. C., Baohan, A., Richardson, R. M., Williams, Z. M., Fried, S. I., Hoi Sang, U., Raslan, A. M., Ben-Haim, S., Halgren, E., Cash, S. S. & Dayeh, S. A. Flexible, scalable, high channel count stereo-electrode for recording in the human brain. *Nat. Commun.* **15**, 218 (2024).

190. Homer, M. L., Nurmikko, A. V., Donoghue, J. P. & Hochberg, L. R. Sensors and Decoding for Intracortical Brain Computer Interfaces. *Annu. Rev. Biomed. Eng.* **15**, 383–405 (2013).

191. Kipke, D. R., Vetter, R. J., Williams, J. C. & Hetke, J. F. Silicon-substrate intracortical microelectrode arrays for long-term recording of neuronal spike activity in cerebral cortex. *IEEE Trans. Neural Syst. Rehabil. Eng.* **11**, 151–155 (2003).

192. Maynard, E. M., Nordhausen, C. T. & Normann, R. A. The Utah Intracortical Electrode Array: A recording structure for potential brain-computer interfaces. *Electroencephalogr. Clin. Neurophysiol.* **102**, 228–239 (1997).

193. Weizenecker, J., Gleich, B. & Borgert, J. Magnetic particle imaging using a field free line. *J. Phys. Appl. Phys.* **41**, 105009 (2008).

194. Vogel, P., Rückert, M. A., Klauer, P., Kullmann, W. H., Jakob, P. M. & Behr, V. C. Superspeed Traveling Wave Magnetic Particle Imaging. *IEEE Trans. Magn.* **51**, 1–3 (2015).

195. Vogel, P., Rückert, M. A., Kampf, T., Herz, S., Stang, A., Wöckel, L., Bley, T. A., Dutz, S. & Behr, V. C. Superspeed bolus visualization for vascular magnetic particle imaging. *IEEE Trans. Med. Imaging* **39**, 2133–2139 (2020).

196. Vogel, P., Kampf, T., Herz, S., Rückert, M. A., Bley, T. A. & Behr, V. C. Parallel magnetic particle imaging. *Rev. Sci. Instrum.* **91**, 045117 (2020).

197. Vogel, P., Lother, S., Rückert, M. A., Kullmann, W. H., Jakob, P. M., Fidler, F. & Behr, V. C. MRI Meets MPI: A Bimodal MPI-MRI Tomograph. *IEEE Trans. Med. Imaging* **33**, 1954–1959 (2014).

198. Vogel, P., Markert, J., Rückert, M. A., Herz, S., Keßler, B., Dremel, K., Althoff, D., Weber, M., Buzug, T. M., Bley, T. A., Kullmann, W. H., Hanke, R., Zabler, S. & Behr, V. C. Magnetic Particle Imaging meets Computed Tomography: first simultaneous imaging. *Sci. Rep.* **9**, 12627 (2019).

199. Mattingly, E., Sliwiak, M., Chacon-Caldera, J., Barksdale, A., Niebel, F., Mason, E. & Wald, L. A Human-Scale Magnetic Particle Imaging System for Functional Neuroimaging. *Int. J. Magn. Part. Imaging IJMPI* **10**, (2024).

200. Zhang, E., Abdel-Mottaleb, M., Liang, P., Navarrete, B., Yildirim, Y. A., Campos, M. A., Smith, I. T., Wang, P., Yildirim, B., Yang, L., Chen, S., Smith, I., Lur, G., Nguyen, T., Jin, X., Noga, B. R., Ganzer, P. & Khizroev, S. Magnetic-field-synchronized wireless modulation of neural activity by magnetoelectric nanoparticles. *Brain Stimulat.* **15**, 1451–1462 (2022).

201. Kozielski, K. L., Jahanshahi, A., Gilbert, H. B., Yu, Y., Erin, Ö., Francisco, D., Alosaimi, F., Temel, Y. & Sitti, M. Nonresonant powering of injectable nanoelectrodes enables wireless deep brain stimulation in freely moving mice. *Sci. Adv.* **7**, eabc4189 (2021).

202. Pardo, M., Roberts, E. R., Pimentel, K., Yildirim, Y. A., Navarrete, B., Wang, P., Zhang, E., Liang, P. & Khizroev, S. Size-dependent intranasal administration of magnetoelectric nanoparticles for targeted brain localization. *Nanomedicine Nanotechnol. Biol. Med.* **32**, 102337 (2021).

203. Kim, Y. J., Driscoll, N., Kent, N., Paniagua, E. V., Tabet, A., Koehler, F., Manthey, M., Sahasrabudhe, A., Signorelli, L., Gregureć, D. & Anikeeva, P. Magnetoelectric Nanodiscs Enable Wireless Transgene-Free Neuromodulation. 2023.12.24.573272 Preprint at https://doi.org/10.1101/2023.12.24.573272 (2023).

204. Ball, J. P., Mound, B. A., Nino, J. C. & Allen, J. B. Biocompatible evaluation of barium titanate foamed ceramic structures for orthopedic applications. *J. Biomed. Mater. Res. A* **102**, 2089–2095 (2014).

205. Polley, C., Distler, T., Scheufler, C., Detsch, R., Lund, H., Springer, A., Schneidereit, D., Friedrich, O., Boccaccini, A. R. & Seitz, H. 3D printing of piezoelectric and bioactive barium titanate-bioactive glass scaffolds for bone tissue engineering. *Mater. Today Bio* **21**, 100719 (2023).

206. Park, J. B., Kelly, B. J., Kenner, G. H., von Recum, A. F., Grether, M. F. & Coffeen, W. W. Piezoelectric ceramic implants: in vivo results. *J. Biomed. Mater. Res.* **15**, 103–110 (1981).

207. Bok, I., Haber, I., Qu, X. & Hai, A. In silico assessment of electrophysiological neuronal recordings mediated by magnetoelectric nanoparticles. *Sci. Rep.* **12**, 8386 (2022).

208. Zhang, E., Liang, P., Yildirim, Y. A., Chen, S., Abdel-Mottaleb, M., Shotbolt, M., Ramezani, Z., Tian, J., Andre, V. & Khizroev, S. Ab Initio Physics Considerations in The Design of Wireless and Non-invasive Neural Recording Systems Using MagnetoElectric Nanoparticles. *IEEE Trans. Magn.* 1–1 (2023) doi:10.1109/TMAG.2023.3300791.

209. Fiocchi, S., Chiaramello, E., Marrella, A., Bonato, M., Parazzini, M. & Ravazzani, P. Modelling of magnetoelectric nanoparticles for non-invasive brain stimulation: a computational study. *J. Neural Eng.* **19**, 056020 (2022).

210. Zabow, G. Reflow transfer for conformal three-dimensional microprinting. *Science* **378**, 894–898 (2022).

211. Guduru, R., Liang, P., Hong, J., Rodzinski, A., Hadjikhani, A., Horstmyer, J., Levister, E. & Khizroev, S. Magnetoelectric 'spin' on stimulating the brain. *Nanomed.* **10**, 2051–2061 (2015).

212. Hadjikhani, A., Rodzinski, A., Wang, P., Nagesetti, A., Guduru, R., Liang, P., Runowicz, C., Shahbazmohamadi, S. & Khizroev, S. Biodistribution and clearance of magnetoelectric nanoparticles for nanomedical applications using energy dispersive spectroscopy. *Nanomed.* **12**, 1801–1822 (2017).

213. Hai, A. In-Cell Recording and Stimulation by Engulfment Mechanisms. in *Nanotechnology and Neuroscience: Nano-electronic, Photonic and Mechanical Neuronal Interfacing* (eds. De Vittorio, M., Martiradonna, L. & Assad, J.) 45–70 (Springer, New York, NY, 2014). doi:10.1007/978-1-4899-8038-0_3.

214. Hai, A., Kamber, D., Malkinson, G., Erez, H., Mazurski, N., Shappir, J. & Spira, M. E. Changing gears from chemical adhesion of cells to flat substrata toward engulfment of micro-protrusions by active mechanisms. *J. Neural Eng.* **6**, 066009 (2009).

215. Hai, A., Dormann, A., Shappir, J., Yitzchaik, S., Bartic, C., Borghs, G., Langedijk, J. P. M. & Spira, M. E. Spine-shaped gold protrusions improve the adherence and electrical

coupling of neurons with the surface of micro-electronic devices. *J. R. Soc. Interface* **6**, 1153–1165 (2009).

216. Hai, A., Shappir, J. & Spira, M. E. Long-Term, Multisite, Parallel, In-Cell Recording and Stimulation by an Array of Extracellular Microelectrodes. *J. Neurophysiol.* **104**, 559–568 (2010).

217. Hai, A. & Spira, M. E. On-chip electroporation, membrane repair dynamics and transient in-cell recordings by arrays of gold mushroom-shaped microelectrodes. *Lab. Chip* **12**, 2865–2873 (2012).

218. Spira, M. E. & Hai, A. Multi-electrode array technologies for neuroscience and cardiology. *Nat. Nanotechnol.* **8**, 83–94 (2013).

219. Gleich, B. & Weizenecker, J. Tomographic imaging using the nonlinear response of magnetic particles. *Nature* **435**, 1214–1217 (2005).

220. Ludewig, P., Gdaniec, N., Sedlacik, J., Forkert, N. D., Szwargulski, P., Graeser, M., Adam, G., Kaul, M. G., Krishnan, K. M., Ferguson, R. M., Khandhar, A. P., Walczak, P., Fiehler, J., Thomalla, G., Gerloff, C., Knopp, T. & Magnus, T. Magnetic Particle Imaging for Real-Time Perfusion Imaging in Acute Stroke. *ACS Nano* **11**, 10480–10488 (2017).

221. Saritas, E. U., Goodwill, P. W., Zhang, G. Z. & Conolly, S. M. Magnetostimulation Limits in Magnetic Particle Imaging. *IEEE Trans. Med. Imaging* **32**, 1600–1610 (2013).

222. Pantke, D., Holle, N., Mogarkar, A., Straub, M. & Schulz, V. Multifrequency magnetic particle imaging enabled by a combined passive and active drive field feed-through compensation approach. *Med. Phys.* **46**, 4077–4086 (2019).

223. Vogel, P., Rückert, M. A., Greiner, C., Günther, J., Reichl, T., Kampf, T., Bley, T. A., Behr, V. C. & Herz, S. iMPI: portable human-sized magnetic particle imaging scanner for real-time endovascular interventions. *Sci. Rep.* **13**, 10472 (2023).

224. Ogawa, S., Lee, T. M., Kay, A. R. & Tank, D. W. Brain magnetic resonance imaging with contrast dependent on blood oxygenation. *Proc. Natl. Acad. Sci. U. S. A.* **87**, 9868–9872 (1990).

225. Belliveau, J. W., Kennedy, D. N., McKinstry, R. C., Buchbinder, B. R., Weisskoff, R. M., Cohen, M. S., Vevea, J. M., Brady, T. J. & Rosen, B. R. Functional mapping of the human visual cortex by magnetic resonance imaging. *Science* **254**, 716–719 (1991).

226. Kwong, K. K., Belliveau, J. W., Chesler, D. A., Goldberg, I. E., Weisskoff, R. M., Poncelet, B. P., Kennedy, D. N., Hoppel, B. E., Cohen, M. S. & Turner, R. Dynamic magnetic resonance imaging of human brain activity during primary sensory stimulation. *Proc. Natl. Acad. Sci. U. S. A.* **89**, 5675–5679 (1992).

227. Logothetis, N. K. The underpinnings of the BOLD functional magnetic resonance imaging signal. *J. Neurosci. Off. J. Soc. Neurosci.* **23**, 3963–3971 (2003).

228. Logothetis, N. K., Pauls, J., Augath, M., Trinath, T. & Oeltermann, A. Neurophysiological investigation of the basis of the fMRI signal. *Nature* **412**, 150–157 (2001).

229. Eklund, A., Nichols, T. E. & Knutsson, H. Cluster failure: Why fMRI inferences for spatial extent have inflated false-positive rates. *Proc. Natl. Acad. Sci. U. S. A.* **113**, 7900–7905 (2016).

230. Choi, S.-H., Im, G. H., Choi, S., Yu, X., Bandettini, P. A., Menon, R. S. & Kim, S.-G. No replication of direct neuronal activity-related (DIANA) fMRI in anesthetized mice. *Sci. Adv.* **10**, eadl0999 (2024).

231. Toi, P. T., Jang, H. J., Min, K., Kim, S.-P., Lee, S.-K., Lee, J., Kwag, J. & Park, J.-Y. In vivo direct imaging of neuronal activity at high temporospatial resolution. *Science* **378**, 160–168 (2022).

232. Hu, J.-M. & Nan, C.-W. Opportunities and challenges for magnetoelectric devices. *APL Mater.* **7**, 080905 (2019).

233. Barry, J. F., Turner, M. J., Schloss, J. M., Glenn, D. R., Song, Y., Lukin, M. D., Park, H. & Walsworth, R. L. Optical magnetic detection of single-neuron action potentials using quantum defects in diamond. *Proc. Natl. Acad. Sci.* **113**, 14133–14138 (2016).

234. Davis, H. C., Ramesh, P., Bhatnagar, A., Lee-Gosselin, A., Barry, J. F., Glenn, D. R., Walsworth, R. L. & Shapiro, M. G. Mapping the microscale origins of magnetic resonance image contrast with subcellular diamond magnetometry. *Nat. Commun.* **9**, 131 (2018).

235. Wahsner, J., Gale, E. M., Rodríguez-Rodríguez, A. & Caravan, P. Chemistry of MRI Contrast Agents: Current Challenges and New Frontiers. *Chem. Rev.* **119**, 957–1057 (2019).

236. Dadfar, S. M., Roemhild, K., Drude, N. I., von Stillfried, S., Knüchel, R., Kiessling, F. & Lammers, T. Iron oxide nanoparticles: Diagnostic, therapeutic and theranostic applications. *Adv. Drug Deliv. Rev.* **138**, 302–325 (2019).

237. Smith, B. R. & Gambhir, S. S. Nanomaterials for In Vivo Imaging. *Chem. Rev.* **117**, 901–986 (2017).

238. Waddington, D. E. J., Boele, T., Maschmeyer, R., Kuncic, Z. & Rosen, M. S. High-sensitivity in vivo contrast for ultra-low field magnetic resonance imaging using superparamagnetic iron oxide nanoparticles. *Sci. Adv.* **6**, eabb0998 (2020).

239. Goodwill, P. W., Saritas, E. U., Croft, L. R., Kim, T. N., Krishnan, K. M., Schaffer, D. V. & Conolly, S. M. X-Space MPI: Magnetic Nanoparticles for Safe Medical Imaging. *Adv. Mater.* **24**, 3870–3877 (2012).

240. Pouliquen, D., Le Jeune, J. J., Perdrisot, R., Ermias, A. & Jallet, P. Iron oxide nanoparticles for use as an MRI contrast agent: Pharmacokinetics and metabolism. *Magn. Reson. Imaging* **9**, 275–283 (1991).

241. Reimer, P., Müller, M., Marx, C., Wiedermann, D., Muller, R., Rummeny, E. J., Ebert, W., Shamsi, K. & Peters, P. E. T1 effects of a bolus-injectable superparamagnetic iron oxide, SH U 555 A: dependence on field strength and plasma concentration--preliminary clinical experience with dynamic T1-weighted MR imaging. *Radiology* (1998) doi:10.1148/radiology.209.3.9844683.

242. Zhang, H., Guo, Y., Jiao, J., Qiu, Y., Miao, Y., He, Y., Li, Z., Xia, C., Li, L., Cai, J., Xu, K., Liu, X., Zhang, C., Bay, B.-H., Song, S., Yang, Y., Peng, M., Wang, Y. & Fan, H. A hepatocyte-targeting nanoparticle for enhanced hepatobiliary magnetic resonance imaging. *Nat. Biomed. Eng.* **7**, 221–235 (2023).

243. Weissleder, R., Stark, D., Engelstad, B., Bacon, B., Compton, C., White, D., Jacobs, P. & Lewis, J. Superparamagnetic iron oxide: pharmacokinetics and toxicity. *Am. J. Roentgenol.* **152**, 167–173 (1989).

244. Chertok, B., Moffat, B. A., David, A. E., Yu, F., Bergemann, C., Ross, B. D. & Yang, V. C. Iron oxide nanoparticles as a drug delivery vehicle for MRI monitored magnetic targeting of brain tumors. *Biomaterials* **29**, 487–496 (2008).

245. Ferrucci, J. T. & Stark, D. D. Iron oxide-enhanced MR imaging of the liver and spleen: review of the first 5 years. *Am. J. Roentgenol.* **155**, 943–950 (1990).

246. Neuwelt, E. A., Várallyay, P., Bagó, A. G., Muldoon, L. L., Nesbit, G. & Nixon, R. Imaging of iron oxide nanoparticles by MR and light microscopy in patients with malignant brain tumours. *Neuropathol. Appl. Neurobiol.* **30**, 456–471 (2004).

247. Hai, A. & Jasanoff, A. Molecular fMRI. in *Brain Mapping* (ed. Toga, A. W.) 123–129 (Academic Press, Waltham, 2015). doi:10.1016/B978-0-12-397025-1.00013-0.

248. Lee, N., Yoo, D., Ling, D., Cho, M. H., Hyeon, T. & Cheon, J. Iron Oxide Based Nanoparticles for Multimodal Imaging and Magnetoresponsive Therapy. *Chem. Rev.* **115**, 10637–10689 (2015).

249. Ghosh, S., Harvey, P., Simon, J. C. & Jasanoff, A. Probing the brain with molecular fMRI. *Curr. Opin. Neurobiol.* **50**, 201–210 (2018).

250. Atanasijevic, T., Shusteff, M., Fam, P. & Jasanoff, A. Calcium-sensitive MRI contrast agents based on superparamagnetic iron oxide nanoparticles and calmodulin. *Proc. Natl. Acad. Sci.* **103**, 14707–14712 (2006).

251. Atanasijevic, T. & Jasanoff, A. Preparation of iron oxide-based calcium sensors for MRI. *Nat. Protoc.* **2**, 2582–2589 (2007).

252. Hsieh, V., Okada, S., Wei, H., García-Álvarez, I., Barandov, A., Alvarado, S. R., Ohlendorf, R., Fan, J., Ortega, A. & Jasanoff, A. Neurotransmitter-Responsive Nanosensors for T2-Weighted Magnetic Resonance Imaging. *J. Am. Chem. Soc.* **141**, 15751–15754 (2019).

253. Narain, R., Gonzales, M., Hoffman, A. S., Stayton, P. S. & Krishnan, K. M. Synthesis of Monodisperse Biotinylated p(NIPAAm)-Coated Iron Oxide Magnetic Nanoparticles and their Bioconjugation to Streptavidin. *Langmuir* **23**, 6299–6304 (2007).

254. Perez, J. M., Josephson, L., O'Loughlin, T., Högemann, D. & Weissleder, R. Magnetic relaxation switches capable of sensing molecular interactions. *Nat. Biotechnol.* **20**, 816–820 (2002).

255. Rodriguez, E., Lelyveld, V. S., Atanasijevic, T., Okada, S. & Jasanoff, A. Magnetic nanosensors optimized for rapid and reversible self-assembly. *Chem. Commun.* **50**, 3595–3598 (2014).

256. Chen, K. L., Mylon, S. E. & Elimelech, M. Enhanced Aggregation of Alginate-Coated Iron Oxide (Hematite) Nanoparticles in the Presence of Calcium, Strontium, and Barium Cations. *Langmuir* **23**, 5920–5928 (2007).

257. Zabow, G., Dodd, S. J. & Koretsky, A. P. Shape-changing magnetic assemblies as high-sensitivity NMR-readable nanoprobes. *Nature* **520**, 73–77 (2015).

258. Phillips, J., Glodowski, M., Gokhale, Y., Dwyer, M., Ashtiani, A. & Hai, A. Enhanced magnetic transduction of neuronal activity by nanofabricated inductors quantified via finite element analysis. *J. Neural Eng.* **19**, (2022).

259. Bricault, S., Barandov, A., Harvey, P., DeTienne, E., Hai, A. & Jasanoff, A. Image-guided neural activity manipulation with a paramagnetic drug. *Nat. Commun.* **11**, 136 (2020).

260. Muller, R. N., Gillis, P., Moiny, F. & Roch, A. Transverse relaxivity of particulate MRI contrast media: from theories to experiments. *Magn. Reson. Med.* **22**, 178–182; discussion 195-196 (1991).

261. Brooks, R. A., Moiny, F. & Gillis, P. On T2-shortening by weakly magnetized particles: the chemical exchange model. *Magn. Reson. Med.* **45**, 1014–1020 (2001).

262. Brooks, R. A. T(2)-shortening by strongly magnetized spheres: a chemical exchange model. *Magn. Reson. Med.* **47**, 388–391 (2002).

263. Gillis, P., Moiny, F. & Brooks, R. A. On T(2)-shortening by strongly magnetized spheres: a partial refocusing model. *Magn. Reson. Med.* **47**, 257–263 (2002).

264. Matsumoto, Y. & Jasanoff, A. T2 relaxation induced by clusters of superparamagnetic nanoparticles: Monte Carlo simulations. *Magn. Reson. Imaging* **26**, 994–998 (2008).

265. Jensen, J. H. & Chandra, R. Strong field behavior of the NMR signal from magnetically heterogeneous tissues. *Magn. Reson. Med.* **43**, 226–236 (2000).

266. Yablonskiy, D. A. & Haacke, E. M. Theory of NMR signal behavior in magnetically inhomogeneous tissues: the static dephasing regime. *Magn. Reson. Med.* **32**, 749–763 (1994).

267. Sun, N., Chen, D.-X., Gu, H.-C. & Wang, X.-L. Experimental study on T2 relaxation time of protons in water suspensions of iron-oxide nanoparticles: Waiting time dependence. *J. Magn. Magn. Mater.* **321**, 2971–2975 (2009).

268. Choo, E. S. G., Tang, X., Sheng, Y., Shuter, B. & Xue, J. Controlled loading of superparamagnetic nanoparticles in fluorescent nanogels as effective T2-weighted MRI contrast agents. *J. Mater. Chem.* **21**, 2310–2319 (2011).

269. Chen, D.-X., Xu, F.-J. & Gu, H.-C. Experimental study on transverse relaxation rate of protons in water suspensions of magnetite nanoclusters: Dependence of cluster sizes, volume fraction, inter-echo time, and waiting time. *J. Magn. Magn. Mater.* **324**, 2809–2820 (2012).

270. Peng, E., Wang, F., Zheng, B., Li, S. F. Y. & Xue, J. M. Engineered water-soluble two-dimensional magnetic nanocomposites: towards highly magnetic relaxometric properties. *Nanoscale* **7**, 7819–7832 (2015).

271. Zhou, Z., Tian, R., Wang, Z., Yang, Z., Liu, Y., Liu, G., Wang, R., Gao, J., Song, J., Nie, L. & Chen, X. Artificial local magnetic field inhomogeneity enhances T2 relaxivity. *Nat. Commun.* **8**, 15468 (2017).

272. Großmann, R., Peruani, F. & Bär, M. A geometric approach to self-propelled motion in isotropic & anisotropic environments. *Eur. Phys. J. Spec. Top.* **224**, 1377–1394 (2015).

273. Wei, H., Bruns, O. T., Kaul, M. G., Hansen, E. C., Barch, M., Wiśniowska, A., Chen, O., Chen, Y., Li, N., Okada, S., Cordero, J. M., Heine, M., Farrar, C. T., Montana, D. M., Adam, G., Ittrich, H., Jasanoff, A., Nielsen, P. & Bawendi, M. G. Exceedingly small iron oxide nanoparticles as positive MRI contrast agents. *Proc. Natl. Acad. Sci.* **114**, 2325–2330 (2017).

274. Kim, B. H., Lee, N., Kim, H., An, K., Park, Y. I., Choi, Y., Shin, K., Lee, Y., Kwon, S. G., Na, H. B., Park, J.-G., Ahn, T.-Y., Kim, Y.-W., Moon, W. K., Choi, S. H. & Hyeon, T. Large-Scale Synthesis of Uniform and Extremely Small-Sized Iron Oxide Nanoparticles for High-Resolution T1 Magnetic Resonance Imaging Contrast Agents. *J. Am. Chem. Soc.* **133**, 12624–12631 (2011).

275. Ludwig, F., Eberbeck, D., Löwa, N., Steinhoff, U., Wawrzik, T., Schilling, M. & Trahms, L. Characterization of magnetic nanoparticle systems with respect to their magnetic particle imaging performance. *Biomed. Tech. Eng.* **58**, 535–545 (2013).

276. Camarneiro, F., Bocquel, J., Gallo, J., Bañobre-López, M., Berg-Sørensen, K., Andersen, U. L., Huck, A. & Nieder, J. B. Magnetic Field Mapping Around Individual Magnetic Nanoparticle Agglomerates Using Nitrogen-Vacancy Centers in Diamond. *Part. Part. Syst. Charact.* **38**, 2100011 (2021).

277. Yu, Q., Zhang, Y.-M., Liu, Y.-H., Xu, X. & Liu, Y. Magnetism and photo dual-controlled supramolecular assembly for suppression of tumor invasion and metastasis. *Sci. Adv.* **4**, eaat2297 (2018).

Appendix 1: Supplementary Table and Figures

Table 3: Detailed statistical parameters of ANOVA analysis of in silico neuronal morphologies

Compartment (Type)	F	n (total)	p
Aggregate	24.5	4	7.90429×10^{-16}
(MTG3)		10452	
(MTG6)		3399	
(FLL3)		8505	
(MFG3)		11291	
Soma	1.73	4	0.21473
(MTG3)		4	
(MTG6)		4	
(FLL3)		4	
(MFG3)		4	
Axon	1.06	4	0.40931
(MTG3)		3	
(MTG6)		4	
(FLL3)		3	
(MFG3)		4	
Dendrite	5.11	4	0.01655
(MTG3)		4	
(MTG6)		4	

(FLL3)	4
(MFG3)	4

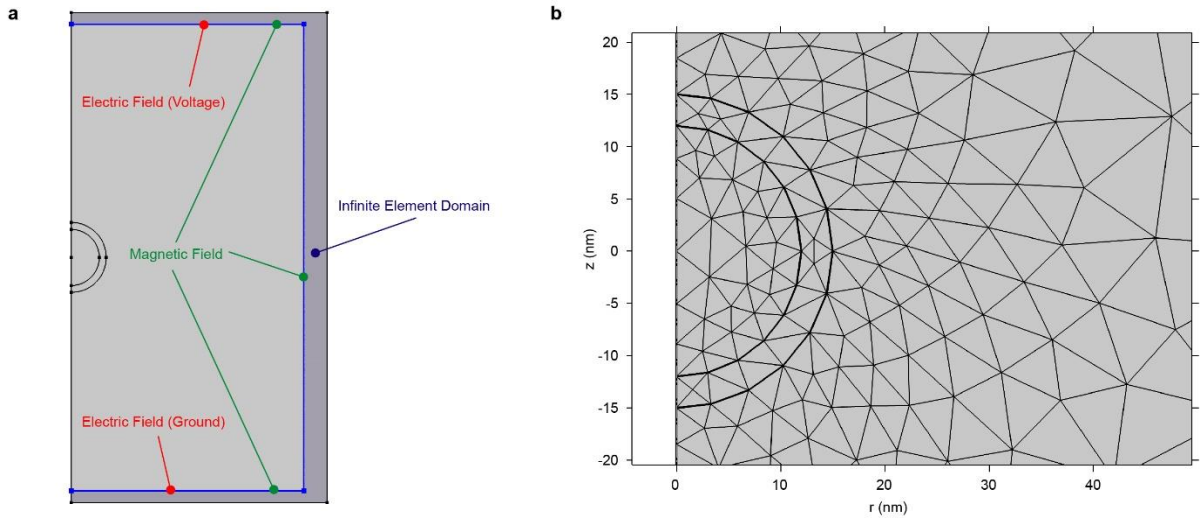

Figure 14: Boundary/domain conditions and mesh placement in COMSOL Multiphysics.

(a) Grounding the bottom boundary of the domain and applying voltage to the top boundary allows for electric field creation (red.) Application of a magnetic field intensity boundary condition (green.) Infinite element domain application to the outer shell (blue.) (b) Model meshing arrangement used ("normal" density).

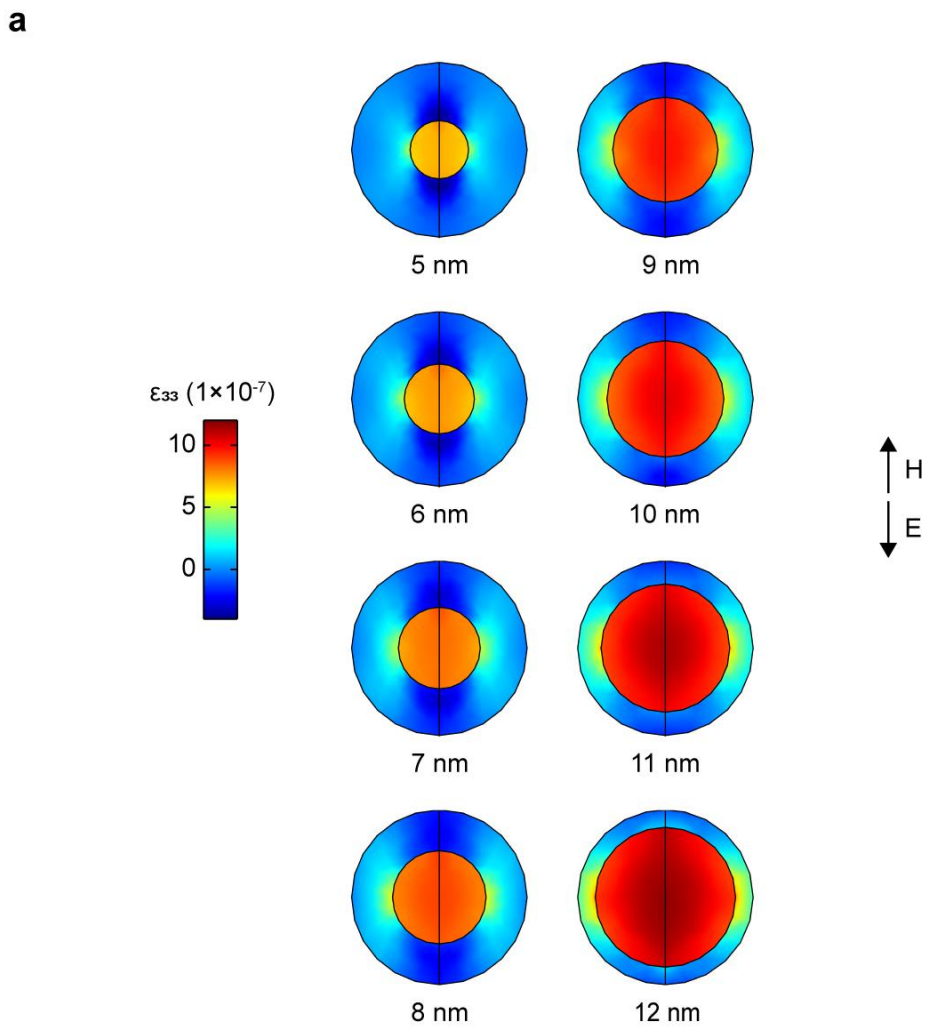

Figure 15: Effect of MENPs core size on internal strain.

(a) The effect of core size on the 33 component of strain (colormap). Core radius ranged from 5 to 12 nm corresponding to shell thickness ranging from 10 to 3 nm. In all cases, E_z = -100 mV/mm antiparallel to H_z = 4 kA/m.

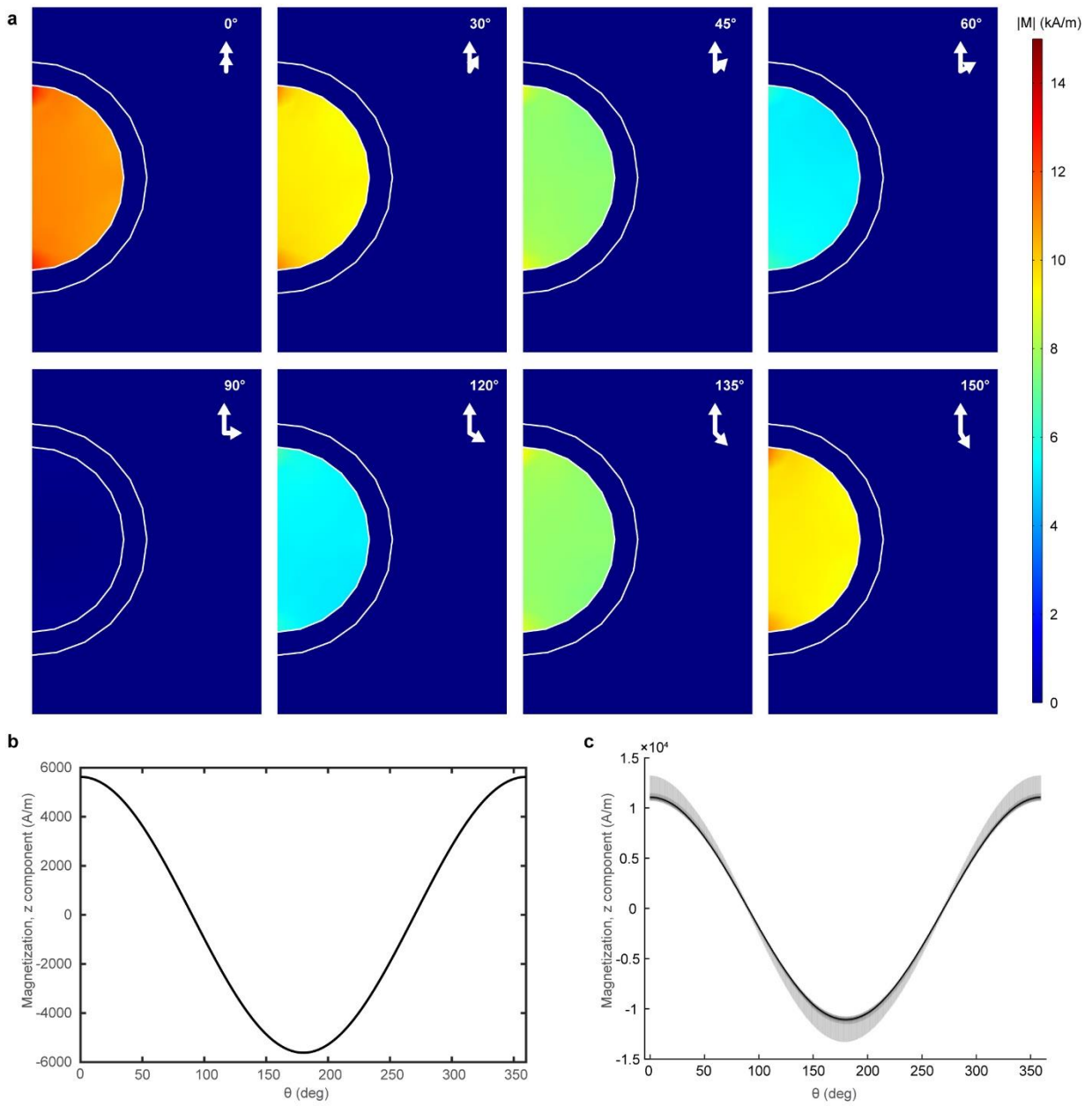

Figure 16: Effect on magnetization of electric field and magnetic field intensity relative direction.

(a) Magnetization norm plots for {0°, 30°, 45°, 60°, 90°, 120°, 135°, 150°} magnetic field rotation. (b) Magnetization average z-component plot versus application angle. (c) Magnetization decile plot; deciles plotted are (0-100), (10-90), (20-80), (30-70), (40-60), and the mean (50^{th} percentile).

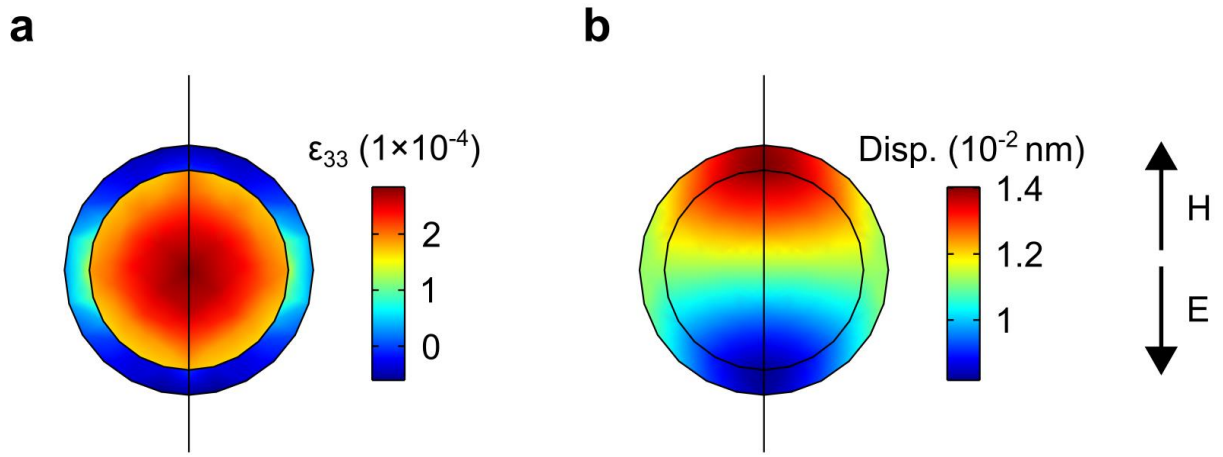

Figure 17: Nanoparticle strain and displacement at high fields comparable to extant literature on magnetoelectric composites.

(a) The 33 component of strain (unitless, 10^{-4}) and (b) displacement (nanometers, 10^{-2}) at E_z = -10 kV/cm antiparallel to Hz = 1 kOe (approximately 80 kA/m).

Disp. = displacement

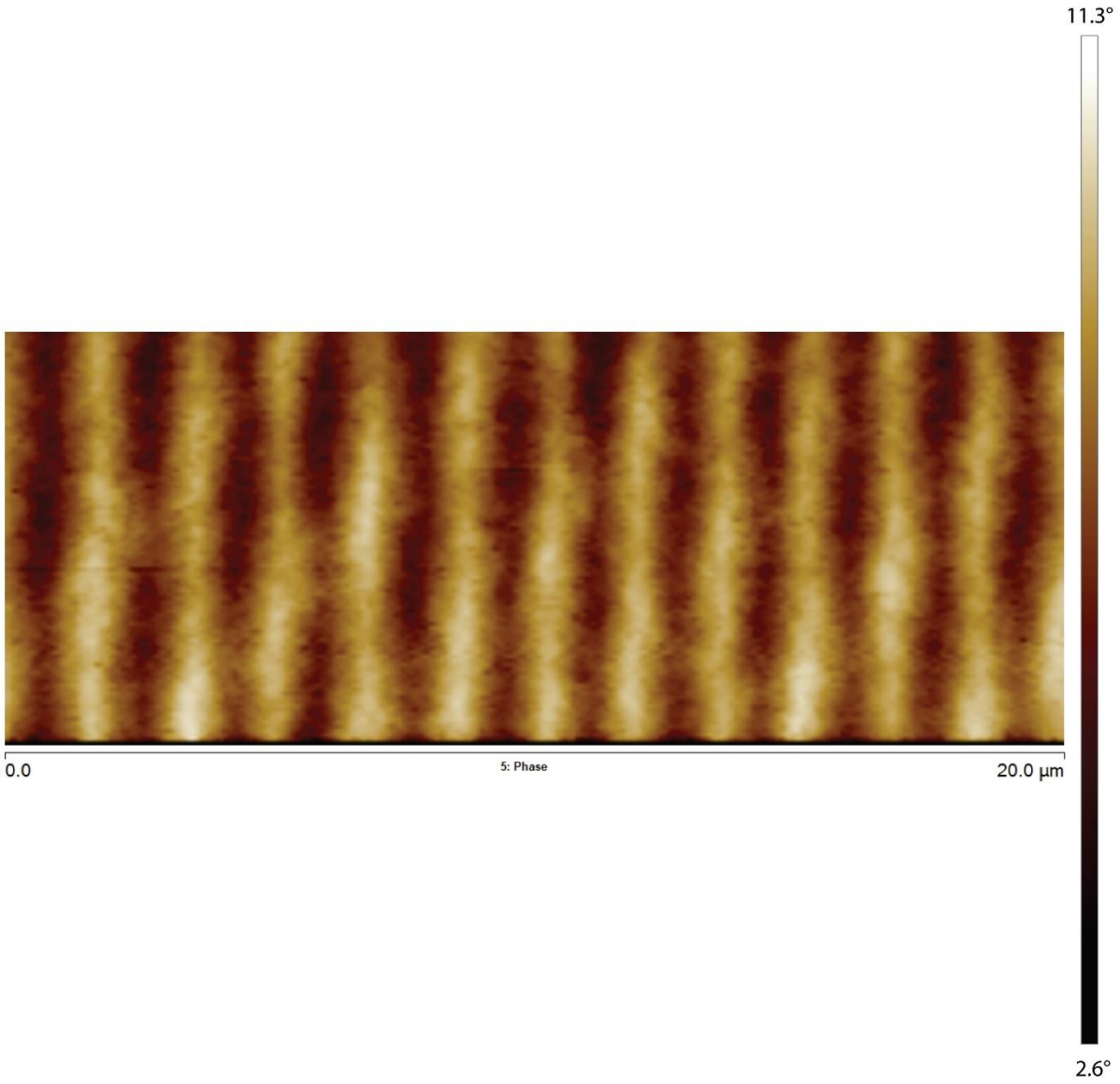

Figure 18: Nanoparticle strain and displacement at high fields comparable to extant literature on magnetoelectric composites.

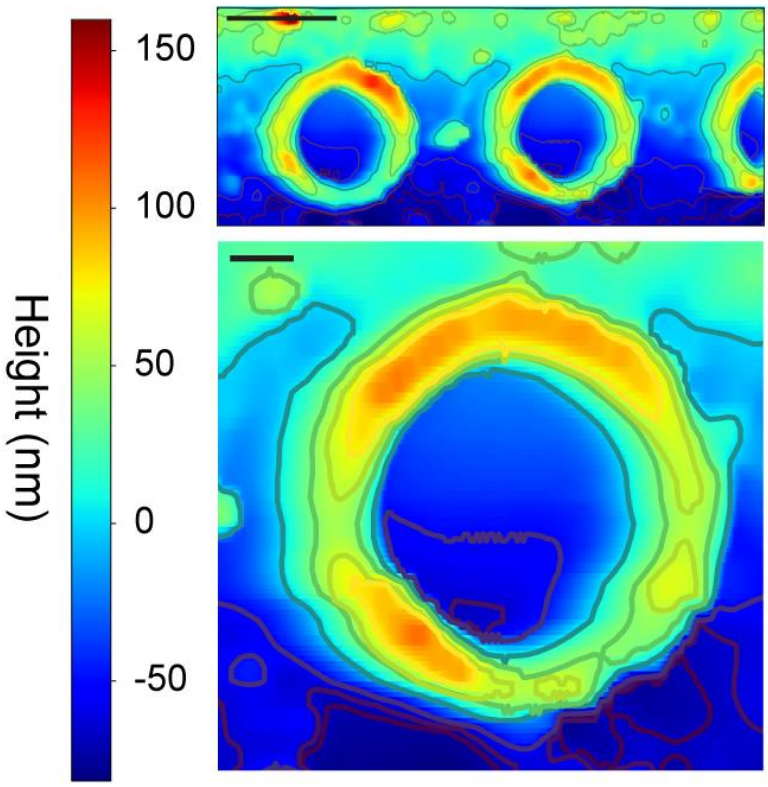

Figure 19: Atomic force microscopy scans of barium titanate rings.

Scale bars = 1 µm (upper), 100 nm (lower).

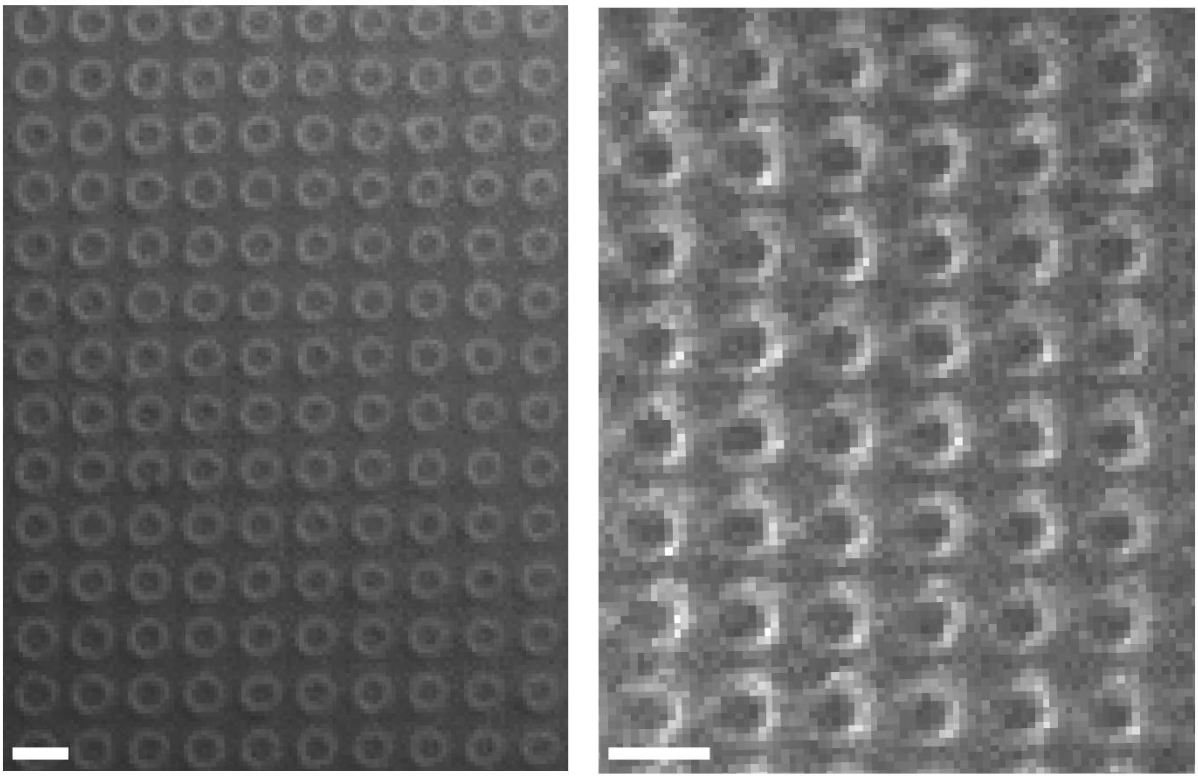

Figure 20: Optical images of barium titanate (non-magnetoelectric) and barium-titanate / cobalt ferrite (magnetoelectric) rings.

Scale bar = 2 μm.

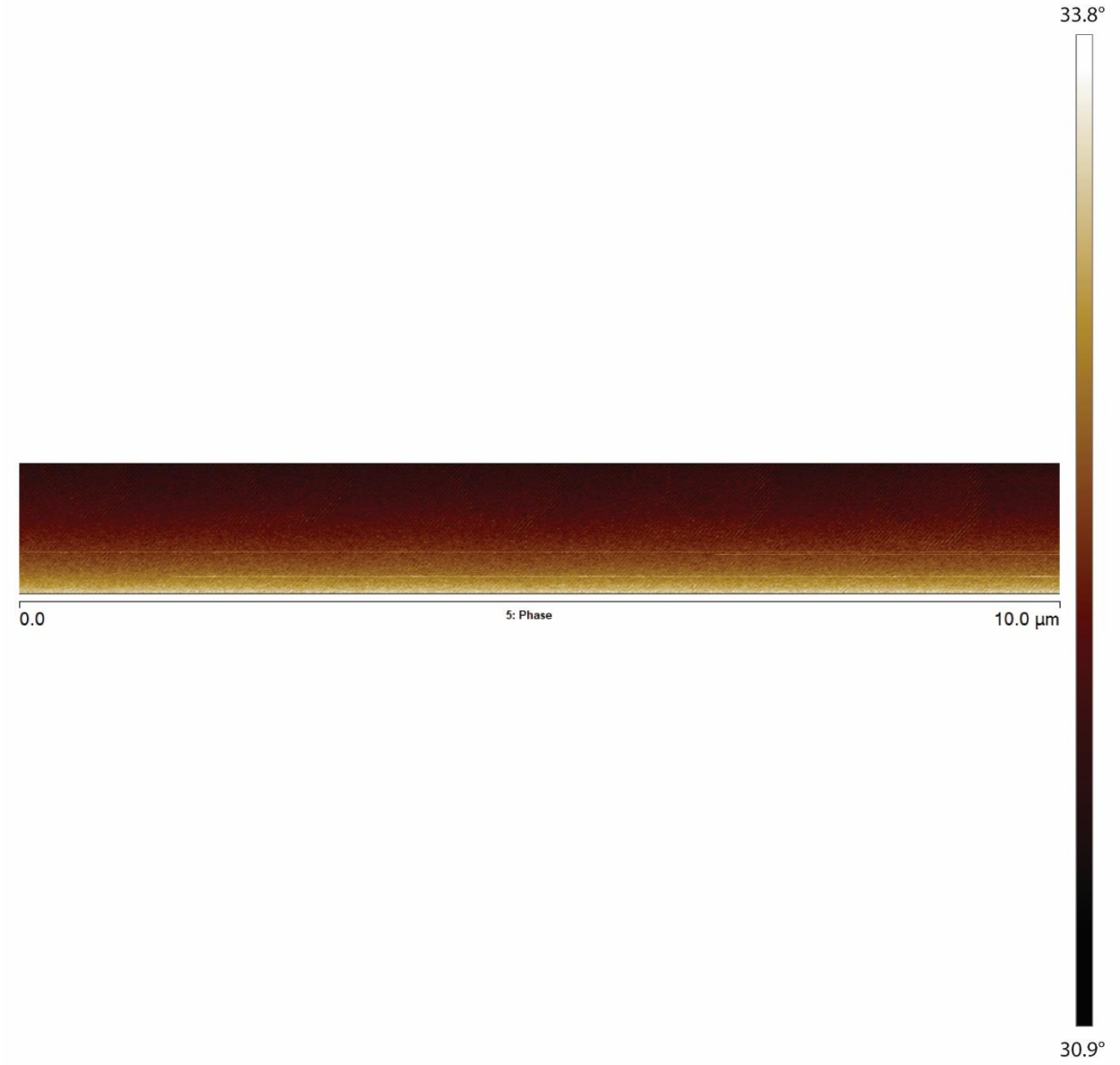

Figure 21: Magnetic force microscopy phase of barium titanate (non-magnetoelectric) rings.

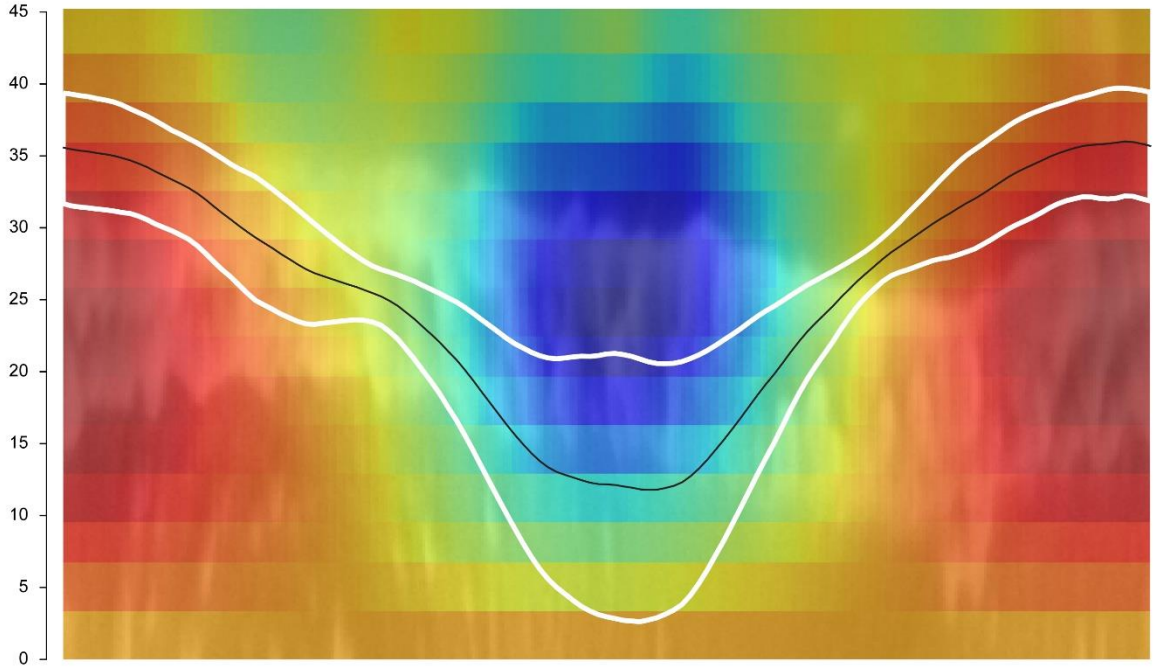

Figure 22: Radially unwrapped dipole from a single nanoring.

Anisotropy line plot of radially unwrapped overlaid magnetic force microscopy and scanning electron microscopy images, with y-axis labels corresponding to line graph of mean (black line) and standard deviation (white lines) with respect to angle.

Appendix 2: Code Snippets

2.1: Single Neuronal Morphology Magnetization Analysis

https://github.com/hailab-uw/Bok2022InSilicoEP

```
'''
QuantifyMag_MPIvoxel_Pyr.py
Description: Runs a biophysical simulation on Allen Brain Atlas morphologies to
             compute surrounding voxel-based magnetization.
Usage: Download and patch desired morphologies from ABA, then run the batch file
`loopMorphoPyr.bat`
Author(s): Ilhan Bok, Xiaofei Qu
Last Modified: Jan. 19, 2022
'''

import numpy as np
import sys
import matplotlib.pyplot as plt
import LFPy
import neuron
import math

def rndu(x, delta):
    return int(math.ceil(x / delta)) * delta

def rndd(x, delta):
    return int(math.floor(x / delta)) * delta

def rnd(x, delta):
    return int(round(x / delta)) * delta

#compile mod files every time, because of incompatibility with Mainen96 files:
neuron.nrn_dll_loaded.append('nrnmech.dll')

cellname = sys.argv[1]
# define cell parameters used as input to cell-class
cellParameters = {
   'morphology'    : cellname + '.asc',
    'templatefile'  : ['templatePyr.hoc',
                       ],
    'templatename'  : 'cADpyr231_L6_TPC_L4_0cb1e9aa6b',
    'templateargs'  : cellname,
    'passive' : False,
    'nsegs_method' : None,
    'dt' : 2**-6,
    'tstart' : 0,
    'tstop' : 50,
    'v_init' : -60,
```

```
    'celsius': 34,
    'pt3d' : True,
}
# delete old sections from NEURON namespace
LFPy.cell.neuron.h("forall delete_section()")

# Initialize cell instance, using the LFPy.Cell class
cell = LFPy.TemplateCell(**cellParameters)
cell.set_rotation(x=4.729, y=-3.166, z=0)

# Override passive reversal potential, AP is generated
for sec in cell.allseclist:
    for seg in sec:
        seg.e_pas = 100

# Interval for recording electrode placement
delta = 20
num_radii = 1
cellx = cell.x.flatten()
celly = cell.y.flatten()
cellz = cell.z.flatten()

xmid = rnd((rndd(min(cellx),delta)-2*delta + rndu(max(cellx),delta)+2*delta)/2,delta)
xmin = rndd(min(cellx),delta)-2*delta
xmax = rndu(max(cellx),delta)+2*delta+1
ymin = rndd(min(celly),delta)-2*delta
ymax = rndu(max(celly),delta)+2*delta+1
zmin = rndd(min(cellz),delta)-2*delta
zmax = rndu(max(cellz),delta)+2*delta+1

# Generate the grid in xz-plane over which we calculate local field potentials
X, Y, Z = np.mgrid[xmin:xmax:delta,
                   ymin:ymax:delta,
                   zmin:zmax:delta]

# Print minimum and maximum x, y, and z for scaling by MATLAB
f = open('CellSizes.out', 'a')
f.write(str(cellname) + ' ' + str(xmin) + ' ' + str(xmax) + ' ' + str(ymin) + ' ' +
str(ymax)
    + ' ' + str(zmin) + ' ' + str(zmax) + '\n')
f.close()

# define parameters for extracellular recording electrode, using optional method
electrodeParameters = {
    'sigma' : 0.3,          # extracellular conductivity
    'x' : X.flatten(),      # x,y,z-coordinates of contacts
    'y' : Y.flatten(),
    'z' : Z.flatten(),
    'method' : 'root_as_point',  #sphere source soma segment
    'N' : np.array([[0, 1, 0]]*X.size), #surface normals
    'r' : 2.5,              # contact site radius
    'n' : 20,               # datapoints for averaging
}
```

```
# create extracellular electrode object for LFPs on grid
electrode = LFPy.RecExtElectrode(cell=cell, **electrodeParameters)

# perform NEURON simulation
# Simulated results saved as attribute `data` in the RecExtElectrode instance
cell.simulate(probes=[electrode])

from example_suppl_2D import plot_cell, plot_mag_dist, plot_mag_dist_branch,
plot_mag_voxel, find_tshow_global
t_show_global = find_tshow_global(cell) # note that this is for times less than 20 ms
(to filter out saturation)

# Create magnetization voxel plots
vector_str = 'XYZ' '''Include static field directions in {X,Y,Z} to compute the
results for'''
for currdir in vector_str:
    print('Computing for ' + currdir)
    dirvec = (1,0,0)
    # Map direction to vector
    if currdir == "Y":
        dirvec = (0,1,0)
    elif currdir == "Z":
        dirvec = (0,0,1)
    fig = plot_mag_voxel(cell, electrode, X, Y, Z, t_show_global, dirvec, xmin, xmax,
zmin, zmax)
    fig.savefig('PYR_LFPy(' + cellname + ')' + currdir + '.svg', dpi=350)
    mag_dict = plot_mag_dist(cell, electrode, X, Y, Z, t_show_global,dirvec,
                    list(range(xmin,xmax,delta)),
                    list(range(ymin,ymax,delta)),
                    list(range(zmin,zmax,delta)))
    f = open( 'PYR_VAR_QuantifyMagDist(' + cellname + ')' + currdir + '.out', 'w')
    f.write(repr(mag_dict))
    f.close()
```

2.2: Iron oxide nanocluster R2 extraction code

https://github.com/hailab-uw/2D_SPIO_R2

```
import numpy as np
import matplotlib.pyplot as plt
import matplotlib.image

import imageio

import matplotlib as mpl
import matplotlib.pyplot as plt
from scipy.stats import f_oneway, ttest_ind, norm
from scipy.ndimage import gaussian_filter
from scipy.interpolate import lagrange

from PIL import Image

import statistics
import numpy as np

import math

# Returns the value corresponding to x for a Normal
# distribution with mean mu and standard deviation sig
def gaussian(x, mu, sig):
    return 1./(np.sqrt(2.*np.pi)*sig)*np.exp(-np.power((x - mu)/sig, 2.)/2)

sq = np.array(Image.open("./cluster_tiff.tif"))
plt.imshow(sq, cmap='gray')
plt.show()

matplotlib.image.imsave('inverse_squared.png', sq, cmap='gray')

# Sample of background noise from the same MRI scan
# the array may be any size but larger samples of noise
# yield better results
background_sample = np.load('Background_Sample.npy')

print('Attempting R2 Quantification...')
counts, bins, _ = plt.hist(background_sample, bins=100, density=1)

# Display the result of Gaussian/Normal fitting the background noise
muo, sigma = norm.fit(background_sample)
best_fit_line = norm.pdf(bins,muo,sigma)
plt.plot(bins, best_fit_line)
plt.show()

# Fade colors between different mu values to ensure
# distinguishabilty
def colorFader(c1,c2,mix=0): #fade (linear interpolate) from color c1 (at mix=0) to
c2 (mix=1)
```

```
    c1=np.array(mpl.colors.to_rgb(c1))
    c2=np.array(mpl.colors.to_rgb(c2))
    return mpl.colors.to_hex((1-mix)*c1 + mix*c2)

c1='red'
c2='blue'

S1_arr = []
S2_arr = []
S3_arr = []
S4_arr = []
S5_arr = []

sweep_range = 5

for mu in range(int(muo)-sweep_range,int(muo)+sweep_range):
    v10x_S1_diff = []
    v10x_S2_diff = []
    v10x_S3_diff = []
    v10x_S4_diff = []

    v10x_S1_Maxes = sq
    maxgauss = gaussian(mu,mu,sigma)
    v10x_S1_Maxes[v10x_S1_Maxes > mu] = mu

    res_S1 = (maxgauss-gaussian(v10x_S1_Maxes,mu,sigma))/maxgauss

    for i in range(len(v10x_S1_Maxes)):
        v10x_S1_diff.append(v10x_S1_Maxes[i]*res_S1[i])

    abcd = np.array(gaussian_filter(v10x_S1_diff,1))# was 2
    asdf = 1/np.log(abcd)

    # Diffusion coefficient in m^2/s
    D = 2.5e-9*3

    # Use these indices to select the regions of the image
    # for sampling of each condition
    C3 = [asdf[18:20,10:12]]
    C2 = [asdf[18:20,7:9]]
    C1 = [asdf[18:20,5:7]]
    C3 = np.array(C3).flatten()
    C2 = np.array(C2).flatten()
    C1 = np.array(C1).flatten()

    # Diffusion time constant in milliseconds
    TD = np.multiply([((25e-9)**2/D),((50e-9)**2/D),((100e-9)**2/D)],1000)
    R2 = np.log([(np.mean(C1)),(np.mean(C2)),(np.mean(C3))])

    plt.plot(TD,R2,color=colorFader(c1,c2,(mu-(int(muo)-500))/1000))

    S1_arr.append(np.mean(C1))
    S2_arr.append(np.mean(C2))
    S3_arr.append(np.mean(C3))
```

```
print('TD:')
print(TD)
print('R2:')
print(R2)
plt.xscale('log')
plt.show()
```

Appendix 3: Direct Observation of Nuclear Magnetic Resonance Transverse Relaxation in Nanopatterned Clusters of Iron Oxide Particles

Ilhan Bok, Beth Rauch, Alireza Ashtiani, Aviad Hai

Magn Reson Med. 2024 Feb;91(2):687-698. doi: 10.1002/mrm.29898. Epub 2023 Oct 23.

Abstract

PURPOSE: We aim to verify predictions showing T2 relaxation rate of nanoparticle clusters and its dependence on spacing, size, geometry, and pulse sequence.

METHODS: We performed a laboratory validation study using nanopatterned arrays of iron oxide nanoparticles to precisely control cluster geometry and image diverse samples using a 4.7T MRI scanner with a *T2*-weighted Fast Spin-Echo Multi Slice sequence. We applied denoising and normalization to regions of interest and estimated relative *R2* for each relevant nanoparticle array or nanocluster array. We determined significance using an unpaired two-tailed t-test or one-way ANOVA and performed curve fitting.

RESULTS: We measure a density-dependent *T2* effect ($p = 8.9976 \times 10^{-20}$, one-way ANOVA) and insignificant effect of cluster anisotropy ($p = 0.5924$, unpaired t-test) on *T2* relaxation. We find negative quadratic relationships $(-0.0045(\log \tau_D)^2 - 0.0655(\log \tau_D) - 2.7800)$ for single nanoparticles of varying sizes and for clusters $(-0.0045(\log \tau_D)^2 - 0.0827(\log \tau_D) - 2.3249)$ for diffusional correlation time $\tau_D = r_p^2/D$. Clusters show positive quadratic relationships for large

(3.8615×10^{-6} $(d_{pp}/r_p)^2$ - 9.3853×10^{-5} (d_{pp}/r_p) - 2.0393) and exponential relationships for small (-2.0050$(d_{pp}/r_p)^{0.0010}$) clusters. Calculated *R2* peak values also align well with in silico predictions (7.85×10^{-4} msec compared to 1.47×10^{-4} msec, 4.23×10^{-4} msec, and 5.02×10^{-4} msec for single iron oxide nanoparticles, 7.88×10^{-4} msec compared to 5.24×10^{-4} msec for nanoparticle clusters).

CONCLUSION: Our verification affirms longstanding in silico predictions and demonstrates aggregation-dependent behavior in agreement with previous Monte Carlo simulation studies.

Introduction

T2 relaxation in magnetic resonance imaging (MRI) and readouts from other recently evolving imaging modalities such as magnetic particle imaging (MPI)[7, 44] and optically detected magnetic resonance (ODMR)[233, 234], are all modulated by multiplexed, concentration-dependent features of magnetic tracers, sensors, and substrates[44, 234, 235]. In clinical setting, superparamagnetic iron oxide nanoparticles (SPIONs) can specifically serve as the agent of choice for tissue contrast enhancement[236–238] and perfusion-dependent structural readouts[237–239]. SPIONs usually act as purely passive isotropic injectable agents, demonstrating an inherent ability to accumulate in different tissue types. Examples include hepatic lumen cells[240–242], splenic red pulp cells[240, 243], gliosarcoma[244], and many more[235]. These provide powerful diagnostic tools for detecting structural and tissue manifestations of pathologies such as cirrhosis[240], liver cancer[240, 241], spleen cancer[245], and brain disorders[246]. In addition to static image contrast enhancement, newly emerging responsive SPION-based sensors rely on specialized chemical coating to enable dynamic functional readouts of biophysical and biochemical components[247–249]. Examples include SPIONs conjugated with calmodulin and its target peptides[250, 251] or C2 domains of synaptotagmin[121] as calcium responsive MRI

contrast agents; engineered monoaminergic binding peptide domains for sensing neurotransmitters[252], and more[253–256]. Moreover, other types of injectable nanoparticles, nanostructures and molecular probes offer aggregation-based sensing and modulation of electric fields[257, 16, 56, 207, 258] and biochemical processes[27, 29, 259] with particular uses in neuroscience and neurology. The spatial distribution and related aggregation attributes of magnetic particles are important to both static and dynamic contrast enhancement, as the final scaling factor, arrangement, and distribution of tracers can impact image quality, contrast, signal-to-noise ratio, and sensitivity to analytes. This highlights the importance of precise prediction of SPION aggregation and corresponding MRI signal changes accompanying their nanoscale spatial organization.

Theoretical predictions of changes in relaxation rate (*R2*) due to SPION aggregation reveal a dependence on particle size, geometry, and anisotropy[260–264]. Random walk simulations of water molecules diffusing in proximity to SPIONs suggest these nonlinearities also depend on scan parameters[263, 264]. Specifically, spin phase dispersion surrounding small nanoparticles are governed by classic outer sphere theory[260] in what is termed simple motional averaging regime (MAR). This effect plateaus and decreases for larger nanoparticles using spin echo pulse sequences with large enough echo time (*TE*) in what is termed the slow motion regime (SMR)[265]. For single nanoparticles of radius r_p in medium with self-diffusion constant (D), the transition between these two regimes is represented by the diffusional correlation time ($\tau_D = r_p^2/D$) and is predicted to occur at a point inversely proportional to the angular frequency shift at the particle surface ($\Delta\omega_r$)[266]. More recent models attempt to describe this relationship for clustered SPIONs in the context of aggregation-based MRI sensing[264] reporting peak *R2* transition value between MAR and SMR of 85.59 s^{-1} at $\tau_D = 5.02 \times 10^{-4}$ msec for single particles/dots and 87.31 s^{-1} at $\tau_D = 5.24 \times$

10^{-4} msec for three-dimensional isotropic clusters. Chemical exchange models of diffusion[261] demonstrated comparable peak *R2* value of 0.45 s^{-1} for echo spacing τ_{CP} = 0.5 msec and $\Delta\omega_r$ = 472 rad/s, at τ_D = 0.15 msec (τ_D/τ_{CP} = 1.97) with a volume fraction (v) of 0.005: normalizing by v yields $\tau_D = 1.47 \times 10^{-4}$. The chemical exchange model posits that water molecules either diffuse past iron oxide nanoparticles ("outer sphere") or contact and bind them ("inner sphere") and that flux between these two states influences diffusion-related *T2* relaxation behavior. A number of measurements have supported these studies indirectly[267–271] but a piecewise ground-truth experimental validation of this effect has not yet been performed.

Here we use precise nano-scale lithography of SPION clusters to provide direct experimental observation of the concept of significant alterations in *R2* due to aggregation. By extracting *R2* values from MRI measurements of nanofabricated arrays of SPION clusters, we demonstrate peak diffusion time correlating with model predictions, with peak τ_D measured at 7.85×10^{-4} msec for single particles. Peak τ_D for isotropic two-dimensional clusters was 7.88×10^{-4} msec and similarly correlated. Our results present a first validation and agreement with long standing theoretical predictions of the behavior of iron oxide nanoparticles and provide a novel protocol with broad implications on the analyses and development of MRI contrast agents and aggregation-based sensors and modulators.

Methods

Finite Element Analyses of Magnetic Fields

Magnetic field profiles of SPION clusters were simulated using COMSOL Multiphysics 6.0 (COMSOL Inc., Stockholm, Sweden). The *Magnetic Fields* (*mf*) module was used to emulate nanoparticle arrays under a 4.7T B_0 bias field applied along the y direction within a hexagonal

simulation arena with periodic boundary condition. The *Ampere's Law* boundary condition with a *B-H curve* magnetization model was applied on low carbon steel magnetite particles (COMSOL Materials Library) surrounded by cerebrospinal fluid (relative electrical permittivity ε_r = 81.2, electrical conductivity σ = 4.8 S/m). A *Job Configurations* node was used to perform a parametric sweep of interparticle distance (d_{pp}) to particle radius (r_p) ratio (d_{pp}/r_p) ranging from three to 40 in 0.1 increments. The resultant magnetic field values were processed using Python 3.7 as follows: values were weighted by mesh element size within a region of radius ½*d_{pp} at the center, left, or right region of the nanoparticle cluster, and an origin-centered circle with radius 2*d_{pp} was used to define the field of view of the cluster. Statistical traces were further processed and visualized using MATLAB R2022a (MathWorks, Inc. Natick, MA, USA). A moving average centered between the current and previous elements with a sliding window of 4 frames was used to smooth the mean and standard deviation for all field traces against d_{pp}/r_p. Averages were truncated at endpoints where there were not enough elements to fill the moving mean window.

Nanostructure Fabrication

We used electron beam nanolithography to create nanopatterned iron oxide arrays (Fig. 23a). A silicon N-type phosphorus doped <100> 1-10 Ω·cm 380 μm single-side polished wafer (UniversityWafer, Boston, MA, USA, Cat. Number 695) was spin-coated with poly methyl-methacrylate (PMMA) 495 A4 photoresist (Kayaku Advanced Materials Inc., Westborough, MA, USA) at 4000 rpm for 45 sec. After verifying a film thickness of 185 nm (F20 Reflectometer, Filmetrics, Inc., San Diego, CA, USA), the wafer sample was baked on a hotplate at 180 °C for 90 sec. The baked wafer was diced into 10 mm × 10 mm chips and patterned using an Elionix ELS G-100 electron beam lithography system (Elionix Inc., Tokyo, Japan) using the parameters shown in Table 4. Samples were developed at room temperature in 1:3 methyl isobutyl ketone (Thermo

Fisher Scientific Inc., Waltham, MA, USA, Cat. Number M2131):isopropanol (MIBK:IPA) for 60 sec and rinsed first with IPA, then with deionized (DI) water. After inspecting the consistency of developed samples (Supplementary Fig. S2.1) using a Zeiss LEO 1530-1 field emission scanning electron microscope (Carl Zeiss AG, Oberkochen, Germany) a custom-built electron beam metal evaporator was used to deposit a 30 nm layer of iron oxide at 0.2 Å/sec at room temperature (~20 °C) and relative humidity of 23% or less. Samples were lifted off in room temperature acetone with gentle agitation to prevent re-adhesion of iron. Completed samples were rinsed first with IPA, then with DI water. Structures were visually inspected for cleanliness and consistency after each processing step using an Olympus BX51WI Upright Fluorescent Microscope (Olympus Corporation, Tokyo, Japan).

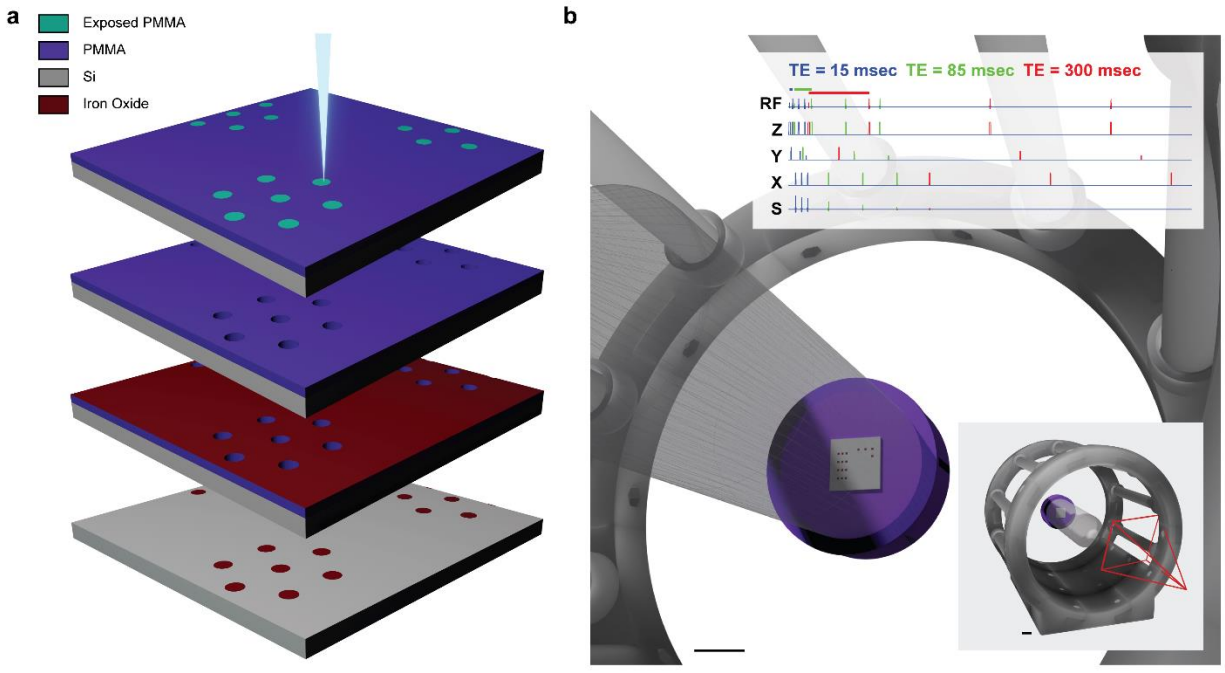

Figure 23: Iron oxide nanoparticle cluster fabrication and MR scan schematic.

(a, from top to bottom) A layer of poly methyl-methacrylate is spin-coated onto a silicon substrate and patterned using electron beam lithography. The layer is then developed using a 1:3 mixture of methyl isobutyl ketone : isopropanol, coated with an ultra-thin layer of iron oxide using electron beam metal evaporation, then lifted off using room-temperature acetone with gentle agitation. (b) A scanning procedure schematic showing the iron oxide chip attached to the inside of a conical tube, placed into a birdcage coil (scale bar = 10 mm), and scanned using multi-slice fast spin echo (upper right) with variable echo time. Values from 15 msec to 300 msec in 15 msec increments were recorded. An image using an echo time of 85 msec was chosen for further analysis (see Fig. 4). The full configuration is shown on the bottom right, with the perspective seen in the full panel shown as a red prism (scale bar = 10 mm).

Fast Spin-Echo Multi Slice MRI T2 Scans

Nanofabricated samples were epoxied (R.S. Hughes Co., Inc., Sunnyvale, CA, USA, Cat. Number 078143-14210) with the patterned side facing up on a cylindrical high density polyethylene surface (radius 10 mm, height 10 mm), which was itself epoxied into a 50 mL centrifuge tube cap, and the entire phantom tube was filled with reagent-grade DI water. Images were acquired using fast spin-echo multi-slice *T2*-weighted scans (Table 5) on an Agilent 4.7T horizontal bore MRI/MRS system housing a 72 mm inner diameter Agilent/Varian #S190888200 108/38 1H 200 MHz Quad Birdcage volume coil (Varian Medical Systems, Inc., Palo Alto, CA, USA) (see Fig. 23b). For density-dependent and anisotropy-dependent samples (see Fig. 24), we used TE = 68 msec, TR = 4000 msec, and a voxel size of 78.1 μm × 79.4 μm with a slice thickness of 700 μm and N = 10 averages. For arrays of varying nanoparticle size and nanoparticle clusters, scans used TE = 85 msec, TR = 5000 msec, and a voxel size of 70.3 μm × 71.4 μm with a slice thickness of 400 μm and N = 12 averages.

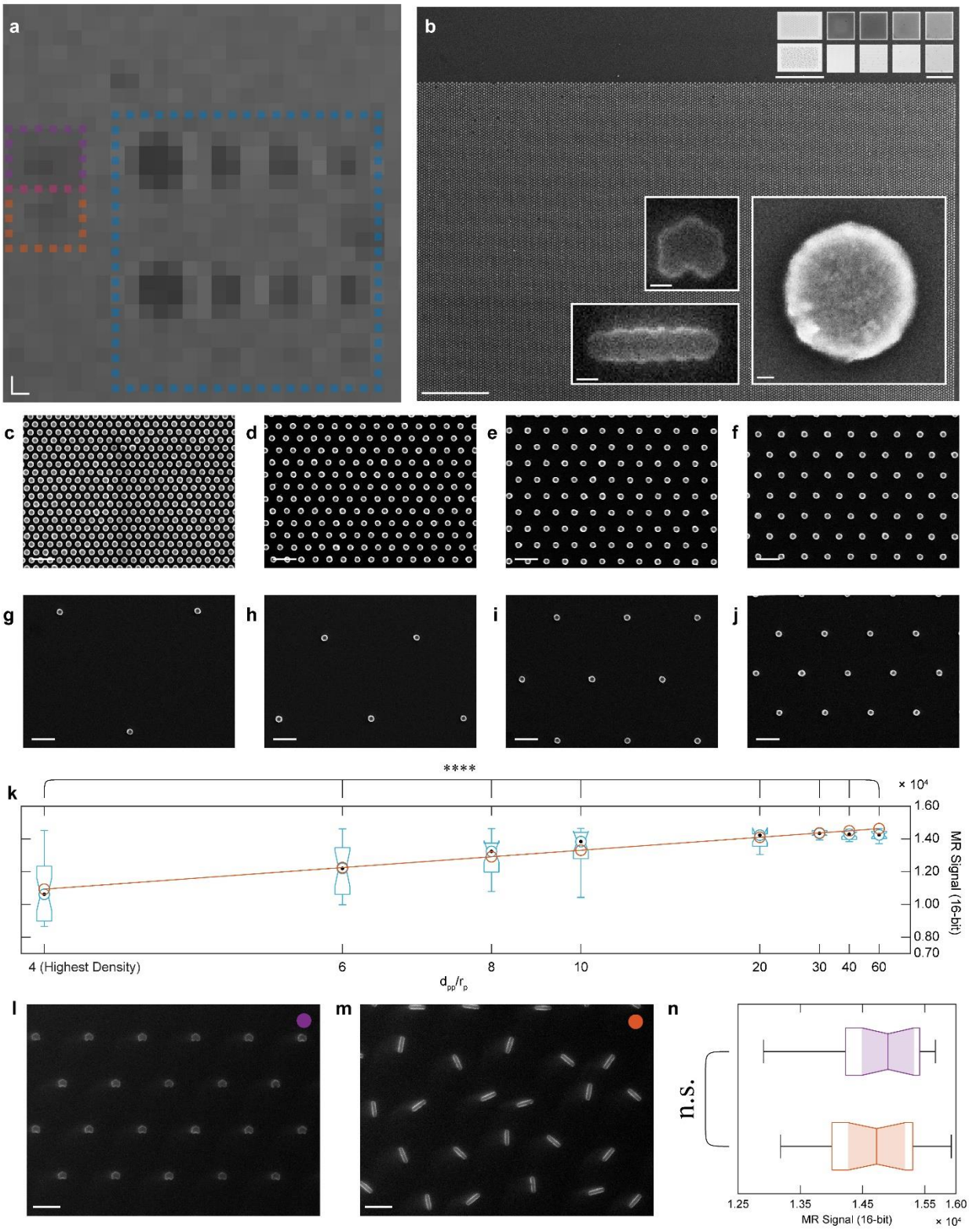
a
b
c
d
e
f
g
h
i
j
k
****
× 10⁴
1.60
1.40
1.20
1.00
0.80
0.70
MR Signal (16-bit)
4 (Highest Density)
6
8
10
20
30
40
60
dpp/rp
l
m
n
n.s.
1.25
1.35
1.45
1.55
1.60
MR Signal (16-bit)
× 10⁴

Figure 24: Magnetic resonance (MR) and scanning electron microscopy (SEM) images of nanopatterned iron oxide arrays reveal density dependence and a non-significant effect of anisotropy on R2.

(a) T2-weighted fast spin-echo multi slice MR images reveal a density-dependent response to 100 × 100 μm^2 nanopatterned iron oxide arrays (diameter = 200 nm, scale bar = 200 μm × 200 μm). Blue, violet, and orange boxes denote regions corresponding to panels c-j, l, and m, respectively. (b) Viewing the nanopatterned iron oxide arrays under SEM (main panel, $d_{pp}/r_p = 4$, scale bar = 10 μm) and optical microscopy (upper insets, left column scale bar = 50 μm, other columns scale bar = 100 μm) shows density-dependent darkening as well as differing anisotropy for chains (bottom left inset, scale bar = 200 nm) and clusters (upper left inset, scale bar = 200 nm). A single-nanoparticle SEM shows consistency and uniformity when approaching single-atom resolution (right inset, scale bar = 30 nm). SEM scans of interparticle spacing to radius (d_{pp}/r_p) ratios of (c) 4, (d) 6, (e) 8, (f) 10, (g) 60, (h) 40, (i) 30, and (j) 20 in the same order as panels a and b are shown below (scale bar = 1 μm). (k) Box plot of relative MR signal intensity versus d_{pp}/r_p. Black dots denote the median, notches denote bounds of statistical significance, and whiskers denote outlier thresholds (from $Q1 - W \times (Q3 - Q1)$ to $Q3 + W \times (Q3 - Q1)$ where $W = 1.5$). The orange line and data points represent a linear curve fit to the medians of each d_{pp}/r_p ($m = 1.5850 \times 10^4$ (MR signal)/$(d_{pp}/r_p)^{-1}$, $b = 2.7895 \times 10^4$ (MR signal); $p = 8.9976 \times 10^{-20}$, **** = $p < 0.0001$, one-way ANOVA, $R^2 = 0.9442$). SEM images of (l) nanoparticle clusters and (m) randomly oriented nanochains (scale bar = 2 μm). (n) Pixel intensity analysis of both regions reveal no significant effect of anisotropy on *R2* ($p = 0.5924$, unpaired t-test).

Quantifications of Density-Dependent MR Intensity Trends

16-bit Digital Imaging and Communications in Medicine (DICOM) MR images were thresholded below a value of 1.47×10^4. For density-dependent DICOM images, ImageJ (National Institutes of Health. Bethesda, Maryland, USA) was used for background correction assuming a light background and a rolling ball radius of 50 px. A 4 px × 4 px selection window was applied to each density. Raw optical images were thresholded at 6.02×10^4 and a polygonal selection was manually applied to each region of interest (ROI). For both image analyses, a least-squares linear fit of iron oxide nanoparticle concentration to median pixel value was used to determine R^2.

Quantifications of Relative R2 Trends

To determine *R2* for each ROI, Python 3.7 was used to curve fit a Gaussian probability density function to a reference histogram of background pixel intensities according to:

$$\boldsymbol{w} = normalpdf\left(\min(\mu_B, \boldsymbol{S}), \sigma_B\right) \quad [2]$$

Where $\boldsymbol{S}$ is the raw MR signal matrix, μ_B is the mean background brightness, σ_B is the standard deviation of background brightness, and *normalpdf* is probability density function of the Gaussian distribution. We then shifted this mean by a constant value for each ROI to compensate for background field inhomogeneities before calculating *R2* values. The resultant pixel weight vectors ($\boldsymbol{w}$) were used to find *T2* values for each voxel ($\boldsymbol{S_{T2}}$) using:

$$\boldsymbol{S_{T2}} = (1 - \boldsymbol{w}\sigma_B\sqrt{2\pi}) * \boldsymbol{S} \quad [3]$$

The output was processed by a Gaussian filter to remove noise (see Table 6 for σ parameter and resultant signal-to-noise values for each ROI type) and estimated relative *R2* with:

$$\mu_{R2} = mean(log(\boldsymbol{S_{T2}})^{-1}) \quad [4]$$

with μ_{R2} is the mean relative *R2* over each ROI normalized to plots of simulated relaxivity changes with minor variations between the corresponding plots.

The output was processed by a Gaussian filter to remove noise (see Table 6 for σ parameter and resultant signal-to-noise values for each ROI type) and estimated relative *R2* with:

$$\mu_{R2} = mean(log(\boldsymbol{S_{T2}})^{-1}) \quad [5]$$

with μ_{R2} is the mean relative *R2* over each ROI normalized to plots of simulated relaxivity changes with minor variations between the corresponding plots.

We translate diffusion coefficient from two to three dimensions by applying the Taylor-Kubo formula:

$$< |\boldsymbol{r}(t) - \boldsymbol{r}(t_0)|^2 > = < |\Delta \boldsymbol{r}(t)|^2 > = v_0^2 \int_{t_0}^{t} dt' \int_{t_0}^{t} dt'' < \hat{\boldsymbol{e}}(t') \cdot \hat{\boldsymbol{e}}(t'') > \quad [4]$$

Where ***r(t)*** is the spatial dynamics of the self-propelled particle (SPP; i.e. water), e is the moving direction (or director), $\boldsymbol{v_0}$ is the constant speed of the SPP, and ***t*** is time and follow this derivation by defining the director correlation function ***C*** as:

$$C(\Delta t) = < \hat{\boldsymbol{e}}(t') \cdot \hat{\boldsymbol{e}}(t' + \Delta t) > \quad [5]$$

While defining the correlating time $\boldsymbol{\tau_c}$ as

$$\tau_c = \int_0^\infty d\Delta t C(\Delta t) \quad [6]$$

We assume $< \boldsymbol{e}(t \to \infty) > = 0$ and rewrite the Taylor-Kubo relation as

$$< |\Delta \boldsymbol{r}(t)|^2 > \sim 2\tau_c v_0^2 t = 2dDt \quad [7]$$

Where *d* is the number of dimensions, and find the spatial diffusion coefficient *D* to be equal to

$$D = \frac{\tau_c v_0^2}{d} \quad [8]$$

To project our distilled two-dimensional system into three dimensions, we therefore applied:

$$D_{2D} = 3 * D_{3D} \quad [9]$$

where D_{2D} is the diffusion coefficient in two dimensions and D_{3D} is the diffusion coefficient in three dimensions[272].

Results

T2 measurements of iron oxide nanoparticle arrays reveal density-dependent and anisotropy-independent behavior

T2-weighted fast spin-echo multi-slice MR images of 200 nm nanopatterned iron oxide particles affirm a density-dependent (particles per unit area) response in 100 × 100 μm^2 arrays and non-significant effect of structure anisotropy (Fig. 24a). Scanning electron micrographs (SEMs) (Fig. 24b, main panel and lower insets) and optical microscopy (Fig. 24b, upper insets) of nanopatterned particles verify consistent linear density-dependent signal decrease (Supplementary Fig. S2.2) and variable anisotropy for nanoparticle chains and clusters (Fig. 24b, upper left – optical, bottom left

– SEM). A single-nanoparticle SEM shows structural uniformity when at near single-atom resolution (Fig. 24b, lower right inset). SEMs of interparticle spacing to radius (d_{pp}/r_p) ratios of 4, 6, 8, 10, 60, 40, 30, and 20 are shown in Fig. 24c-j, respectively and in the same order as Fig. 24a and Fig. 24b. Comparing MRI voxel intensity versus $(d_{pp}/r_p)^{-1}$ reveals a density-dependent response (Fig. 24k). Shown in Fig. 24k are black dots denoting the median, notches denoting bounds of statistical significance, and whiskers denoting outlier thresholds from $Q1 - 1.5 \times (Q3 - Q1)$ to $Q3 + 1.5 \times (Q3 - Q1)$, where $Q1$ is the first quartile or 25th percentile, $Q3$ is the third quartile or 75th percentile, $(Q3 - Q1)$ is the interquartile range, and $1.5 \times (Q3 - Q1)$ is the outlier cutoff threshold. The orange curve in Fig. 24k and corresponding data points represent a linear curve fit to the medians of each $(d_{pp}/r_p)^{-1}$ ($m = 1.5850 \times 10^4$ (MR signal)/$(d_{pp}/r_p)^{-1}$, $b = 2.7895 \times 10^4$ (MR signal); $p = 8.9976 \times 10^{-20}$, **** = $p < 0.0001$, one-way ANOVA). Minor variations in brightness exist at lower densities (*dpp/rp* ranging between 30 and 60), independent of background gradient correction. SEM images of compact nanoparticle clusters and randomly oriented and positioned nanoparticle chains (Fig. 24l and 2m, respectively) confirm the consistency of our cluster fabrication method. MRI signal brightness of both regions reveal no significant effect of anisotropy on *T2* decay (Fig. 24n; $p = 0.5924$, unpaired t-test). Based on these verifications of uniformly dense arrays of single nanoparticles, we turned to finite element analysis to predict the effect of non-uniform aggregation on magnetic fields.

Finite element analysis of hexagonal nanoparticle clusters affirms proximity-dependent field enhancement

We used finite element analysis to quantify B_0-induced magnetization in single nanoparticles (Fig. 25a), and clusters of nanoparticles with *dpp/rp* = 40 (Fig. 25b), *dpp/rp* = 20 (Fig. 25c), *dpp/rp* = 10 (Fig. 25d), and *dpp/rp* = 5 (Fig. 25e). SEM reference images (Fig. 25a(i)-3e(i)) show proof of

principle structures for simulations of magnetic vector potential (Fig. 25a(ii)-3e(ii)), magnetic flux density (Fig. 25a(iii)-3e(iii)), and magnetic field intensity (Fig. 25a(iv)-3e(iv)) of varying cluster values of d_{pp}/r_p. Corresponding running-average mean and standard deviation of fields across a single nanoparticle (Fig. 25f-h, black curves), from the center, left, and right regions of a single nanoparticle (Fig. 25f-h, purple, blue, green curves, respectively), and across the entire cluster (Fig. 25f-h, yellow) are shown for magnetic vector potential z-component ($\mathbf{A}_z$, Fig. 25f), magnetic flux density y-component ($\mathbf{B}_y$, Fig. 25g), and magnetic field intensity y-component ($\mathbf{H}_y$, Fig. 25h). The inverse coefficient of variation (ICV), defined as the mean field amplitude divided by the standard deviation (μ/σ) surrounding nanoparticles in the simulation arena (Fig. 25j-l) shows greater variability for clustered nanoparticles compared with single nanoparticles under the same simulation conditions, demonstrating a clear aggregation-related effect. Specifically, the residual sum of squares (RSS) for single nanoparticles for $\mathbf{A}_z$, $\mathbf{B}_y$, and $\mathbf{H}_y$ are 0.0561, 0.0063, and 51.0562, while for the center nanoparticle in a cluster they are 0.3968 (7.0733×RSS_{single}), 5.4398 (862.6164), and 168.2382 (3.2952), and for the whole cluster the values are 0.3537 (6.3044), 0.6542 (103.7460), and 122.3860 (2.3971) (Fig. 25m). The larger RSS for clusters affirms that iron oxide nanoparticle clusters exhibit highly variable fields compared with single nanoparticles. While ICV increases relatively linearly for single nanoparticles, changes are more stochastic or highly nonlinear for the entire cluster and single nanoparticles at the cluster center. Subtracting the line of best fit yields standard deviations for $\mathbf{A}_z$, $\mathbf{B}_y$, and $\mathbf{H}_y$ of 0.0123, 0.0041, and 0.3715 for single nanoparticles, 0.0327 (2.6596×σ_{single}), 0.1213 (29.3703), and 0.6743 (1.8153) for center nanoparticles, and 0.0309 (2.5109), 0.0421 (10.1856), and 0.5751 (1.5483) for the whole cluster (Fig. 25n). Of note are ICVs for magnetic flux density (Fig. 25k) which fluctuate from -0.0099 at $dpp/rp = 20.9$ to 0.0345 at $dpp/rp = 3.0$ for isolated single iron oxide nanoparticles compared to

fluctuations from -0.0077 at *dpp/rp* = 3.6 to 0.7086 at *dpp/rp* = 7.3 for center iron oxide nanoparticles. These simulations therefore predict that aggregation of nanoparticles produces fields that show asymptotic behavior with increasing d_{pp}/r_p and are spatially diverse compared to those of single nanoparticles.

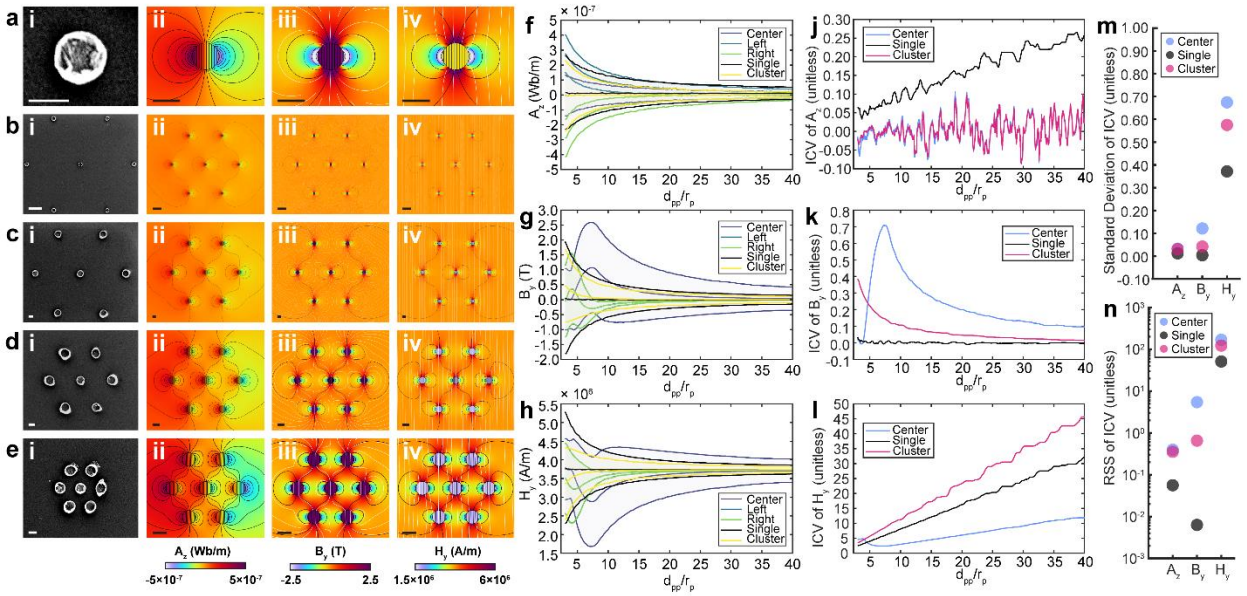

Figure 25: Finite element analysis demonstrate highly diverse magnetic fields in proximity to nanoparticle clusters compared with single nanoparticles.

Data for (a) nanoparticles, nanoparticle clusters with (b) $d_{pp}/r_p = 40$, (c) $d_{pp}/r_p = 20$, (d) $d_{pp}/r_p = 10$, and (e) $d_{pp}/r_p = 5$ (nanoparticle diameter = 200 nm, scale bar = 200 nm except (b) where scale bar = 1 µm). SEM a(i)-e(i), magnetic vector potential z-component $\mathbf{A}_z$ a(ii)-e(ii), magnetic flux density y-component $\mathbf{B}_y$ a(iii)-e(iii), magnetic field intensity y-component $\mathbf{H}_y$ a(iv)-e(iv) of various d_{pp}/r_p. Corresponding running-average (n=4) mean and standard deviation of a nanoparticle and center, left, right, and entire cluster are shown for (f) $\mathbf{A}_z$ (g) $\mathbf{B}_y$ and (h) $\mathbf{H}_y$. Changes in inverse coefficient of variation (ICV) for varying interparticle distance to particle radius (c.f. panels f-h). The inverse coefficient of variation (ICV), defined as the mean divided by the standard deviation of field values around particles in the simulation arena, for (j) magnetic vector potential z-component $\mathbf{A}_z$, (k) magnetic flux density y-component $\mathbf{B}_y$, and (l) magnetic field intensity y-component $\mathbf{H}_y$ of d_{pp}/r_p ranging from 3.0 to 40.0 in increments of 0.1. While the ICV increases relatively linearly for single particles, changes are more stochastic or highly nonlinear for the entire cluster, particularly the

nanoparticle at the center of the cluster. Comparing (m) the residual sum of squares (RSS) and (n) the adjusted standard deviation of the ICV versus magnetic field type shows that single nanoparticles are less variable than clusters and center nanoparticles.

MR scan-derived R2 trends agree with Monte Carlo simulations

To corroborate nanoparticle aggregation- and nanoparticle size-dependent field effects predicted in theory, we performed MRI of varying nanopatterned iron oxide cluster arrays (Fig. 26). SEMs of constant $dpp/rp = 10$ and variable nanoparticle sizes of 800 nm (Fig. 26a), 200 nm (Fig. 26b), 100 nm (Fig. 26c), and 70 nm (Fig. 26d) demonstrate consistent uniformity of nanoparticles and nanoparticle clusters (Fig. 26a-l). Four representative nanoparticle clusters (and corresponding zoomed insets) with nanoparticle diameter of 100 nm and $dpp/rp = 5$ (Fig. 26e (4i)), $dpp/rp = 10$ (Fig. 26f (4j)), $dpp/rp = 20$ (Fig. 26g (4k)), and $dpp/rp = 40$ (Fig. 26h (4l)) are shown. Our *R2* analyses show agreement in diffusional correlation time $\tau_D = r_p^2/D$ for single nanoparticles (Fig. 26m; corresponding SEMs in Fig. 26a-d) and nanoparticle clusters (Fig. 26n; see Fig. 25e and Fig. 26e) and *dpp/rp* for clusters of small nanoparticles ($r_p = 35$ nm or 50 nm; Fig. 26o; see Fig. 26e-h) and clusters of large nanoparticles ($r_p = 400$ nm; Fig. 26p; see Fig. 25b-e). When present, lines denote the median, notches denote bounds of statistical significance, and whiskers denote outlier thresholds from $Q1 - 1.5 \times (Q3 - Q1)$ to $Q3 + 1.5 \times (Q3 - Q1)$, where *Q1* is the first quartile or 25th percentile, *Q3* is the third quartile or 75th percentile, $(Q3 - Q1)$ is the interquartile range, and $1.5 \times (Q3 - Q1)$ is the outlier cutoff threshold. Shown in Fig. 26q are corresponding MRI ROIs for panel (m) after conversion to *R2*. We find negative quadratic relationships $(-0.0045(\log \tau_D)^2 - 0.0655(\log \tau_D) - 2.7800)$ (Fig. 26m) for single nanoparticles of varying sizes and for clusters $(-0.0045(\log \tau_D)^2 - 0.0827(\log \tau_D) - 2.3249)$ (Fig. 26n) for varying diffusional correlation time $\tau_D = r_p^2/D$. Small clusters show changes smaller than the background noise level which we fit quadratically $(3.2046 \times 10^{-6} (d_{pp}/r_p)^2 - 2.6204 \times 10^{-4} (d_{pp}/r_p) - 2.0075)$, inverse quadratically $(-7.9436 \times 10^{-7} (d_{pp}/r_p)^{-2} + 6.4888 \times 10^{-5} (d_{pp}/r_p)^{-1} - 0.4981)$ and exponentially $(-2.0050(d_{pp}/r_p)^{0.0010})$ (Fig. 26o). We applied Gaussian filtering to reduce noise in

this ROI and determined that the percent change in signal remained consistent (-0.2097% to -0.2382%, Supplementary Fig. S2.3, see Table 6 for SNR values). We additionally found large clusters show positive quadratic relationships well above noise level (3.8615×10^{-6} $(d_{pp}/r_p)^2$ - 9.3853×10^{-5} (d_{pp}/r_p) - 2.0393) (Fig. 26p). While our data show trends in agreement with previous Monte Carlo simulation studies[263, 264], we carefully and explicitly note the uncertainty in translating our results from two to three dimensions.

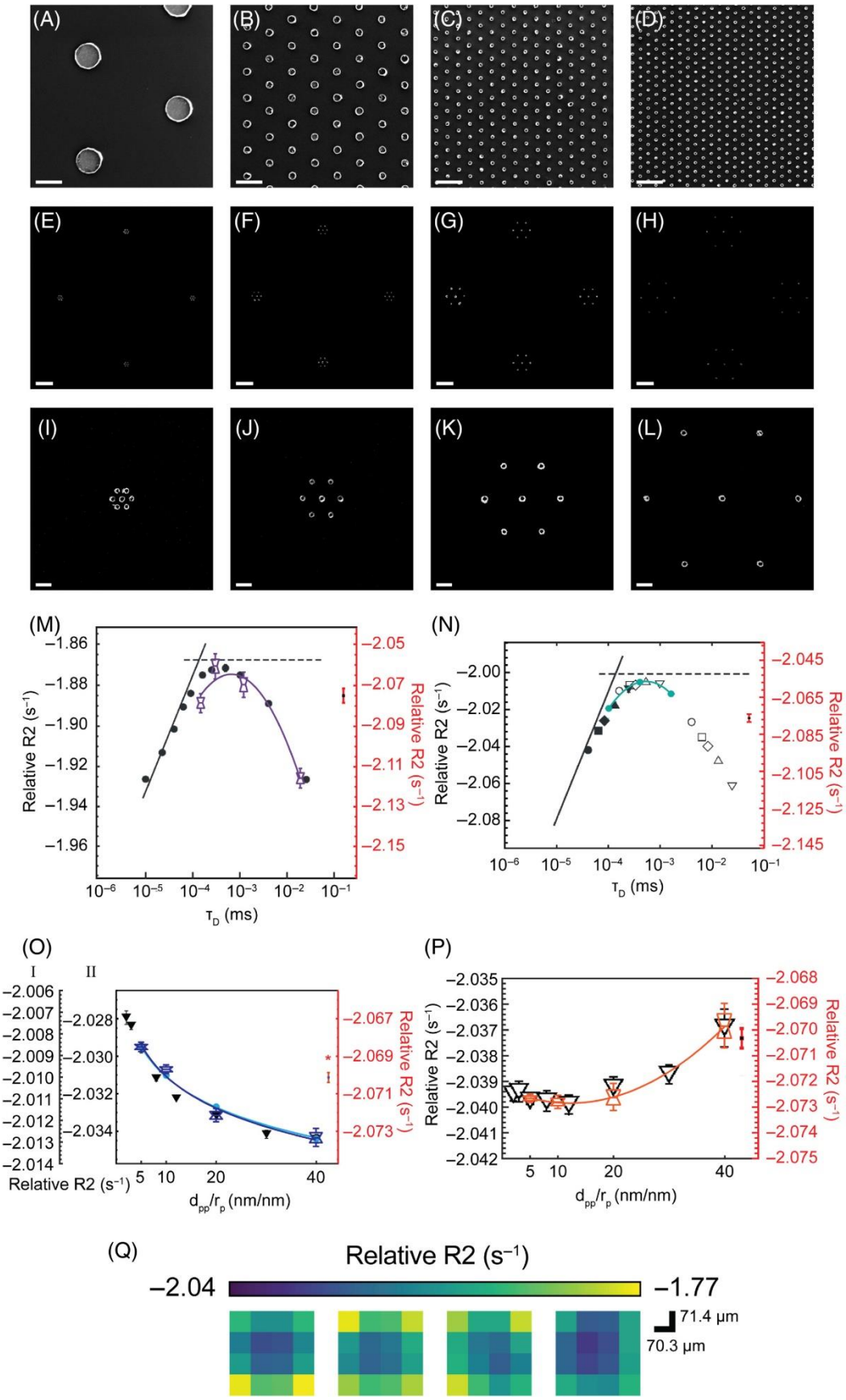
(A)
(B)
(C)
(D)
(E)
(F)
(G)
(H)
(I)
(J)
(K)
(L)
(M)
Relative R2 (s⁻¹)
−1.86
−1.88
−1.90
−1.92
−1.94
−1.96
−2.05
−2.07
−2.09
−2.11
−2.13
−2.15
Relative R2 (s⁻¹)
10⁻⁶ 10⁻⁵ 10⁻⁴ 10⁻³ 10⁻² 10⁻¹
τD (ms)
(N)
Relative R2 (s⁻¹)
−2.00
−2.02
−2.04
−2.06
−2.08
−2.045
−2.065
−2.085
−2.105
−2.125
−2.145
Relative R2 (s⁻¹)
10⁻⁶ 10⁻⁵ 10⁻⁴ 10⁻³ 10⁻² 10⁻¹
τD (ms)
(O)
I
II
−2.006
−2.007
−2.008
−2.009
−2.010
−2.011
−2.012
−2.013
−2.014
−2.028
−2.030
−2.032
−2.034
−2.067
−2.069
−2.071
−2.073
Relative R2 (s⁻¹)
Relative R2 (s⁻¹)
5 10 20 40
dpp/rp (nm/nm)
(P)
Relative R2 (s⁻¹)
−2.035
−2.036
−2.037
−2.038
−2.039
−2.040
−2.041
−2.042
−2.068
−2.069
−2.070
−2.071
−2.072
−2.073
−2.074
−2.075
Relative R2 (s⁻¹)
5 10 20 40
dpp/rp (nm/nm)
(Q)
Relative R2 (s⁻¹)
−2.04
−1.77
71.4 µm
70.3 µm

Figure 26: Scanning electron microscope (SEM) images and corresponding MR R2 plots of signal and noise show trends in agreement with previous Monte Carlo simulations.

Shown are SEMs of different nanopatterned iron oxide arrays with d_{pp}/r_p = 10 of sizes (a) 800 nm, (b) 200 nm, (c) 100 nm, and (d) 70 nm (scale bar = 1 μm). Below are SEMs of four representative nanoparticle clusters of r_p = 50 nm and (e) d_{pp}/r_p = 5, (f) d_{pp}/r_p = 10, (g) d_{pp}/r_p = 20, and (h) d_{pp}/r_p = 40 (scale bar = 2 μm), corresponding to magnified panels (i-l, scale bar = 400 nm). Relative *T2* relaxation rates (*R2*) (left axis) and noise levels (right axis) normalized to previous simulations show agreement in diffusional correlation time $\tau_D = r_p^2/D$ for (m) single nanoparticles (panels a-d) and (n) nanoparticle clusters of nanoparticles (panel e (inset panel i) size differs). Relative *R2* values from nanoparticle clusters of (o) small nanoparticles (r_p = 35 nm or 50 nm as in panels e-h (inset panels i-l))) where I corresponds to raw data (light blue), II corresponds to Gaussian blurred data (navy blue), and * denotes noise level after Gaussian blurring. and (p) large nanoparticles (r_p = 400 nm patterned like panels e-h (i-1), size differs) also show *R2* trends versus d_{pp}/r_p in agreement with Monte Carlo simulations. When present, lines denote the median, notches denote bounds of statistical significance, and whiskers denote outlier thresholds from $Q1 - 1.5 \times (Q3 - Q1)$ to $Q3 + 1.5 \times (Q3 - Q1)$, where *Q1* is the first quartile or 25th percentile, *Q3* is the third quartile or 75th percentile, $(Q3 - Q1)$ is the interquartile range, and $1.5 \times (Q3 - Q1)$ is the outlier cutoff threshold. Shown in (q) are corresponding MRI ROIs for panel (m) after conversion to *R2*.

Discussion and Conclusions

Here we leveraged nano-scale lithography to precisely pattern clusters of iron oxide nanoparticles and quantify their *R2* using fast spin-echo multi-slice MR scan data. We found nonlinear polynomial *R2* dependence for both single and diversely clustered iron oxide dots with varying interparticle distance and particle radius. Further, we report an exponential aggregation-dependent relationship between interparticle distance and particle radius, verified by nonlinear least squares trust region reflective fit strategy. A two-dimensional array of SPIONs situated on a planar silicon surface also mainly effects field perturbations for water molecules diffusing near the plane of the nanoparticle cluster array, which may help explain relatively low SNR for exponentially-fitted small nanoparticles without Gaussian filtering. To characterize magnetic field behavior for a continuum of varying interparticle spacings for nanoparticle clusters, we analyzed magnetic field maps from our finite element nanoparticle cluster model and found increasing variability quantified by both inverse coefficient of variation (ICV) and residual sum of squares (RSS) with decreasing interparticle distance to particle radius ratio (d_{pp}/r_p). We note that while we investigated *T2* relaxation effects for nanoparticles with radius as small as 35 nm, some clinically used SPIONs can be as small as 4 nm[236]. Earlier theoretical work shows that MNPs below 10 nm in diameter are expected to continue trends predicted by microscopic outer sphere theory[260]. Extrapolating our experimental results yields a similar decline in the form of relative R2 of -2.006 s-1 for 10 nm nanoparticles and -2.214 s-1 for clusters, correlating with theoretical predictions and corresponding to the quadratic nature of diffusion distances versus time, whereby water molecules are expected to diffuse past small particles (<10 nm) more than an order of magnitude faster than 35 nm particles. Nonetheless, smaller particle sizes usually result in more efficient tissue clearance and the effect on diffusing water molecules described here coincides with the overall applicability

of biomedically relevant single nm SPIONs.[273, 274]. Some discrepancies could be a result of nano- and pico-scale variations in fabricated structures compared with chemical synthesis of SPIONs. The ability to determine precise peak *R2* values by nanopatterning diverse cluster topologies can drive the design of new sensor technologies for MRI. Our fabrication protocol could be expanded for patterning other particle material compositions and even patterning of widely used molecular agents. Broadening the scope of both native and modified nanoparticles for MPI[275], ODMR[276], and fluorescent imaging[277] could help optimize static and dynamic image contrast, signal-to-noise ratio, and sensitivity to analytes without sacrificing biocompatibility or resolution. Future experiments will comprise nanofabricating two- and three-dimensional array combinations composed of self-assembling modules with additional geometries to confirm that our work extends to three dimensions and performing multimodal magnetic imaging of array samples implanted *in vivo*. In conclusion, our analyses agree with and contribute further understanding into iron oxide nanoparticle aggregation-dependent field behavior observed in theoretical predictions. Our results lay a robust and adaptable foundation for the design and development of nanometer- and micrometer-scale contrast agents and probes for MRI and related modalities.

Acknowledgments

The authors gratefully acknowledge the use of facilities and instrumentation supported by NSF through the University of Wisconsin Materials Research Science and Engineering Center (DMR-1720415) and thank Dr. Alan McMilllan for useful advice about magnetic resonance measurements. This work was supported by the National Institute of Neurological Disorders and Stroke and the Office of the Director's Common Fund at the National Institutes of Health (Grant DP2NS122605 to AH), the National Institute of Biomedical Imaging and Bioengineering (Grant K01EB027184 to AH) and the Wisconsin Alumni Research Foundation (WARF).

Table 4: Parameters used for electron beam lithography patterning of Si/PMMA substrate

Array Type	*Density/Anisotropy*	*Size/Cluster*
Field Size (µm)	250	250
Dot Number	500,000	500,000
Exposure (µC/cm^2)	800	[800, 1600, 2400]
Feed Pitch	10	10
Scan Pitch	10	10
Beam Current (nA)	2	10
Exposure Time (µs/dot)	0.10	[0.02, 0.04, 0.06]
Matrix Size (µm × µm)	100.0 × 100.0 (Density) 122.5 × 70.0 (Anisotropy)	100.0 × 100.0

Table 5: Parameters used for magnetic resonance scans of iron oxide nanoparticle arrays

Scan Parameters	***Density and Anisotropy Arrays***	***Size and Spacing Arrays***
Pulse Sequence	**FSEMS**	**FSEMS**
Field Strength (T)	4.7	4.7
Echo Time (msec)	68	85
Repetition Time (msec)	4000	5000
Voxel Size (μm × μm)	78.1 × 79.4	70.3 × 71.4
Slice Thickness (μm)	700	400
Number of Averages	10	12

Table 6: Gaussian blurring (GB) parameters and corresponding signal-to-noise (SNR) values for R2 plots in Fig. 26

Analysis Type	*ROI size*	*Gaussian Kernel σ*	*μ Noise (s^{-1})*	*σ Noise (s^{-1})*	*SNR (dB)*
Single	3×3	1	-2.071	1.071×10^{-3}	44.530
Cluster	2×2	0	-2.076	2.173×10^{-3}	24.983
Small Clusters	2×4	0	-2.074	3.349×10^{-3}	25.134
Small Clusters GB	2×2	2	-2.070	2.652×10^{-4}	43.198
Large Clusters	2×3	2	-2.070	3.800×10^{-4}	37.429

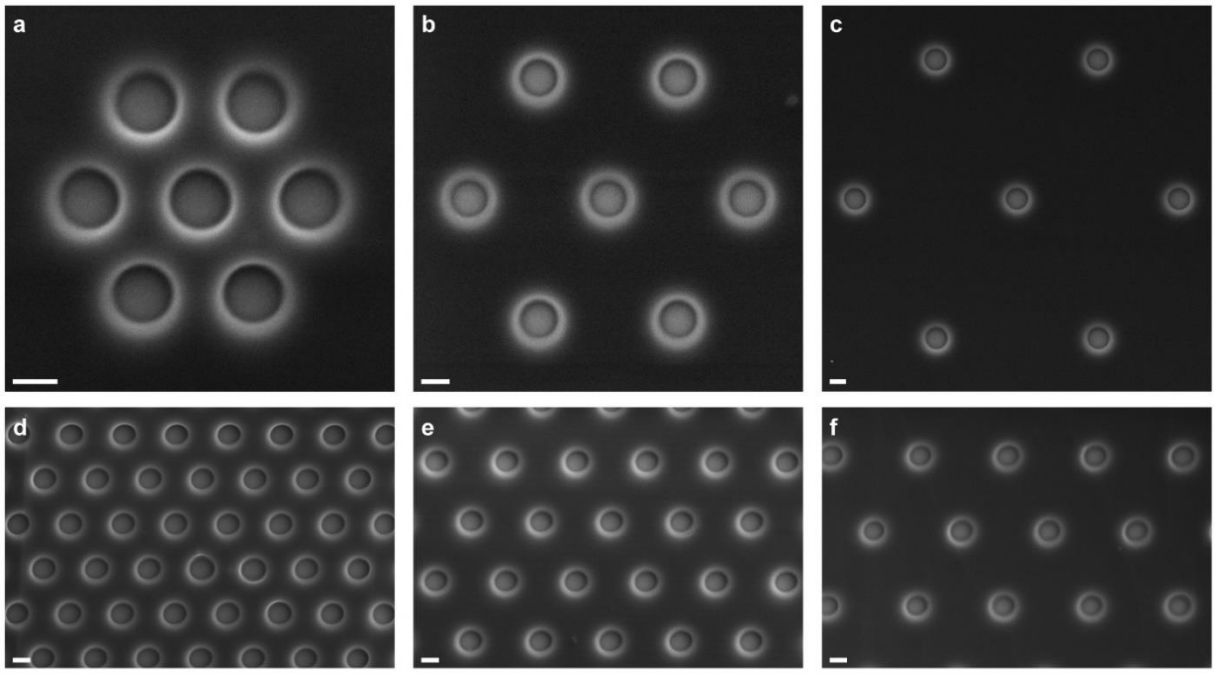

Figure 27: Scanning electron microscope (SEM) images of developed poly methyl-methacrylate before iron oxide deposition.

Shown are SEMs of representative hexagonal nanovoids patterned on poly methyl-methacrylate with (a) d_{pp}/r_p = 5, (b) d_{pp}/r_p = 10, and (c) d_{pp}/r_p = 20, and nanovoids with spacing (d) d_{pp}/r_p = 6, (e) d_{pp}/r_p = 8, and (f) d_{pp}/r_p = 10 (scale bars = 200 nm).

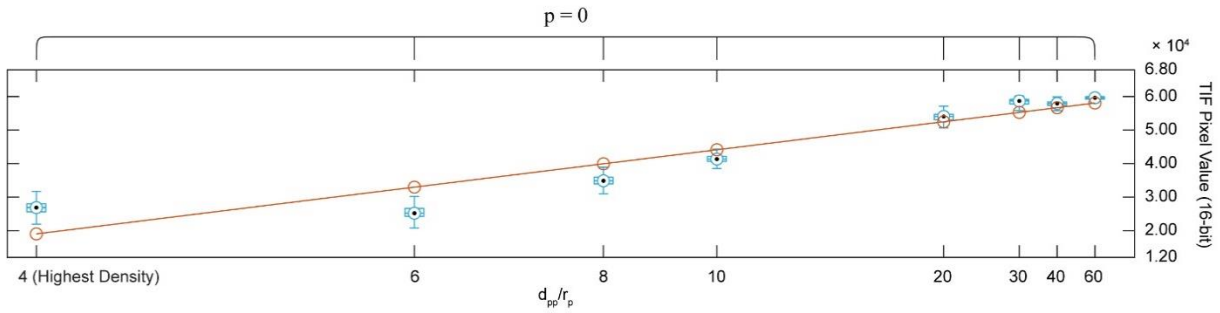

Figure 28: Linear fit of iron oxide nanostructure array optical image intensity.

Box plot of optical image intensity (see square insets in upper right of Fig. 2b) versus d_{pp}/r_p. Black dots denote the median, notches (present but not visible) denote bounds of statistical significance, and whiskers denote outlier thresholds (from $Q1 - W \times (Q3 - Q1)$ to $Q3 + W \times (Q3 - Q1)$ where $W = 1.5$). The orange line and data points represent a linear curve fit to the medians of each d_{pp}/r_p ($m = 1.6475 \times 10^5$ (Optical intensity)/$(d_{pp}/r_p)^{-1}$, $b = 6.0603 \times 10^4$ (Optical intensity); $p = 0$, one-way ANOVA, $R^2 = 0.8915$).